

THESIS FOR THE DEGREE OF DOCTOR OF PHILOSOPHY

High-Temperature Corrosion in Biomass- and Waste-fired Boilers:

Current Challenges and the Impact of Integrating Carbon Capture Technology

HAMPUS LINDMARK

Department of Chemistry and Chemical Engineering
CHALMERS UNIVERSITY OF TECHNOLOGY
Gothenburg, Sweden 2025

High-Temperature Corrosion in Biomass- and Waste-fired Boilers: *Current Challenges and the Impact of Integrating Carbon Capture Technology*

HAMPUS LINDMARK

ISBN: 978-91-8103-214-7

Acknowledgements, dedications, and similar personal statements in this thesis, reflect the author's own views.

© HAMPUS LINDMARK, 2025

Doktorsavhandlingar vid Chalmers tekniska högskola

Ny serie nr 5672

ISSN 0346-718X

Department of Chemistry and Chemical Engineering

Chalmers University of Technology

SE-412 96 Gothenburg

Sweden

Telephone +46 (0)31-772 1000

Cover:

Scanning electron microscope (SEM) image acquired in backscattered electron (BSE) mode, showing the surface morphology of a low-alloyed steel exposed to $\text{PbCl}_2(\text{s}) + 5\% \text{O}_2 + 20\% \text{H}_2\text{O} + \text{N}_2 \text{ bal.}$ at 400°C for 168 hours. The dark regions correspond to iron-rich oxide while the bright areas represent lead oxide formed through the reaction of $\text{PbCl}_2(\text{s})$ with the surrounding environment.

Printed by Chalmers Digitaltryck
Gothenburg, Sweden 2025

High-Temperature Corrosion in Biomass- and Waste-fired Boilers:

Current Challenges and the Impact of Integrating Carbon Capture Technology

HAMPUS LINDMARK

Department of Chemistry and Chemical Engineering

Chalmers University of Technology

Abstract

Substituting fossil fuels with biomass and waste-derived fuels is a recognized strategy for promoting more-sustainable heat and electricity production. However, compared to fossil fuels, biomass and waste have higher levels of corrosive species, which upon combustion can interact with critical boiler components and cause significant corrosion. This results in reduced electricity output and makes the transition to more-sustainable fuels less-appealing to key stakeholders. To enable increased electricity production, it is essential to enhance our understanding of corrosion mechanisms in this environment.

This thesis investigates corrosion phenomena related to the combustion of biomass and waste, through a combination of laboratory experiments, field exposures and kinetic modeling. In particular, it looks at the following topics: corrosion of superheaters positioned in the loop seal of a circulating fluidized bed (CFB) waste-fired boiler; PbCl_2 -induced corrosion of low-alloyed steels; and kinetic modeling of corrosion in superheater tubes. The latter aspect is approached through a novel methodology that combines oxide microstructural analyses from laboratory and field exposures with thermodynamic kinetic simulations. The corrosion products and microstructures were characterized using a combination of x-ray diffraction (XRD) and electron backscattered diffraction (EBSD) for phase identification and scanning electron microscopy (SEM) coupled with energy-dispersive x-ray spectroscopy (EDX) for microstructural evaluation. Broad ion beam (BIB) milling was used to prepare high-quality cross-sectional samples.

The results reveal that corrosion plays an important role in the degradation rates of various alloy types in the loop seal of CFB waste-fired boilers. FeCrAl alloys exhibit material loss rates comparable to those of conventional nickel-based alloys, positioning them as cost-effective alternatives. However, significant nitridation was observed in these alloys, and further studies are required to understand its impact on their protective and mechanical properties. Furthermore, PbCl_2 -induced corrosion on low-alloyed steels was found to be severe, with oxide scale delamination identified as a key degradation mechanism. This phenomenon is attributed to the formation of metal chlorides at the metal/oxide interface, which weakens scale adhesion and accelerates corrosion. Microstructural analyses of superheater tubes exposed for up to 4 years in the convective pass of a CFB waste-fired boiler revealed the presence of dense and adherent oxide scales on top of the alloy substrate, supporting the use of parabolic oxide growth modeling. Discrepancies between the simulated material losses and measured material losses in superheaters that were exposed in a commercial boiler were observed, likely attributable to cyclic corrosion influenced by chlorine load and boiler operating conditions.

Lastly, this thesis explores high-temperature corrosion in chemical looping combustion (CLC), a promising technology for achieving negative CO_2 emissions and efficient electricity production with sustainable fuels. A novel laboratory setup was developed to simulate continuous alkali release in the air reactor. The results show that conventional chromia-forming alloys experience accelerated corrosion, whereas an FeCrAl alloy exhibits strong corrosion resistance under the same conditions.

Keywords: *Biomass, Waste, Boilers, High-temperature corrosion, Alloys, Chemical looping combustion, Modeling*

List of appended papers

This thesis is based on the following papers:

Paper I

H. Lindmark*, J. Phother, M. Dolores Paz, J. Nockert, F. Lind, A. Jonasson, V. Barišić, K. Vänskä, L. Rioja-Monllor and J. Liske. *A material degradation study of novel FeCrAl alloys, stainless steels and nickel base alloy in fluidized bed heat exchangers of a waste-fired CFB boiler.* **Fuel**, Vol. 338., p. 127299- Published 2023.

Paper II

H. Lindmark*, T. Jonsson and J. Liske. *A time-resolved study of PbCl₂-induced corrosion of low-alloyed steel in the presence of water vapour at 400 °C.* **Corrosion Science**, Vol. 229., p. 111843- Published 2024.

Paper III

H. Lindmark*, H. Larsson, M. Dolores Paz, S. Andersson, L. Höglund, T. Jonsson, and J. Liske. *A framework for predicting superheater corrosion in waste-fired boilers: integrating kinetic simulations, oxide microstructure and boiler operation.* (**Manuscript**).

Paper IV

H. Lindmark*, R. Faust, T. Sand, L.G Johansson, P. Knutsson, and J. Liske. *Corrosivity of KOH(g) towards superheater materials in a simulated air reactor environment for chemical looping combustion of biomass.* **Fuel**, Vol. 381. p. 133178- Published 2025.

* Corresponding author

Statement of the author's contribution

Paper I: Collected and analyzed data, wrote the first draft. Led the revision of the manuscript.

Paper II: Conceptualization, participating in planning and designing the study, carried out the experiments, collected and analyzed data, wrote the first draft. Led the revision of the manuscript.

Paper III: Contributed to developing the experimental approach for microstructure characterization, data analysis, and wrote part of the first draft.

Paper IV: Participating in planning and designing the study, carried out the experiments, collected and analyzed data, wrote the first draft. Led the revision of the manuscript.

Related technical report not included in this thesis:

H. Lindmark, F. Lind, M. Dolores Paz, L. Rioja-Monllor, B. Wahlund, A. Jonasson, J. Nockert, M. Hautakangas, H. Larsson, V. Barišić, K. Vänskä and J. Liske. “*New materials and oxygen carrier aided combustion for improved competitiveness of FB plants using renewable fuels*”. Konsortium Materialteknik för Termiska Energiprocesser (KME) report 2022. ISBN: 978-91-7673.

Acknowledgement

Before diving into the scientific outcome presented in this thesis, I find it important to take a moment to thank everyone who supported me throughout my PhD journey.

Firstly, I would like to thank my main supervisor Dr. Jesper Liske. You are an excellent researcher and your feedback on my work has greatly enriched my learning experience. You have encouraged me to take the lead and responsibility for my research from day one. Thank you for giving me the freedom to think independently, explore my own ideas, and take risks rather than micromanaging me. Your trust has allowed me to grow as a researcher in a way that has been extremely rewarding. I have not only enjoyed our discussions regarding science, but also our talks about life in general, and of course, your amazing crème brûlée! Thank you for always believing in me during the (∞) times I doubted myself.

Secondly, I would like to thank my co-supervisor, Dr. Torbjörn Jonsson. The title of “co-supervisor” has always felt inadequate to describe your role during my PhD journey. Your support and feedback on my work has truly been helpful. Your extensive knowledge in microscopy and willingness to share it has been so inspiring and “instrumental” throughout this journey. Thank you.

I would like to thank my examiner Professor Jan-Erik Svensson. I always felt that you had my back throughout this journey and your door was always open for discussion. Thank you not only for your input in my work but also for your encouragement. I would like to extend my gratitude to Professor Lars-Gunnar Johansson. Although not part of my supervision team on paper, your input in my work has been very important. Your knowledge of inorganic chemistry and corrosion is truly inspiring.

My heartfelt gratitude goes to Dr. Maria Paz Olausson. Thank you for your immense support in helping me with instruments and setting up lab trials. You were one of the few people available on site when I started my PhD during COVID, and without your guidance during that challenging time, I would likely not have completed my degree in time. Your “everything can be solved” mentality is so inspiring and a testament of why you are such a brilliant researcher and mentor.

I am very grateful for all past and present PhD students and employees in the Division of Energy and Materials. You are exceptional researchers, and you have together made this a fun place to work at. To Dr. Tommy Sand, I am grateful for all the support, especially during the first year when building my PbCl₂ lab set-up and discussing research ideas. I would also like to thank Dr. Johan Eklund, Dr. Vicent Ssenteza, Dr. Julien Phother, Dr. Mareddy Reddy and Hooman Karimi Abadeh for the fun times and many fruitful discussions that have greatly enriched my work. I would like to thank my office mates, Dr. Esraa Hamdy, Aida Nikbakht and Shweta Dhiman. Cheers for the great laughs and support! I would like to further acknowledge Dr. Christine Geers for her support and encouragement, especially during those many long weekends. Who knew that science never sleeps? Special thanks to my colleagues and friends, Dr. Robin Faust and Dr. Matthieu Tomas. I appreciate our friendship, your support, our deep discussions on the meaning of life, and the way you turned all our ping-pong games into high-stake showdowns. Mr. Thorbjørn Krogsgaard, despite our endless debates over whether Sweden or Denmark reigns supreme, having you as a colleague throughout this journey has been nothing short of amazing. Mange takk!

Furthermore, I am so grateful for all the fruitful discussions and collaborations I have had with my co-authors and industry partners. Thank you for sharing your knowledge with me! Special thanks

to Anna Jonasson at E.ON for always being just a phone call away, ready to answer even the simplest questions about boiler design and process parameters.

I am truly grateful for the technical support from Chalmers Material Analysis Laboratory (CMAL). A special thanks goes to Dr. Stefan Gustavsson for his assistance with the SEM instruments.

I would like to dedicate the last part to my family. Thank you for your patience. I thank my mother for teaching me that hard work pays off and my sisters for always believing in me. Thank you to my brother Dr. Max Lindmark, who has been such a helpful guide throughout this journey. Thank you for always offering your advice when needed.

Ludo, I know there were times during this period when being around me was about as fun as watching a handball game. Despite the long working hours and self-doubt, your belief in me has never wavered. Your love and support have been the most important factor in me completing this work. Thank you for always cheering me up no matter the difficulties.

Dearest Dad. Your pride in my acceptance as a PhD candidate at Chalmers will forever remain in my memories. Although you are no longer with us, your invaluable lessons of kindness, courage, wisdom, and humility have shaped the person I am today. Throughout my PhD journey, I have felt your guidance every step of the way.

Hampus Lindmark, Gothenburg (2025)

Contents

Abstract.....	i
List of appended papers	iii
Acknowledgement.....	v
Contents	vii
1. Renewable fuels for heat and electricity production: motivation, opportunities and corrosion challenges.....	1
1.1 Objectives	4
1.1.1 Part I- Investigation of corrosion mechanisms in biomass and waste-fired boiler environments	4
1.1.2 Part II- Potential corrosion challenges in chemical looping combustion of biomass.....	5
2. Combustion of biomass and waste.....	7
2.1 Circulating fluidized bed boiler	7
2.2 Integration of carbon capture technology into power plants.....	9
2.2.1 Post-combustion.....	9
2.2.2 Oxy-fuel combustion	10
2.2.3 Chemical looping combustion	11
3. High-temperature corrosion	13
3.1 Thermodynamics.....	13
3.2 Oxide growth	14
3.3 Kinetics	15
3.3.1 Linear rate law	16
3.3.2 Logarithmic rate law.....	16
3.3.3 Parabolic rate law	17
3.4 Diffusion paths through oxides	18
3.5 Breakaway corrosion- primary vs secondary corrosion regime.....	19
4. Alloys used in this thesis	23
4.1 Ferritic low-alloyed steels.....	23
4.2 Austenitic stainless steels	23
4.3 Nickel-based alloys	23
4.4 FeCrAl alloys	23
5. Corrosion mechanisms in biomass and waste-fired boilers	25
5.1 Chlorine-induced corrosion.....	25
5.1.1 Active oxidation	25
5.1.2 The electrochemical approach	26
5.1.3 Delamination of oxide scales in presence of Cl.....	26
5.2 Molten-phase corrosion	27

5.3 Chromate formation	28
5.4 Corrosion-erosion	28
5.4.1 Erosion of oxide	29
5.4.2 Erosion-enhanced corrosion.....	29
5.4.3 Oxidation-affected erosion.....	29
5.5 PbCl ₂ -induced corrosion	30
6. Analytical techniques	33
6.1 Scanning electron microscopy	33
6.2 Broad ion beam milling	35
6.3 X-ray diffraction	37
6.4 Average grain size measurement.....	38
6.5 Electron backscatter diffraction	38
6.6 Kinetic modelling of oxide growth using the DICTRA approach	39
7. Part I:	41
Investigation of corrosion mechanisms in biomass and waste-fired boiler environments.....	41
7.1 Experimental: Paper I	42
7.2 Experimental: Paper II	43
7.3 Experimental: Paper III.....	45
7.4 Results & discussion	47
7.4.1 Paper I- degradation behavior of superheater materials positioned in the loop seal of a waste-fired CFB boiler	47
7.4.2 Paper II- PbCl ₂ -induced corrosion on low-alloyed steel	54
7.4.3 Paper III- A framework for predicting superheater corrosion in waste-fired boilers: integrating kinetic simulations, oxide microstructure, and boiler operation	62
8. Part II:	69
Potential corrosion challenges in chemical looping combustion of biomass.....	69
8.1 Background.....	69
8.1.1 Corrosion in the fuel reactor.....	69
8.1.2 Corrosion in the air reactor	70
8.1.3 Material selection for superheater applications in CLC.....	72
8.2 Experimental overview- Part II.....	73
8.3 Experimental: Paper IV.....	74
8.4 Results & discussion: Paper IV.....	76
8.4.1 Chromia-forming alloys	76
8.4.2 Alumina-forming alloy	81
9. Concluding remarks	83
9.1 Part I- Investigation of corrosion mechanisms in biomass and waste-fired boiler environments	83

9.2 Part II- Potential corrosion challenges in chemical looping combustion of biomass	85
10. Outlook.....	87
10.1. Part I- Investigation of corrosion mechanisms in biomass and waste-fired boiler environments	87
10.2 Part II- Potential corrosion challenges in chemical looping combustion of biomass	87
11. References	89

1. Renewable fuels for heat and electricity production: motivation, opportunities and corrosion challenges

Over the past few decades, anthropogenic CO₂ emissions have increased significantly, with studies suggesting a correlation between rising atmospheric CO₂ levels and the increase in average global temperatures (Fig. 1.1) [1, 2]. Today, there is a consensus in the scientific community that limiting global warming to “well below 2 °C above pre-industrial levels” (the period of 1850–1900) is critical [3-5]. Exceeding this temperature-threshold may impose severe stress on the earth’s climate and ecosystems, resulting in more-frequent extreme weather events, such as droughts and heatwaves, with the consequence of populated regions may become uninhabitable in the near future [5-8]. Despite efforts to address the issue, the average global surface temperatures continue to rise (see Fig. 1.1). This suggests that the mitigation strategy has either been insufficient or has not been fully implemented [9].

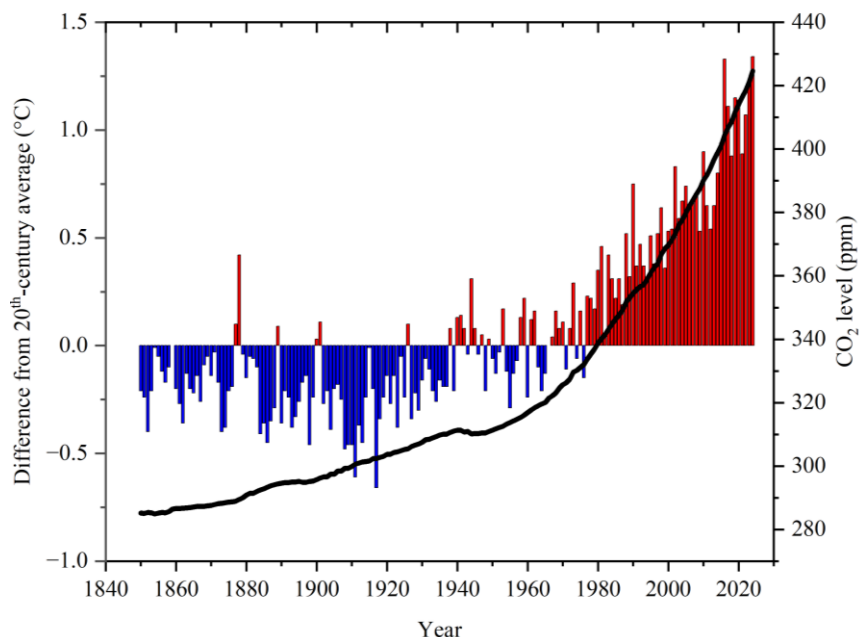


Fig. 1.1: Bar chart: Annual temperature deviations from the 20th Century average from Years 1850 to 2023, with red bars indicating warmer-than-average years and blue bars indicating colder-than-average years. Data from [10]. Line graph: Global atmospheric carbon dioxide levels (ppm) from 1850 to 2023. Data from [11, 12].

The energy sector has the potential to adopt more sustainable practices. The International Energy Agency (IEA) reports that electricity and heat production is the largest single source of global CO₂ emissions, accounting for approximately 40% of global CO₂ emissions as of Year 2022 [13]. This high number is primarily driven by the heavy reliance on fossil fuels [14]. To mitigate these emissions, the Intergovernmental Panel on Climate Change (IPCC) has emphasized the replacement of fossil fuels with sustainable alternatives, such as waste-derived and biomass fuels, in power and combined heat and power (CHP) plants, among other solutions [15]. According to the IEA’s annual coal market report from Year 2019, there are approximately 9,000 active coal-fired power plants globally, producing more than 10,000 TWh of electricity annually [14]. In contrast, global electricity generation from biomass in Year 2018, as reported by the World Bioenergy Association, totaled 637 TWh, including contributions from biomass that originated

from municipal and industrial waste sources [16]. These statistics highlight the current substantial gap in electrical generation volumes. While fully replacing fossil fuels will require a mix of renewable technologies, such as wind, solar, and hydro power, increasing the use of fuels that have a large proportion of biogenic sources in power plants remains a key factor in meeting future sustainable energy needs.

Heat and electricity are commonly generated in boilers through the combustion of fuel, producing thermal energy that converts water into superheated steam. This steam drives turbines for electricity generation. In addition to electrical output, power plants can improve overall energy efficiency by capturing and utilizing excess heat for district heating in nearby residential areas. Facilities that generate both electricity and useful thermal energy are referred to as combined heat and power (CHP) plants. CHP plants are common in colder regions, where a significant portion of their revenue comes from supplying district heating to local neighborhoods. One of the key technical challenges in the combustion of waste and biomass is corrosion. Corrosion refers to the gradual degradation of a material caused by chemical reactions with its surrounding environment, which can weaken the material's structure and functionality, ultimately resulting in premature failure. A particular concern when utilizing biomass and waste fuel in these combustion processes is the release of corrosive species into the flue gases, including alkali chlorides (KCl, NaCl), hydrogen chloride (HCl), water vapor, and heavy metal chlorides such as lead chloride ($PbCl_2$). These chemical species react with critical boiler components, such as the water walls and superheater tubes, causing severe corrosion that significantly reduces the lifetime of the metallic materials [17-22]. The corrosion rate and mechanism depend on factors such as material selection, temperature, fuel composition, and location in the boiler, leading to diverse impacts across the different parts of the boiler.

Due to this complex environment, boiler operators are compelled to maintain the superheated steam at relatively low temperatures, thereby lowering the material temperature, to minimize corrosion and prevent unscheduled boiler shutdowns. This, however, results in lower electrical efficiencies compared to fossil fuel-fired boilers. While waste-fired boilers typically achieve an electrical generation efficiency of 18%–26% [23], and biomass-fired boilers range from 25%–37% [24], coal-fired boilers have been reported to reach electrical efficiencies of up to 55% [25]. This disparity makes the transition from fossil fuels to waste and biomass combustion less appealing to key stakeholders, particularly in situations where the electricity output rather than heat recovery is the main source of revenue.

Despite extensive research on corrosion challenges in biomass- and waste-fired boilers, certain mechanisms remain unclear. For instance, in waste-derived fuels, heavy metal-containing compounds such as $PbCl_2$ are often detected in the deposits that form on the heat-exchange materials, such as the water wall tubes [26]. Although studies have shown that $PbCl_2$ is highly corrosive for various steel types, the corrosion mechanisms are not yet fully understood for low-alloyed steel, which is a common steel type used for water wall applications [18, 26-28].

One strategy to improve steam data when utilizing renewable fuel involves smart boiler design. Modern circulating fluidized bed (CFB) boilers have superheaters installed in the recirculation loop, called the ‘loop seal’, whereby the fluidizing bed material is recirculated back to the combustion chamber. In this region, heat transfer properties between the bed material and the superheater tubes is high, leading to greater heat transfer per unit area of tube surface, as compared

to superheaters positioned in the convective pass [29]. Furthermore, this area should in theory be less-corrosive than superheaters that are positioned in the convective pass. However, immersing superheater tubes in the fluidized bed material may raise other challenges, such as erosion or a mixture of erosion and corrosion [30]. Research on superheater material performance in the loop seal region remains limited, and it is important to understand the degradation mechanisms, in order to select the most-suitable materials that have high resistance to corrosion and erosion while ensuring cost-effectiveness.

There is growing recognition that the transition to more-sustainable heat and electricity production might not be sufficient to reach the ambitious 2 °C global climate goal. The IPCC AR6 Synthesis Report, published in Year 2023, states that significant carbon capture and storage (CCS) efforts must be implemented in the near future [31]. CCS involves the capture of CO₂ emissions from industrial processes, such as those in heat and electricity generation, before they are released into the atmosphere, thereby reducing overall greenhouse gas emissions. The captured CO₂ is then transported and stored in stable geologic features, making the CO₂ emissions net zero when using a fossil fuel. If instead the majority of the fuel is from biogenic sources, the realization of negative CO₂ emissions is within reach through the so-called Bioenergy with Carbon Capture and Storage (BECCS) technology. Currently, BECCS is recognized as one of the more-promising, large-scale, carbon-negative technologies [32]. As an example of the potential of BECCS, a study by the Swedish Government in Year 2020 suggested that the adoption of BECCS in biomass- and waste-fired boilers in Sweden could result in the uptake of 10 Mt CO₂/year by Year 2045 [33]. This figure would correspond to around 25% of the current total CO₂ emissions in Sweden [34]. However, many of the carbon capture technologies proposed for integration into power plants today are associated with a significant energy penalty, making their implementation a less-attractive investment. Chemical looping combustion (CLC), on the other hand, is a carbon capture combustion technology that has the potential to not only capture CO₂ with a low energy penalty but also to significantly enhance the efficiency of power plants that utilize renewable fuels [35]. This boost in efficiency is, however, based on the assumption that minimal corrosive species are transported to the air reactor (AR). Nevertheless, studies have shown that there may be slippage of volatile alkali to the AR during the combustion of biomass, which could affect the corrosive environment and, thereby, the maximum steam data levels achieved [36, 37]. Despite the pivotal role that corrosion is expected to play in achieving the desired steam data, there have to date been surprisingly few efforts to study this issue.

Not only is there a demand for more corrosion-resistant materials from the industry, but there is also a great need to increase the predictability of material degradation, thereby avoiding costly forced shutdowns during peak seasons. Reliable corrosion kinetic models would improve material selection and ensure more-effective maintenance planning, leading to higher efficiency and fewer unexpected failures. However, modeling corrosion kinetics remains a significant challenge due to the complex and harsh conditions that exist inside biomass- and waste-fired boilers. Sudden increases in corrosion rates can be caused by a variety of operational conditions, including shifts to more-corrosive fuels, soot blowing, thermal fluctuations, and others operational parameters, making it difficult to isolate and quantify the individual effects. The kinetics of corrosion in superheater tubes, however, are also heavily influenced by the oxide microstructure, with factors such as oxide grain size and oxide phases playing crucial roles in the diffusion rate of ions through the oxide scale. While many studies have focused on modeling operational parameters to predict

high-temperature corrosion of superheaters [38], there have been no attempts to develop a kinetics model that explores the relationships between material degradation, oxide microstructure, and operational conditions. One of the challenges in addressing this is the difficulty associated with securing suitable sample preparation methods that allow for the characterization of oxide scales from samples exposed in a commercial boiler at the nanoscale, while also ensuring high statistical reliability of the results.

1.1 Objectives

This thesis addresses corrosion challenges associated with the combustion of biomass and waste-derived fuels for heat and electricity generation. The primary objective is to enhance the understanding of corrosion mechanisms under these conditions, thereby supporting the selection of suitable materials which can ultimately contribute to improved plant efficiency. The work carried out in this thesis is divided into two parts: **Part I** focuses on corrosion issues observed in operating boilers using biomass or waste-derived fuels, while **Part II** examines potential corrosion challenges associated with chemical looping combustion (CLC) of biomass.

1.1.1 Part I- Investigation of corrosion mechanisms in biomass and waste-fired boiler environments

In **Paper I**, I investigate the degradation rates and mechanisms of several different alloy types that were exposed in the loop seal region of an 80-MW_{th} CFB waste-fired boiler for up to 12 months. The following questions were addressed:

- ❖ What type of alloy material is suitable for this application?
- ❖ Does corrosion or erosion exert the strongest influence on the degradation rate of the material, or is there a synergism between erosion and corrosion?

For this study, microstructural analyses were performed on the materials of interest using scanning electron microscopy (SEM) coupled with energy-dispersive x-ray (EDX) spectroscopy.

In **Paper II**, I address the knowledge gap related to the initiation and propagation mechanisms of PbCl₂-induced corrosion on a low-alloyed steel (T22) at 400 °C in a humid atmosphere. This was achieved by implementing a time-resolved experimental approach, in which we exposed T22 to PbCl₂ for 1, 24 and 168 hours in an isothermally controlled, laboratory-scale environment. The following research questions were addressed:

- ❖ How do the individual elements (Pb and Cl) affect the corrosion rate?
- ❖ How do the initiation and propagation mechanisms differ from each other?

Microstructural analyses were carried out on carefully prepared ion beam-milled cross-sections. The analyses were performed using SEM coupled to EDX and x-ray diffraction (XRD).

In **Paper III**, the objective was to develop a new framework for lifetime prediction models of superheaters used in waste-fired boilers. This was achieved by establishing a practical microstructural characterization method that enables the analysis of oxide grain size in samples exposed to commercial boilers. This grain size data was then incorporated into a DICTRA-based diffusion model to simulate the corrosion rate. Furthermore, the effect of chlorine load on the corrosion kinetics was incorporated, with chlorine presence modeled to reduce the activation energy for grain boundary diffusion. The simulated corrosion kinetics were then compared with

measured corrosion kinetics on a superheater tube exposed for roughly 4 years in a waste-fired boiler. The following research questions were discussed:

- ❖ What role does the detailed analysis of oxide grain size play in understanding the corrosion kinetics in superheater tubes, and how can this information be used to improve lifetime prediction of alloys in the present environment.
- ❖ What key factors should be considered when discrepancies arise between predicted and measured corrosion kinetics, and how can these factors be incorporated into models to improve lifetime predictions?

Microstructural analyses were carried out on carefully prepared ion beam-milled cross-sections. The analyses were performed using SEM coupled to EDX. The kinetic simulations were carried out using the software package DICTRA (**D**iffusion **C**ontrolled phase **T**RAnsformation).

1.1.2 Part II- Potential corrosion challenges in chemical looping combustion of biomass

In **Paper IV**, I address the knowledge gap regarding high-temperature corrosion in CLC that utilizes biomass as fuel. This was done by developing an experimental set-up that simulates the conditions relevant for superheater applications in the AR side of CLC of biomass fuel. Here, the focus was on two scenarios: 1) no release of alkali in the AR; and 2) continuous release of alkali in the form of KOH(g) in the AR. The following research questions were addressed:

- ❖ What material is suitable for superheater applications in the AR side of a CLC unit combusting biomass?
- ❖ How does significant alkali release affect the corrosion rates of the different materials and, consequently, their suitability for use as superheaters?

Microstructural analyses were carried out on carefully prepared ion beam-milled cross-sections. The analyses were performed using SEM coupled to EDX and x-ray diffraction (XRD).

2. Combustion of biomass and waste

Replacing fossil fuels with waste-derived or biomass fuels for energy conversion presents challenges that stem from the chemical characteristics of the fuel itself. Table 1.1 compares with coal the fuel characteristics of various biomass sources that are relevant as fuels for heat and electricity production. It is clear that biomass sources typically differ from coal, particularly with respect to higher alkali content, moisture levels, and chlorine concentrations, while having a lower sulfur content. As a result, the combustion of biomass produces relatively high levels of HCl(g), H₂O(g), alkali chloride, and alkali-rich ash, which have been linked to accelerated corrosion of critical boiler components, such as water walls and superheater tubes [39, 40].

Table 1.1: Estimated chemical compositions, moisture contents, and ash yields for selected fuels relevant for heat and electricity production [41-45].

Fuel type	Moisture content (wt.%)	wt.% dry-basis			
		S	Cl	K	Ash
Coal	6–10	0.5–3.1	<0.01	<0.01	8–40
Straw	17–25	0.05–0.2	0.14–1.05	0.69–1.30	8.6
Wood	5–60	<0.05	0.01–0.03	0.02–0.05	0.2–0.6
Bark	45–65	<0.05	0.01–0.05	0.1–0.4	3.7

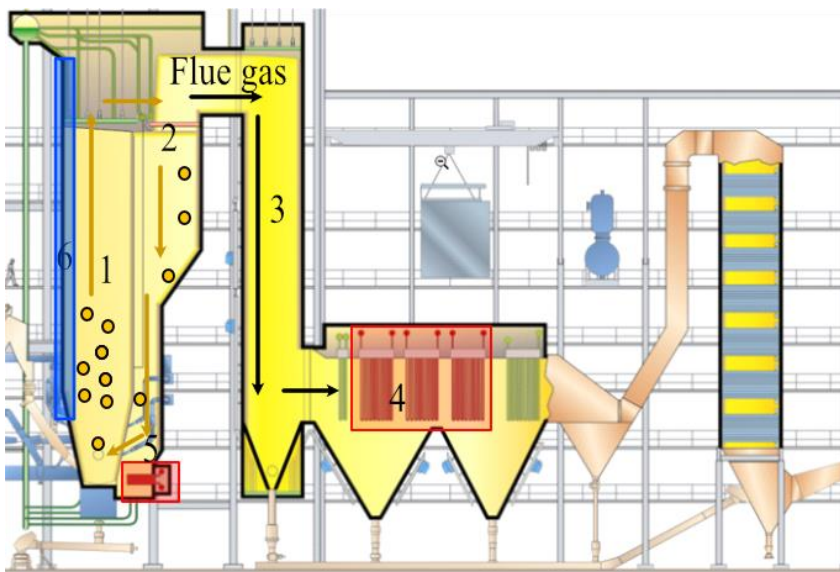
Unlike fossil fuels and biomass, waste streams are generally more heterogeneous and can consist of anything from biomass and plastics to electronics. Thus, waste streams may contain high fractions of alkali from biomass, as well as Cl that originates from both biomass and plastics such as PVC [46]. In addition, waste streams can contain high concentrations of heavy metals, such as Pb and Zn, which often originate from batteries, plastics and electrical devices. High levels of Pb are also detected in treated sustainable materials, such as recycled waste wood (RWW), which is a key fuel source for heat and electricity production in many European countries [27]. The presence of Pb in RWW is associated with lacquers, preservatives and siccative, which are used as surface treatments for wood in the furniture and building industries [47] [48]. Kinnunen analyzed the elemental composition of 100 different RWW fuels used in European waste-fired boilers, comparing them with bark-free stem wood [49]. That study found that RWW contains approximately 480-times more Pb than stem wood due to surface contaminants. A similar study carried out by Krook et al. compared the Pb levels in RWW to those in pine and spruce stem wood, revealing that the RWW used in three large (CHP) plants in Sweden contains 480–1,638-times more Pb than pine and spruce-derived stem wood [47]. As will be discussed in *Section 5.5*, PbCl₂ plays an important role in accelerating corrosion of the water wall tubes in waste-fired boilers.

2.1 Circulating fluidized bed boiler

The two main boiler technologies used for the combustion of biomass and waste-derived fuels include grate-fired boilers and fluidized bed (FB) boilers (including bubbling fluidized and circulating fluidized bed (CFB) boilers) [50]. While their designs vary, they share the fundamental principle of converting the fuel's stored energy into heat, which is then used to produce superheated steam for electricity and heat generation. Since the research presented in **Papers I** and **III** of this thesis was conducted in a CFB boiler, the following section provides a brief overview of this combustion technology.

Fig. 2.1 depicts a CFB boiler at the Händelö CHP plant in Sweden. In a CFB boiler, combustion takes place in direct contact with the circulating bed material. The bed material typically comprises sand, as well as recirculated ash from the combustion process when combusting biomass or waste. The fuel is introduced into the combustion chamber (see Region 1 in Fig. 2.1), where primary air is injected from the bottom to ensure steady combustion and maintain the bed material in a fluidized state. Part of the bed material with sufficiently small particle sizes is then transported from the combustion chamber to the cyclones (Region 2), where the bed material is separated from the flue gas and fly ash through centrifugal and gravimetric forces [28]. The separated bed material is recirculated back to the furnace chamber via a loop seal (Region 5), which is equipped with its own air inlet to ensure rapid transportation and to minimize the risk of agglomeration of the fluidized medium. If an aggressive fuel is combusted, CFB boilers may include an empty pass (Region 3), where the flue gas is transported after the cyclone. One of the purposes of the empty pass is to lower the flue gas temperature, allowing corrosive species to condense before the gas reaches the superheaters in the convective pass (Region 4) [51].

Two important components in the steam-water cycle in a CFB boiler are the waterwall and the superheater tubes, highlighted as blue and red regions, respectively in Fig. 2.1. The water walls are typically situated along the walls of the combustion chamber and are filled with water, which absorbs heat from the combustion process, converting the water into saturated steam. The material temperature of the water walls is kept at around 300°–400 °C during the combustion of biomass and waste [52]. This relatively low temperature promotes the condensation from the flue gas of chemical elements such as alkali, chlorine, and Pb-containing compounds, which are known to accelerate the corrosion of water wall materials [52]. In the superheater tubes, the steam undergoes its final heating stage, resulting in the production of superheated steam. Here, the material temperatures are typically in the range of 400°–600 °C, depending on the fuel being burned and the positions of the superheaters. The final superheating of steam is typically carried out in the convective pass of the boiler (Region 4 in Fig. 2.1). Although the empty pass helps to reduce the corrosive species reaching the convective pass, studies have linked high corrosion rates to alkali- and chlorine-rich deposits on the superheating tubes [53]. As an approach to improving the steam data, modern CFB boilers employ a strategy of final steam heating in the loop seal region (Region 5) [53, 54]. By placing superheaters in this region, direct contact is achieved between the superheater tubes and the FB material, thereby improving the heat transfer properties [29]. Furthermore, because this region is positioned after the cyclone, it should, in theory, create an environment with low concentrations of corrosive species.



- Bed material
- 1. Combustion chamber
- 2. Cyclones
- 3. Empty pass
- 4. Convective pass
- 5. Loop seal region
- 6. Water walls

Fig. 2.1: Schematic of a CFB boiler, as designed by Sumitomo SHI FW. Courtesy of E.ON AB.

CFB boilers are recognized for having high fuel flexibility, which makes them suitable for the combustion of various large-scale solid fuels, including biomass, municipal solid waste (MSW), sludge, industrial waste, and recycled wood. However, the challenges associated with CFB combustion include the need to prepare the fuel by reducing the average fuel particle size. This step is essential to ensure that the fuel remains appropriately fluidized during combustion. In addition, a high alkali content can cause the sand bed particles to agglomerate, and in extreme cases, this can result in the complete defluidization of the bed and unscheduled maintenance [51, 55]. In terms of mitigating this issue, studies have shown that substituting the bed material with olivine $[(\text{Mg},\text{Fe})_2\text{SiO}_4]$ or ilmenite (FeTiO_3) can reduce the extent of agglomeration [56, 57].

2.2 Integration of carbon capture technology into power plants

As discussed in *Section 1*, there are several reports emphasizing the need to achieve negative net-CO₂ emissions to meet global climate goals [31]. This can be achieved by integrating CO₂ capture techniques into power plants that operate on renewable fuel in what is commonly referred to as 'Bioenergy with Carbon Capture and Storage' (BECCS). In the EU, it is estimated that roughly 50% of all waste combusted in power plants originates from a renewable source [46]. Furthermore, according to the Confederation of European Waste-to-Energy Plants (CEWEP), there are 497 waste-to-Energy plants in the EU, with the capacity to supply electricity to over 21 million people, highlighting the region's significant potential to achieve negative net-CO₂ emissions in this sector [58]. Descriptions of some of the most commonly discussed carbon capture technologies for implementation in power plants are provided in the following sections.

2.2.1 Post-combustion

The only two large-scale power plants in the world that have integrated CO₂ capture are the Boundary Dam Carbon Capture Project in Canada and the Petra Nova CCS Project in the USA [59]. Both power plants run on fossil fuels and utilize the so-called 'post-combustion' CO₂ capture method. Specifically, the amine-based process is used, which is one of the most industrially mature methods for large-scale CO₂ capture [60]. In this process, fuel is combusted in air, producing flue gas that is directed to an absorber–stripper system. Within the absorber, the flue gas comes into

contact with an aqueous amine solution that selectively captures CO₂ through chemical absorption. The resulting CO₂-rich solvent is subsequently transferred to a stripper column, where it is regenerated, releasing a concentrated CO₂ stream and allowing the amine solvent to be recycled back to the absorber [61]. The advantages of this technology are its high technology readiness level (TRL) and that it can be retrofitted into existing power plants relatively easily. Furthermore, this technology has been designed to achieve a CO₂ capture efficiency of approximately 90% when operated with no downtime [59].

Nevertheless, there are some challenges associated with the amine-based process. For instance, in order to regenerate the amine solution, heat is required. This is supplied from the power plant's primary steam cycle or from a secondary steam cycle and is associated with a large energy penalty [35, 59, 62]. The high energy penalty of solvent regeneration has been reported as a reason for why the Boundary Dam project typically operates at only 65%–85% of its CO₂-capturing capacity [63]. The Petra Nova power plant has bypassed the energy penalty of using steam from the existing steam cycle by powering the CO₂ capture unit with a natural gas-fired power plant, which generates more steam than the CO₂ capture unit requires. While this boosts the net power output, it comes with very high capital costs and undermines the environmental motivation of mitigating CO₂ emissions, as the combustion of natural gas increases such emissions [59].

Efforts to implement CO₂ capture in existing power and CHP plants using renewable fuels for negative CO₂ emissions are ongoing. The Swedish utility company Stockholm Exergy has secured EU funding to support the construction of one of the world's largest facilities for biogenic CO₂ capture, integrated with a biomass-fired CHP plant, and aiming to capture 800 KtCO₂ by Year 2026 [64]. They have opted to utilize the so-called hot potassium carbonate (HPC) process, primarily due to its high TRL. In similarity to the amine-based process, the HPC CO₂-capture process occurs post-combustion and can be retrofitted into existing power plants. However, instead of an amine solution, this method uses potassium carbonate as absorption solvent [65] [66]. A study carried out by Levihn et al. on the installation of a CO₂ capturing system for this particular case has reported that the energy penalty associated with the HPC method may end up being higher than that linked to the amine solvent process, making it less financially viable when the revenue is based exclusively on electricity production [66]. However, it is also mentioned in the same study that this technology can be viable in CHP plants, as the excess heat used to regenerate the potassium carbonate solvent can be repurposed to generate revenue from district heating.

It is important to note that the implementation of post-combustion carbon capture technologies in conventional biomass or waste-fired boilers will not alter the process of superheated steam production. Thus, these technologies not only impose a high energy penalty for CO₂ capture, but they also fail to address the reduced electrical efficiency associated with the corrosive flue gases formed during the combustion of biomass and waste.

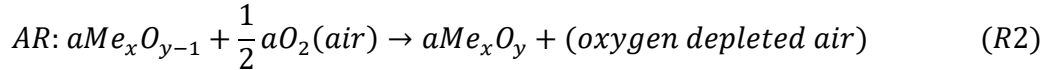
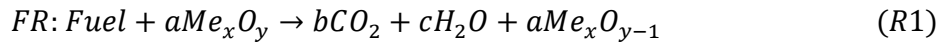
2.2.2 Oxy-fuel combustion

In the oxy-fuel combustion carbon capture technology, molecular oxygen is separated from the air before entering the boiler. This step occurs in an air separating unit (ASU). Thus, the fuel is combusted with a high concentration of oxygen, and the flue gas primarily consists of CO₂ and H₂O. Since there is minimal nitrogen present, it becomes significantly easier to separate CO₂ compared to the post-combustion technology. The main challenge associated with oxy-fuel combustion is the production of a high concentration of oxygen in the ASU. This is typically

achieved in a cryogenic environment and is highly energy-intensive [67]. Despite the high energy demand, techno-economic analyses suggest that this technology holds promise for CCS [67]. It has been reported that a large fraction of the flue gas, typically between 60% and 80%, will have to be recycled to the boiler to moderate the flame temperatures during combustion [67-70]. This can be problematic as it may generate higher concentrations of water vapor and Cl-containing species, as compared with conventional air-aided combustion, and consequently, accelerate corrosion in the superheaters [71-73].

2.2.3 Chemical looping combustion

Chemical looping combustion (CLC) is a CO₂ capture technology that offers the potential to not only capture CO₂ with a low energy penalty, but also to improve the steam data during the combustion of biomass and waste, a distinct advantage over the CO₂ capture technologies presented above [74]. An illustration of the CLC concept is shown on Fig. 2.2. CLC operates with two interconnected FB reactors: the fuel reactor (FR) and the air reactor (AR). The fluidizing medium in CLC comprises of a so-called ‘oxygen carrier’, which serves a dual purpose: it aids in the fuel conversion process, while also acting as the FB material. The oxygen carrier (OC) is typically made up of metal oxides, such as Fe, Mn, and Cu oxides, and ilmenite (FeTiO₃), among others [75, 76]. In the FR, the OC supplies the oxygen required for fuel conversion, resulting in a flue gas composed primarily of H₂O and CO₂ [35]. The reduced OC (Me_xO_{y-1}), is then transported to the AR, where it oxidizes in contact with air, maintaining a continuous loop:



Since fuel conversion occurs without direct contact with air, a minimal level of nitrogen is expected in the flue gas leaving the FR. Thus, the energy penalty for separating CO₂ is expected to be low [35]. Although no commercial CLC units are currently in operation, laboratory- and pilot-scale tests utilizing solid biomass as fuel have been reported [77-79]. For instance, CLC operated with various biomass fuels, using manganese ore and ilmenite as the OC in a 10-kW and 100-kW pilot unit at Chalmers University of Technology, was able to achieve a carbon capture rate of >94% [78, 79]. Furthermore, studies conducted by Langørgen et al. in a 150-kW CLC pilot unit have yielded promising results with the use of solid recovered waste-derived material (SRF), achieving a carbon capture rate >95% [80].

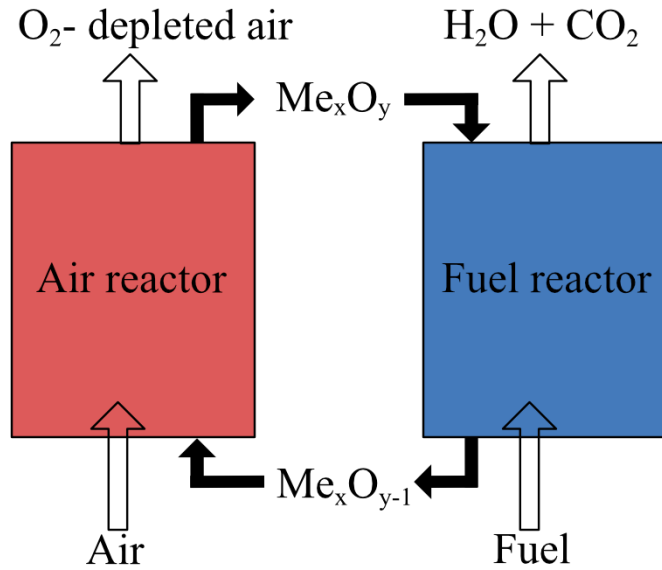


Fig. 2.2: Illustration of the chemical looping combustion concept.

The inherent two-reactor arrangement of CLC is particularly interesting when it comes to heat and electricity production. The AR is expected to maintain a non-corrosive environment, regardless of fuel type, since it is separated from the fuel conversion step that takes place in the FR. Furthermore, the oxidation of the OC in the AR (Reaction 2) is exothermic. From the corrosion perspective, if one places the final heating of the steam in this region of a CLC unit, enhanced steam performance for biomass and waste fuels should be feasible, potentially reaching levels comparable to today's advanced coal-fired boilers (Fig 2.3).

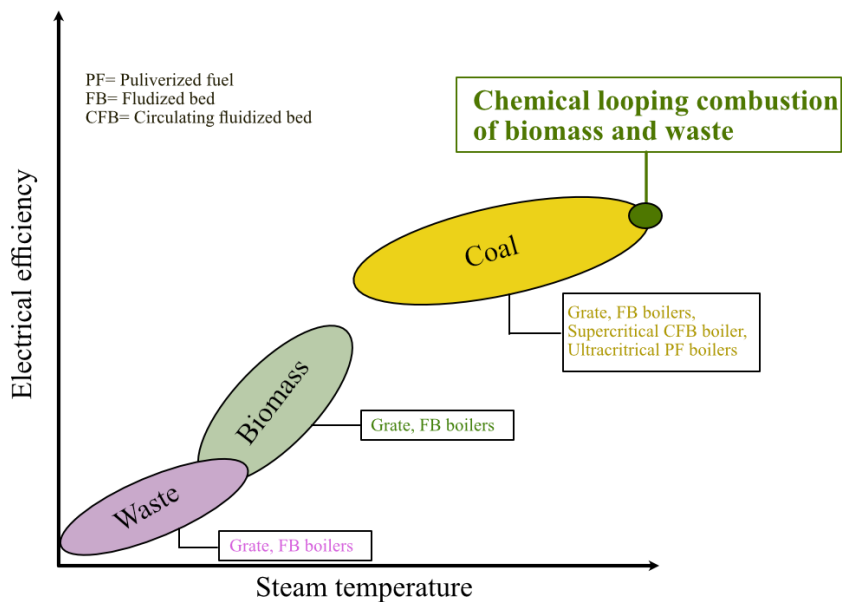


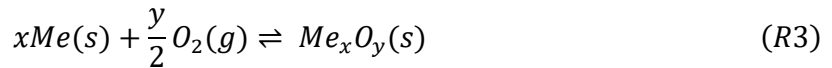
Fig. 2.3: Illustration of the potential for improving electrical efficiency from chemical looping combustion of a renewable fuel (biomass or waste), as compared to using conventional boiler technologies and various fuel types (adapted from [81]).

3. High-temperature corrosion

Resistance to high-temperature corrosion relies heavily on the ability of an alloy to form a protective oxide scale. Understanding the thermodynamics and kinetics of oxide formation on a metal surface enables predictions of which oxides will form and their protective properties under specific conditions. This knowledge is essential for selecting suitable materials and for developing effective corrosion-mitigation strategies for high-temperature applications.

3.1 Thermodynamics

Exposing a non-noble metal to high temperatures in an oxidizing environment inevitably results in the metal becoming oxidized. The driving force for the oxidation of metals originates from the principle of the second law of thermodynamics [82]. Consider the following oxidation of a metal (*Me*) when exposed to oxygen (*O*) and where *x* and *y* are stoichiometric constants:



Assuming that the temperature (T) and pressure (P) are constant, it is possible to predict whether or not the reaction is occurring spontaneously by calculating the change in the Gibbs free energy (ΔG) of the reaction:

$$\Delta G = \Delta H - T\Delta S \quad (Eq. 1)$$

where *H* is the enthalpy, *T* is the temperature, and *S* is the entropy of the system. A negative value of the Gibbs free energy, $\Delta G < 0$, indicates that a spontaneous reaction is expected, i.e., the metal will undergo oxidation. Conversely, a positive ΔG value describes a thermodynamically unfavorable reaction, whereas if $\Delta G = 0$ the chemical reaction has reached equilibrium [83].

The Gibbs free energy per mole of oxygen can be expressed as follows:

$$\Delta G = \Delta G^\circ + RT \ln\left(\frac{a_{(Me_xO_y)(s)}}{a_{Me(s)}^x * a_{O_2(g)}^{\frac{y}{2}}}\right) \quad (Eq. 2)$$

where ΔG° is the standard Gibbs free energy, *R* is the universal gas constant, *T* is the temperature, and *a* represents the chemical activity of the reactant and products [84]. As the chemical activity of a pure solid substrate equals unity and the activity of any gas compound can be expressed as an ideal gas, Eq. (2) in equilibrium ($\Delta G = 0$) can be rearranged as follows:

$$\Delta G^\circ = RT \ln(p_{O_2}^{y/2}) \quad (Eq. 3)$$

The p_{O_2} is referred to as the dissociation pressure of oxygen, which is the minimum oxygen partial pressure at which the oxide remains thermodynamically stable at a given temperature. From Eq. (3) we can understand that the formation or dissociation of an oxide dependent on the temperature and p_{O_2} [84]. The temperature and oxygen partial pressure dependence of the Gibbs free energy for oxidation of metals is effectively shown in the Ellingham-Richardson diagrams (Fig. 3.1). The further down the line in the diagram, the more negative the Gibbs free energy becomes, and thus the greater stability of the oxide. Relevant oxides for this work are shown in Fig 3.1. For example, at 400 °C Al_2O_3 is more thermodynamically stable than Cr_2O_3 followed by Fe_3O_4 and Fe_2O_3 .

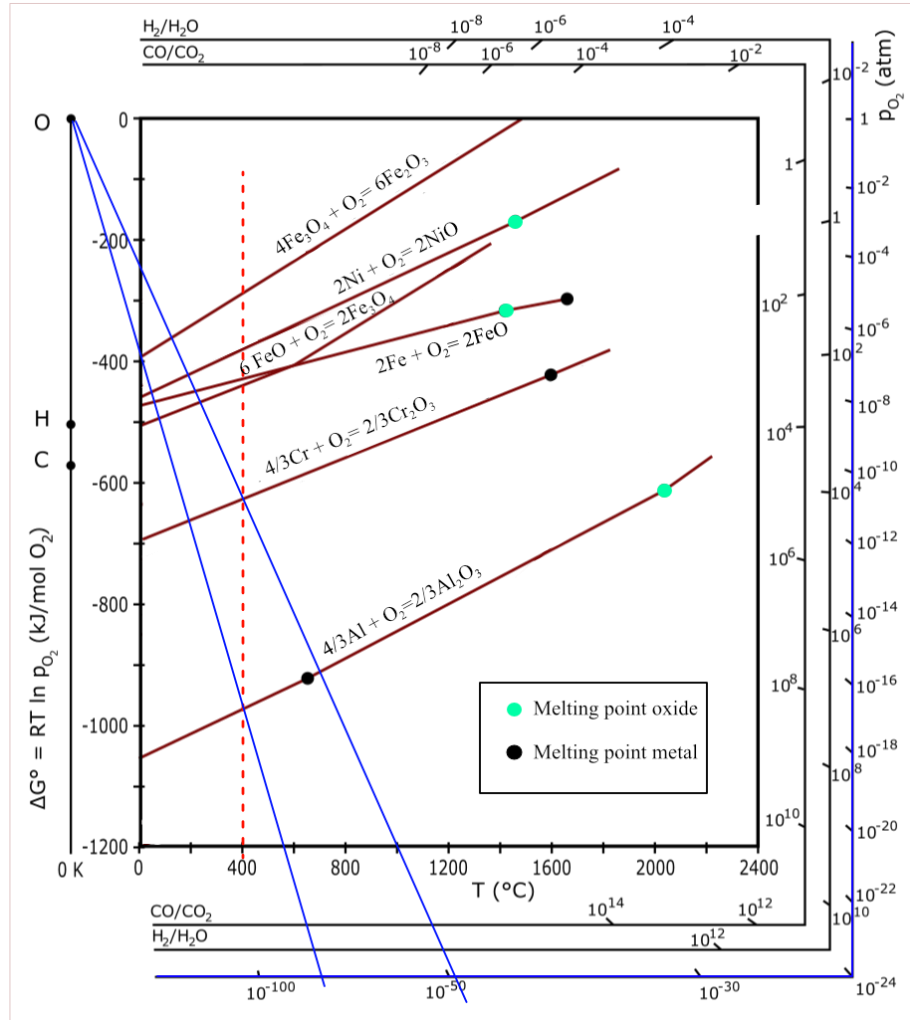


Fig. 3.1: Ellingham-Richardson diagram, adapted from [82].

Thermodynamics helps to determine whether oxide formation occurs spontaneously in a given environment, providing valuable insights for designing alloys and predicting the compositions needed to form protective and selective oxides. Furthermore, thermodynamic equilibrium calculations and the assumption of equilibrium are important tools for modelling high temperature corrosion [28, 85, 86]. While thermodynamics describes the potential of oxide formation, kinetic factors, such as diffusion through the metal and oxide, are important to consider to fully understand and predict oxidation rates.

3.2 Oxide growth

The growth of an oxide scale on a metal surface is often described in terms of a three-step process (Fig. 3.2). The initial step involves the adsorption of oxygen from the surrounding environment onto the metal surface. Charge transfer occurs between the adsorbed oxygen and the metal to form O^{2-} , which reacts with metallic cations (Me^{n+}) to allow the formation of individual oxide nuclei. These oxide nuclei then proceed to grow parallel to the metal surface until the entire surface is covered. Once the surface is completely covered (Step 3 in Fig. 3.2), oxide growth is governed by the solid-state diffusion of ions through the oxide scale. Consequently, if the oxide scale remains intact the oxidation rate decreases over time, since it takes longer time for ionic species to diffuse through the oxide scale as it becomes thicker.

At high temperatures, Steps 1 and 2 in Fig. 3.2 occur rapidly and Step 3 is generally considered as the rate-determining step for the corrosion attack. Accordingly, research on high-temperature corrosion processes in biomass- and waste-fired boilers has focused on the protective properties of the oxide, associated with Step 3.

Oxide growth

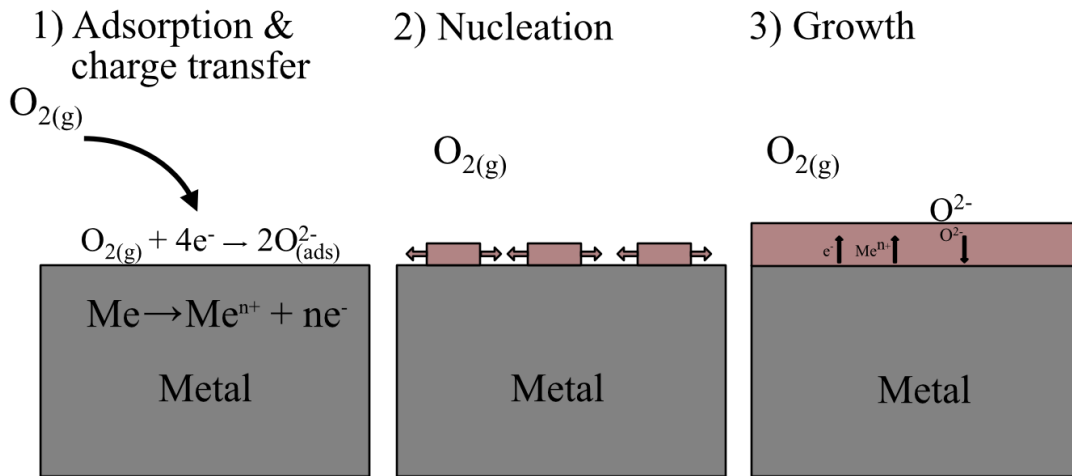


Fig 3.2: Oxide growth mechanism.

3.3 Kinetics

Various techniques are available to monitor corrosion kinetics, with the selection influenced by factors such as environmental conditions and the required temporal or spatial resolution. Often, multiple methods are used in combination to achieve a more comprehensive understanding.

The most widely used method for determining corrosion rates is the monitoring of oxide accumulation over time. This is typically done in laboratory-scale exposures by determining the mass change of the substrate from before and after exposure as a function of time. By connecting a laboratory furnace with a balance, the mass change can be measured continuously by thermogravimetric analysis (TGA). A key advantage of continuous measurement is that mass changes are recorded during the exposure and can be directly attributed to the interaction between the oxide scale and the environment, providing data for highly detailed kinetics. Furthermore, TGA minimizes the mass gain errors caused by post-exposure effects, such as oxide spallation during cooling or sample handling. However, the thermogravimetric equipment is costly, and discontinuous measurements, especially for longer exposure times, are used more often [84].

Another approach to evaluate oxide accumulation is by measuring the oxide thickness. This is typically accomplished through microscopy of prepared cross-sections following exposure. This can be beneficial in laboratory-scale exposures simulating corrosive environments, where the observed mass changes can be influenced by additional factors, such as salt condensation, evaporation of elements from the oxide, and the formation of other corrosion products unrelated to oxide growth. Therefore, in this scenario, gravimetric data alone may not accurately reflect the growth of the oxide scale. Compared to mass gain analysis, oxide scale evaluation with cross-sections works on different scales, which can be both beneficial and limiting. For example, in cases of highly localized corrosion, the overall mass gain of the sample may mask the mass changes that are occurring within the active corrosion region, which can be critical for the lifetime of the

material. In such instances, cross-sectional analysis of the oxide scale at the localized site of attack can offer more-meaningful insights into the corrosion behavior. Nevertheless, this method is destructive, as it requires cutting the sample [84].

In a complex environment, e.g., biomass and waste-fired boilers, the harsh conditions and often long exposure times can result in relatively thick oxide scales that are building up internal stresses. These stresses frequently lead to spallation of both the oxide and surface deposits, either during exposure or during post-exposure preparation. As a result, methods based on oxide thickness or mass gain become less accurate and may not represent the oxide kinetics. In such cases, a more-reliable approach is to measure material loss, specifically the rate of metal consumption. This can be achieved by measuring the material thickness before and after exposure using ultrasonic measurements or a combination of ultrasonic and microscopy techniques [84].

Accurately interpreting corrosion kinetics is crucial for developing predictive models that can reliably estimate the long-term performance and lifetime of metals or alloys in specific environments. The three most widely used kinetic rate laws to describe oxide kinetics are: linear, parabolic, and logarithmic (Fig. 3.3). While oxide thickness is used as a representative example for these rate laws, the underlying rate laws are not limited to oxide scale growth. They are equally applicable to related parameters such as mass gain or material loss, depending on the focus of the investigation.

3.3.1 Linear rate law

When the oxide growth is constant with time, the oxidation kinetics follow a linear rate law, Eq. (4):

$$X = k_l t + C \quad (\text{Eq. 4})$$

where X is the oxide thickness, k_l is the linear rate constant, t is time, and C is a constant. The rate determining step for linear oxidation can be a surface or phase boundary process or a reaction. Scenarios in which linear growth may arise include environments with a low partial pressure of oxygen, thin oxide scales, or an oxide scale that is highly porous. In the latter case, the growth of the oxide scale has no bearing on the oxidation rate, since oxidants are transported to the metal surface by gas diffusion through the pores, rather than by ionic diffusion through the oxide [82].

3.3.2 Logarithmic rate law

When the oxide growth is behaving logarithmically, it can be described as in Eq. (5):

$$X = K_{log} * \log(t + t_0) + C \quad (\text{Eq. 5})$$

where X represents the oxide thickness, K_{log} represents the logarithmic rate constant, and C is a constant. In this scenario, the initial oxidation rate is high but quickly decreases to a negligible level. This behavior is typically observed at relatively low temperatures (300°-400 °C) and for very thin oxide layers (thicknesses of up to approximately 4 nm). The exact rate-determining step for this oxidation regime remains unclear. Various hypotheses have been proposed, including chemisorption and the transport of electrons from the metal to the oxide-gas interface driven by an electric field; however, a clear consensus has not yet emerged [82].

3.3.3 Parabolic rate law

If the oxide layer is sufficiently thick and dense to isolate effectively the gas from direct contact with the metal surface, its growth can be expressed by a parabolic rate law:

$$X^2 = K_p t + C \quad (\text{Eq. 6})$$

where X is the oxide thickness, K_p is the parabolic rate constant, t is time, and C is a constant [82]. In this case, solid-state diffusion of ions through the oxide scale becomes the rate-limiting step for oxide growth. Since the oxide growth rate is proportional to the square root of time ($X \propto t^{0.5}$), the growth rate of the oxide slows as time progresses [82]. By plotting the oxide thickness (X) vs \sqrt{t} , the rate of parabolic growth is confirmed if a linear relationship is observed. From this, the slope of the line can be determined, and this represents the parabolic rate constant (K_p). Once K_p is known, it can be used to support lifetime predictions and modeling of oxide growth over longer exposure times and at various temperatures.

The parabolic growth rate model was first established by Tammann [87] and further developed by Wagner in 1930 [88]. The presented model is rather idealized, and several assumptions have been made, such as:

- ❖ Thermodynamic equilibrium is established at the gas/oxide and oxide/metal interfaces, as well as throughout the oxide layer.
- ❖ The oxide layer is adherent and compact.
- ❖ The rate-controlling process is driven by lattice diffusion of ionic species through the oxide scale, i.e., no consideration of crystal defects such as grain boundaries and dislocations.
- ❖ Oxygen solubility in the metal is negligible.

Some oxides may display sub-parabolic oxidation behavior, characterized by a deviation from the parabolic rate law, with the oxidation rate either decreasing or increasing more rapidly than at a parabolic rate. This phenomenon has been attributed to mechanisms such as oxide grain coarsening and changes in the elemental composition of the oxide scale as a function of time [89, 90].

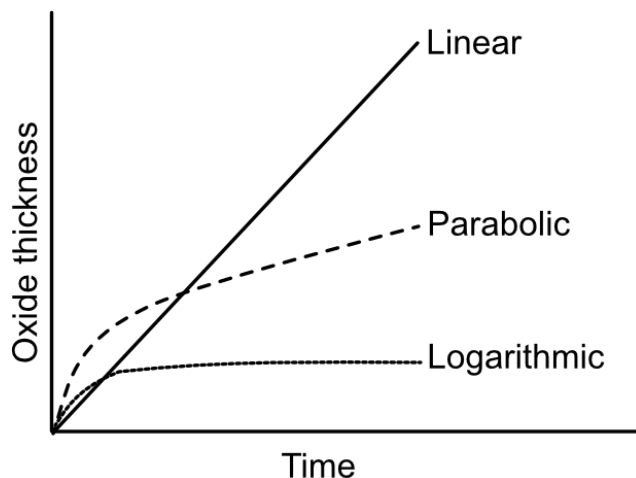


Fig 3.3: Illustration of the common kinetic rate laws describing oxide growth at high temperatures.

3.4 Diffusion paths through oxides

Oxides are ionic crystals, consisting of a structured arrangement of metal cations and oxygen anions. However, most oxides are not free from defects. Various types and degrees of point and surface defects are typically present, which influence the diffusion of charged species through the oxide scale. Diffusion of charge species occur through either *lattice diffusion*, i.e., transportation of charged species via point defects in the lattice structure, or *short circuit diffusion*, whereby diffusion occurs along surface defects such as grain boundaries [91]. The relative contributions of the two diffusion processes are highly dependent upon the temperature, grain size, and lattice defect concentrations [82].

The most-common point defects for oxides are Schottky and Frenkel pairs (Fig. 3.4). Schottky defect, constitute a cationic vacancy that is charge balanced by an anionic vacancy. A Frenkel defect involves charge compensation for a cation or anion vacancy through the presence of an interstitial cation or anion, respectively. Lattice diffusion through an oxide scale occurs by means of point defects, according to the following mechanisms (Fig. 3.4):

- ❖ Vacancy diffusion: Occurs in the presence of vacancy defects within the crystal lattice. An ion occupying a regular lattice site migrates into a neighboring vacant site, creating a new vacancy in its original position [82].
- ❖ Interstitial diffusion: Involves the movement of ions positioned in the interstitial sites to an adjacent interstitial site [82].
- ❖ Interstitialcy diffusion: Involves the movement of ions positioned in the interstitial site to an occupied lattice site, forcing the ion to move to an adjacent interstitial site [82].

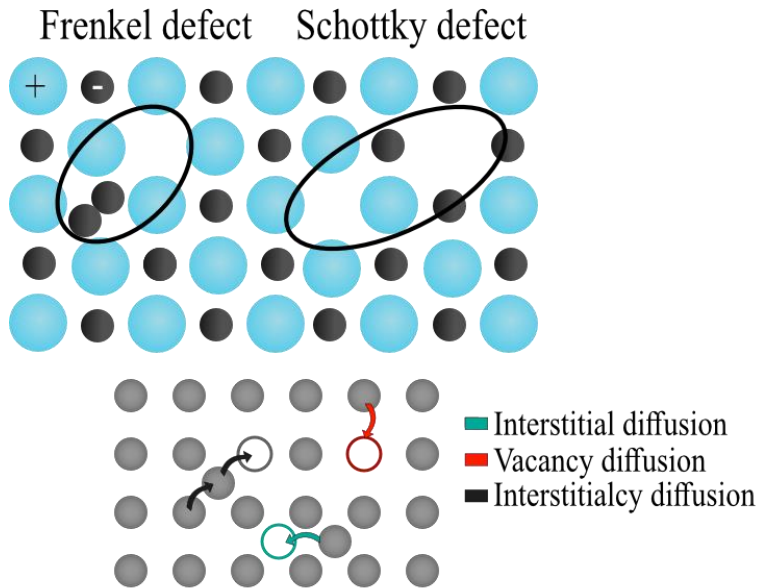


Fig. 3.4: Illustration of Frenkel and Schottky defects and the different mechanisms of lattice diffusion.

A low concentration of lattice defects results in relatively slow diffusion of charged species through oxide, promoting the formation of slow-growing oxides in mildly corrosive environments. For alloys that are relevant for biomass and waste-fired boilers, such as stainless steels, Ni-base alloys, FeCrAl alloys, and low-alloyed steel, this is exemplified by Cr₂O₃, α-Al₂O₃ and Fe₂O₃, respectively.

It is generally accepted that at service temperatures for water walls and superheaters, short-circuit diffusion of ions via line defects, such as grain boundaries of crystalline solids proceed more rapidly than lattice diffusion [92-95]. A grain boundary is the interface between two oxide grains with misaligned crystal structures, separating regions of the crystal that have different crystallographic orientations (see Fig. 3.5).

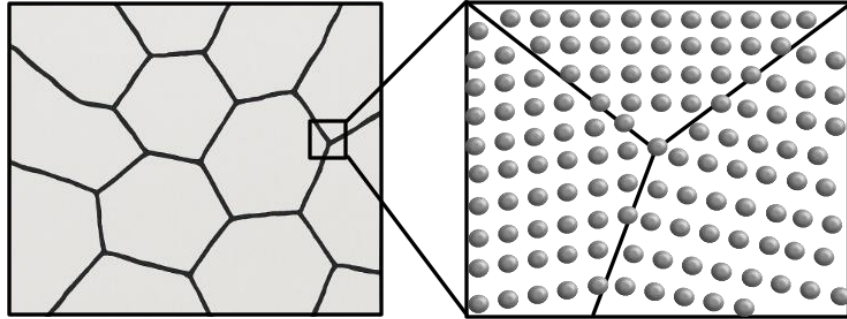


Fig. 3.5: Illustration of grain boundaries on a metal surface (left panel). Right panel, A zoomed-in section of the image, showing the misalignment in crystal orientation between the grain boundaries.

Short-circuit diffusion and lattice diffusion have different diffusion coefficients (D) that typically follow an Arrhenius-type relationship:

$$D = D_0 * \exp\left(-\frac{Q}{RT}\right) \quad (\text{Eq. 7})$$

D_0 is the frequency factor independent of the temperature, Q is the activation energy, R is the gas constant, and T is temperature. A useful approach to describing total diffusion in polycrystalline oxide has been proposed by Hart [96]:

$$D_{eff} = D_L(1 - f) + D_{gb}f \quad (\text{Eq. 8})$$

where D_{eff} represents the effective diffusion coefficient, contributed by both lattice diffusion and grain boundary diffusion. Thus, D_{gb} and D_L are the self-diffusion coefficients for the grain boundaries and the bulk lattice, respectively. The term f is the area fraction of grain boundaries perpendicular to the direction of diffusion, which is expressed as follows:

$$f = \frac{\delta}{d} \quad (\text{Eq. 9})$$

where δ is the width of the oxide grain, and d is the grain size. This approach has been adapted for various oxide systems, to determine the diffusivity of ions through the oxide scale. As understood from Eq. (9), the size of the oxide grain plays an important role in understanding the mobility of ions through an oxide scale. Previous studies on Fe-Cr alloys at high temperatures have shown that the diffusion coefficient, D_{gb} , may be several orders of magnitude greater than D_b [94, 95].

3.5 Breakaway corrosion- primary vs secondary corrosion regime

Typically, oxides are generally described as protective if they achieve the following properties [82]:

- ❖ Strong adherence to the alloy
- ❖ Thermodynamic stability
- ❖ High melting temperature
- ❖ Thermal expansion coefficient similar to the metal

❖ Low frequency of lattice defects

Alloys designed for use in high-temperature applications are described as relying on the formation of oxides that have the abovementioned properties. These are exemplified by corundum-type Me_2O_3 oxides, such as Fe_2O_3 , Cr_2O_3 , $(\text{Fe},\text{Cr})_2\text{O}_3$ and Al_2O_3 [82]. However, in biomass- and waste-fired boilers, the environment is highly dynamic and corrosive. Interactions with the surrounding environment can result in the gradual removal of Cr and Al from the oxide. If the rate of removal of these critical alloy elements is sufficiently high, the protective oxide layer breaks down, leading to the formation of a fast-growing, multilayer oxide that is less-protective, in a phenomenon commonly referred to as ‘breakaway corrosion’. In light of this, recent studies have categorized the protective properties of alloys into two regimes: the primary corrosion regime, where the Cr/Al-rich corundum oxide scale remains intact; and the secondary corrosion regime, i.e., the transition to the multilayer, less-protective oxide scale [97, 98]. For Fe-based alloys such as stainless steels and FeCrAl alloys, the multilayer oxide beyond breakaway corrosion generally consists of an outward-growing, Fe-rich oxide scale and an inward-growing spinel. The structure of the oxide scale is driven by both kinetics and thermodynamics. In the inward-growing spinel structure, Cr^{3+} and Al^{3+} ions are relatively immobile, while $\text{Fe}^{2/3+}$ ions diffuse rapidly towards the oxide/atmosphere environment, leading to the formation of the outward-growing, Fe-rich oxide scale [82]. The phase of the Fe-rich, outward-growing oxide scale will vary depending on the partial pressure of oxygen and the temperature, as described in *Section 3.1*. The chemical composition of the inward-growing spinel depends on the chemical composition of the alloy.

Studies have demonstrated that alloys that are capable of forming protective Cr- and Al-rich corundum-type oxides in a mild environment may transition to the secondary corrosion regime within 24 hours of exposure in a waste-fired boiler environment [99]. Thus, describing the protective properties of alloys solely in terms of the primary corrosion regime may, in some scenarios, be misleading. As a consequence, recent studies have shifted the focus towards understanding the influences of alloying elements in the secondary protective regime, beyond breakaway corrosion, in harsh environments [100, 101]. The findings from these studies are illustrated in Fig. 3.6. Typically, within the secondary protective regime, the oxide may have:

- (I) Poor protective properties characterized by a high corrosion rate.
- (II) Good protective properties, characterized by a lower corrosion rate than in (I).
- (III) Progression from good protective properties to the formation of a healing layer further improving the corrosion resistance.

The corrosion-protective property has shown to depend heavily on the oxide structure of the inward-growing spinel [100, 102]. It has been shown that elements such as chromium (Cr), and aluminum (Al) not only contribute to improve protection during the primary corrosion regime, but also play crucial roles in enhancing corrosion resistance in the secondary corrosion regime [100, 101]. Specifically, it has been shown that these alloy elements can promote the development of a protective Cr/Al-rich spinel (good protection), which over time can form a corundum-type, inward-growing oxide beyond breakaway corrosion, i.e., a ‘healing layer’ that further reduces the corrosion rate [100]. Note that the examples shown in Fig. 3.6 represent a generalized case in which the oxide scale remains dense and well-adherent to the alloy. It does not account for kinetic deviations caused by other factors, such as: (i) the oxide scale delamination commonly observed in aggressive

corrosive environments that leads to a restart of parabolic growth and, thus, an increase in kinetics; or (ii) the formation of surface melts from the reaction of various corrosion products and deposits, which may shift the oxidation kinetics toward an overall linear growth behavior.

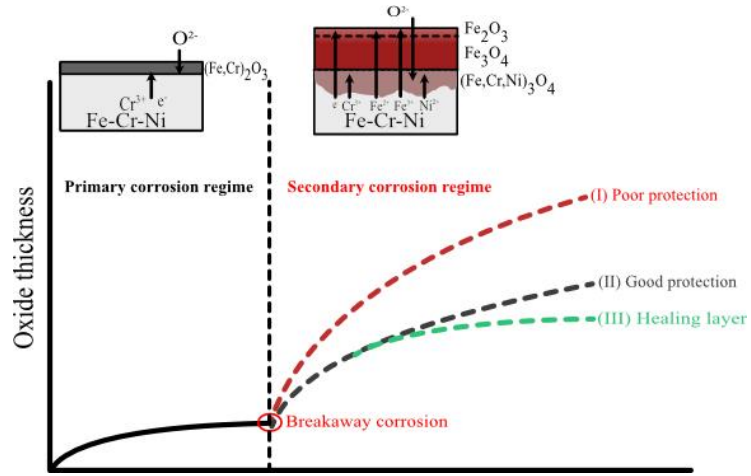


Fig. 3.6: Illustration of the concepts of breakaway corrosion and the primary and secondary corrosion regimes, exemplified by a Fe-Cr-Ni alloy. The protective properties of the oxide scale beyond breakaway corrosion are highly influenced by the alloy elements.

The term breakaway corrosion is not applicable to low-alloyed steels. These types of alloys do not contain sufficient Cr or Al to form primary protective oxide scales, so the transition to the secondary protective regime does not occur. However, when exposed to harsh environments there are increases in the oxide growths of these alloy types. In such cases, the sudden change in kinetics is not due to the depletion of key alloying elements in the oxide scale, but rather to the introduction of corrosive species into the oxide or at the metal/oxide interface. These species can enhance ion diffusion through the scale, accelerating the corrosion process. In addition, delamination of the oxide scale can occur, driving repeated reformation of the oxide layer resulting in increased corrosion [103, 104].

4. Alloys used in this thesis

For water walls and superheater tubes, efficient and cost-effective performance over prolonged periods relies on specific attributes, including adequate resistance to high-temperature corrosion. To ensure this, a set of alloy types can be implemented. Depending on the chemical composition of the alloy, the temperature, and the surrounding environment, the protective properties of the oxide formed will vary. An overview of the alloy types studied in this thesis is provided below.

4.1 Ferritic low-alloyed steels

Ferritic low-alloyed steels are commonly used for water wall and superheater applications due to their low cost and favorable mechanical properties, such as creep strength at temperatures of up to approximately 500 °C [105]. Molybdenum (Mo) is frequently utilized as an alloying element to improve the mechanical properties of the material, while Cr is incorporated to improve the material's resistance to corrosion. Nevertheless, the amount of Cr added is not sufficient to form a Cr-rich, corundum-type oxide; instead, a multilayer Fe-rich oxide scale is formed at temperatures and in environments relevant to biomass- and waste-fired boilers [82].

4.2 Austenitic stainless steels

Austenitic stainless steels are Fe-based alloys that contain at least 10.5 wt.% Cr, which enables the formation of the Cr-rich, corundum-type oxides $[Fe,Cr]_2O_3$ or Cr_2O_3 , which have excellent corrosion resistance in mild environments. The austenitic phase is typically stabilized by the addition of nickel (Ni) [82]. Characteristic properties of austenitic stainless steels are good ductility, weldability, and protection against corrosion. The addition of elements such as Co and Cu improves creep strength through precipitation hardening [105].

4.3 Nickel-based alloys

Nickel-based alloys consist primarily of Ni and sufficient Cr to facilitate the formation of a protective corundum Cr_2O_3 . As with the austenitic stainless steels, these alloys have an austenitic microstructure with excellent weldability and corrosion-protective properties. These make them attractive candidates for coating and overlaying weld applications at high temperatures. Improvement of the mechanical strength is achieved by precipitation hardening or solution hardening through the addition of different alloy elements, such as Ti, Al, Mo, Co and W [105]. The high Ni-content, however, makes this alloy expensive [49].

4.4 FeCrAl alloys

FeCrAl alloys are known for their exceptional corrosion resistance in the temperature range of 900°–1300 °C [106-108]. This is primarily attributed to their ability to form a protective α - Al_2O_3 oxide scale, which is a thermodynamically stable oxide with high stoichiometry that enables slow diffusion of chemical species thorough oxide. However, the superheater tubes in waste-fired boilers operate at much lower material temperatures and the formation of α - Al_2O_3 is very slow, leading to the formation of transient, mixed Al_2O_3 [20, 109]. Furthermore, FeCrAl alloys containing high chromium content leads to phase separation at intermediate temperatures around 500 °C due to the miscibility gap in the Fe–Cr system. This results in the formation of a Fe-rich (α) phase and a Cr-rich (α') phase, a phenomenon known as 475 °C embrittlement or α – α' phase separation [108]. This phase transformation significantly impairs the alloy's mechanical properties, making it unsuitable

for use in applications between 300 °C and 700 °C or higher. To avoid this, a Cr content of 10 wt.% in FeCrAl alloys that contain 4–8 wt.% Al has been reported to suppress the formation of the α' -phase at temperatures relevant for water walls and superheater tubes [108]. The novel FeCrAl alloys (EF100 and EF101) developed by Kanthal AB used in this study have been designed specifically to avoid α - α' phase separation at temperatures as low as 300 °C, which makes them interesting candidates for water wall and superheater applications. Lastly, it is important to note that FeCrAl alloys do not possess the pressure-bearing properties required for use as bulk materials in water wall or superheater applications, so in this work, they are considered for use as overlay materials, for co-extrusion or coating.

5. Corrosion mechanisms in biomass and waste-fired boilers

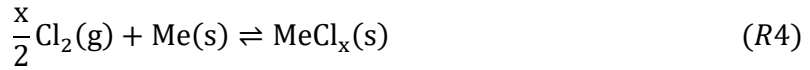
The environment in a biomass- or waste-fired boiler is highly corrosive. While flue gas composition can be chemically complex, research has identified several key corrosion mechanisms that are commonly linked to increased corrosion rates of water wall and superheater tubes. The most-relevant mechanisms for this work are discussed in the following sub-sections.

5.1 Chlorine-induced corrosion

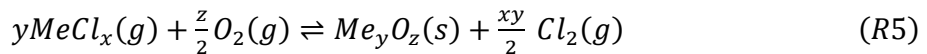
It is widely acknowledged that Cl-containing compounds are highly corrosive at high temperatures [110]. While extensive research has been conducted on the mechanisms involved, the exact processes are still not fully understood. In general, two primary mechanisms have been proposed; the active oxidation mechanism and the electrochemical approach.

5.1.1 Active oxidation

The active oxidation mechanism, also known as the chlorine cycle, was first suggested by McNallan [111] and subsequently refined by Grabke [112]. This mechanism proposes that Cl-induced corrosion is initiated by gaseous $\text{Cl}_2(\text{g})$ diffusing through the oxide scale via micro-cracks and pores and reacting with the metal substrate at the oxide/metal interface, to form metal chlorides (MeCl_x) [112]:



where x depends on the valency of the metal ion. It is suggested that due to the high vapor pressures of metal chlorides at elevated temperatures, continuous evaporation of these species occurs, which allows the rapid diffusion of gaseous metal chlorides outwards towards the oxide/gas interface. As an oxygen concentration gradient develops throughout the oxide scale, the metal chlorides will eventually reach a region that has sufficiently high p_{O_2} to promote the oxidation of metal chlorides, resulting in the formation of a porous, poorly protective oxide and the release of $\text{Cl}_2(\text{g})$. It is argued that the released $\text{Cl}_2(\text{g})$ acts as a corrosion catalyst, re-entering the oxide scale and repeating the reactive steps described above:



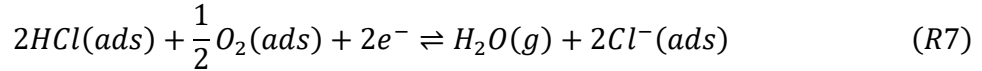
However, certain aspects of the proposed mechanism are subjects of debate. For instance, to establish favorable conditions for metal chloride formation at the metal/oxide interphase, rapid diffusion of $\text{Cl}_2(\text{g})$ and metal chlorides(g) through the oxide is assumed, whereas oxygen molecules simultaneously retain significantly lower mobility. Furthermore, as mentioned before, it has been assumed that diffusion occurs via cracks and pores. Given that the molecular length of O_2 is less than that of Cl_2 , micro-cracks and pores should also promote rapid diffusion of O_2 , thereby promoting an environment that makes metal chlorides thermodynamically unstable. In addition, prior to breakaway corrosion, the oxide scales are usually adherent with low concentration of cracks and voids, which makes it even more difficult to explain the suggested rapid diffusion route for $\text{Cl}_2(\text{g})$ [113].

5.1.2 The electrochemical approach

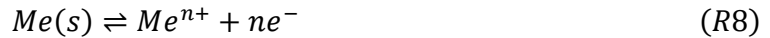
Folkeson et al. have proposed an electrochemical approach to elucidate the diffusion of chlorine through the oxide scale [114]. In the proposed mechanism, molecular chlorine dissociates at the scale-gas interface to form chloride ions:



During the combustion of biomass and waste where HCl is present, chloride ions are suggested to be generated via the deprotonation of HCl:



Subsequently, metal oxidation takes place at the oxide/metal interface, thereby supplying the Cl molecule with the necessary electronic current:



Given the relatively low charge and large size of the monovalent Cl^- , it has been suggested unlikely that the Cl^- will exchange positions with the oxygen ions in the oxide crystal lattice. Instead, it is proposed that the anionic species is transported through grain boundary diffusion [114]. In addition, surface-located Cl^- are expected to have higher mobilities than the divalent O^{2-} , due to the aforementioned properties. Metal chlorides are expected to form throughout the oxide surface rather than exclusively at the metal-oxide interface. It has been suggested that the locations of the metal chlorides in the oxide scale depend on the inward and outward diffusions rate of Cl^- and metal ions, respectively [114].

5.1.3 Delamination of oxide scales in presence of Cl

The presence of Cl has been suggested to promote delamination of oxide scales [103]. This results in the creation of a localized pathway for the corrosive atmosphere to reach the metal-oxide interface, leading to the exposure of a new reactive surface and the subsequent re-initiation of oxide growth. A study carried out by Jonsson et al. showed that a low-alloyed steel in the presence of KCl(s) displayed significant delamination at 400 °C [115]. Persdotter et al. have shown that with TGA, i.e., continuous monitoring of the mass gain during the exposure, delamination of the oxide scale on a low-alloyed steel in the presence of KCl(s) most likely occurs during the exposure, as indicated by the sudden kinetic increase in mass gain (see Fig. 5.1) [103]. Furthermore, when analyzing the oxide microstructure, two oxide scale layers with similar morphologies were detected. The dense oxide structure, together with the parabolic growth, indicates that ion diffusion through the oxide scale is the rate-determining step of oxidation.

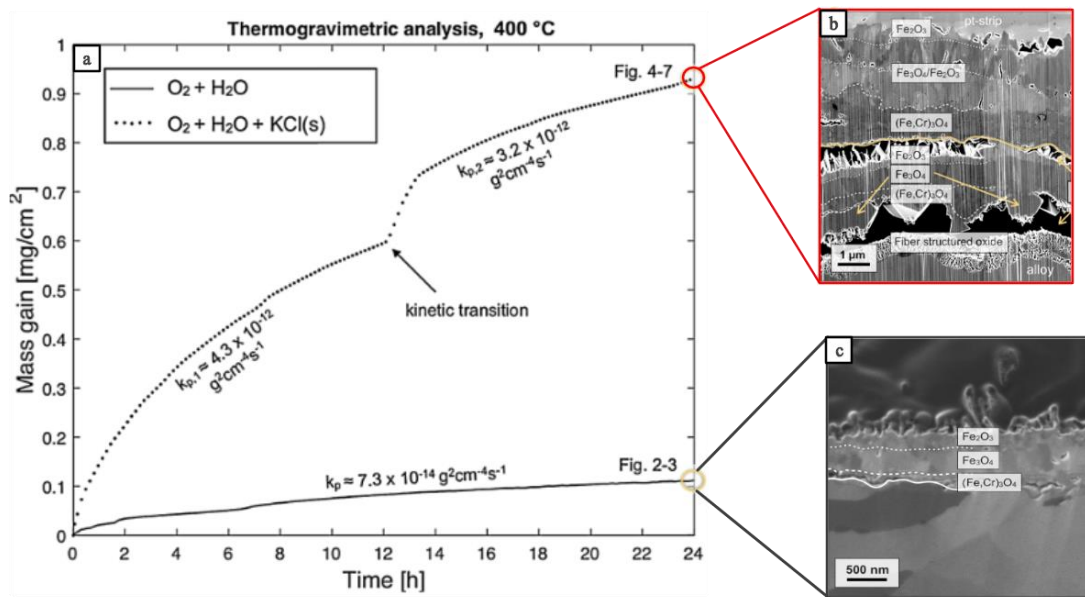


Fig. 5.1: (a) Thermogravimetric analysis (TGA) of a low-alloyed steel (T22) that was exposed to O₂ + H₂O and O₂ + H₂O + KCl(s) at 400 °C for 24 hours. Both conditions show parabolic oxidation behavior, although the presence of KCl(s) leads to a sudden increase in oxidation rate after approximately half the exposure time; (b) Microstructural analysis reveals oxide scale delamination in presence of KCl(s), followed by the formation of a secondary oxide layer. The overall growth of both layers remains parabolic; (c) In the absence of KCl(s), the oxide scale remains adherent and much thinner. Images reproduced and modified from [103], and distributed under the Creative Commons Attribution (CC BY) license.

The reason for the delamination associated with Cl is not yet fully understood. It has been suggested that metal chlorides (such as FeCl₂) that are present at the metal/oxide interphase significantly reduce the adhesion of the oxide scale [115]. An alternative suggestion is that the accelerated corrosion rate leads to growth stresses which may lead to cracks and delamination [116].

5.2 Molten-phase corrosion

The formation of molten species may significantly accelerate the corrosion, in what is described as ‘molten-phase corrosion’. Molten salts act as electrolytes that facilitate rapid transport of ions through the oxide scale. Moreover, studies have shown that melt-induced corrosion can promote the dissolution and disruption of the protective oxide scales [18]. In biomass- and waste-fired boilers, molten-phase corrosion has been linked to eutectic melt formations or partial melt formations with various salts and corrosion products [18]. Eutectics are a homogeneous mixture of two or more components that have lower melting points than the respective pure substances at a particular mix ratio of the components. Table 5.1 lists the melting points of the compounds that are relevant for this thesis and describes the eutectics that have been suggested to accelerate corrosion of important water walls and superheater tubes [28].

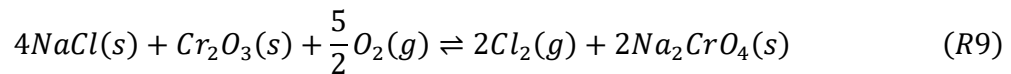
Table 5.1: Melting temperature of relevant compounds and mixed compounds observed in deposits during combustion both biomass and waste. Adapted from [117].

Reference	Compounds	Melting point and lowest eutectic melting temperature [°C]
[118]	Pb	327
[26]	PbCl ₂	501
[118]	PbO	886
[119]	KCl	771

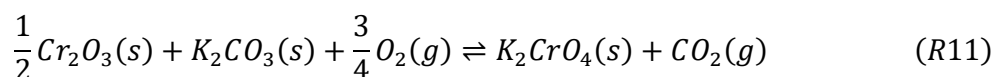
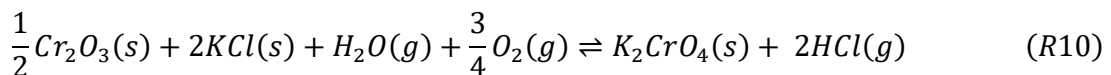
[119]	NaCl	801
[120]	FeCl ₂	677
[121]	KCl-PbCl ₂	409
[121]	NaCl-PbCl ₂	409
[49]	KCl-NaCl	657
[122]	PbCl ₂ -FeCl ₂	420
[49]	KCl-FeCl ₂	350
[49]	NaCl-FeCl ₂	300

5.3 Chromate formation

Accelerated corrosion of Cr₂O₃ or (Fe,Cr)₂O₃ has been attributed to chromium depletion from the oxide as a result of its interaction with alkali and heavy metal chlorides [123]. Experimental studies carried out by Grabke et al. on stainless steel samples exposed to NaCl at 600 °C and 700 °C in an oxidizing environment suggest that NaCl reacts with the protective chromia scale to form sodium chromate and chlorine [112]:



The released Cl₂(g) is suggested to participate in the propagating corrosion step via the active oxidation mechanism described in the previous section, forming a porous oxide that consists mainly of Fe₂O₃. Grabke et al. concluded that chromate formation only acts as a source for the Cl₂ formation that is needed for the chlorine cycle to be activated, which is designated as the main corrosion mechanism [18]. Nevertheless, Pettersson et al. [124] have studied the role of alkali in high-temperature corrosion by exposing stainless steel to a set of alkali compounds, including both Cl-containing (KCl) and chlorine-free (K₂CO₃) salts, in a humid environment at 500 °C or 600 °C. Based on their observations, it appears that breakaway corrosion is initiated by the breakdown of the protective Cr-rich oxide scale, which is triggered by the formation of potassium chromate:



The results of the study demonstrate that K₂CO₃ exhibits corrosion behavior comparable to KCl, forming a similar oxide morphology. This suggests that the initial corrosion process is primarily driven by chromate formation rather than being solely influenced by chlorine.

5.4 Corrosion-erosion

Fluidized bed boilers provide fuel flexibility and improved combustion efficiency. However, the fluidized bed material can lead to significant erosion of the water walls and superheater tubes. This issue may be especially critical for modern CFB boilers, wherein superheater tubes are placed in the loop seal. The loop seal is the section of the boiler where recirculated solid particles are directed before it is returned to the combustion chamber. It is equipped with its own fluidizing air system to prevent particle accumulation. Thus, the bed particles may experience relatively high velocities, such that upon impact with the superheater tubes can result in increased degradation rates. Although this part of the region should in theory provide an environment with low concentrations of corrosive

species, as the flue gas is separated from the bed particles in the cyclone prior to entering the loop seal, studies have reported clear signs of corrosion on superheaters in this region, and this has been associated with aggressive corrosive species such as Cl, which suggests that the presumably mild environment might be harsher than initially argued [30] [125] [126]. One possible reason for this has been suggested by [30], whereby an increasingly corrosive environment is attributed to the transportation of corrosive flue gas to the loop seal region and metal surface via condensation onto the fluidized bed material. As such, both erosion and corrosion are likely to impact the degradation rate of the material.

Corrosion in high-temperature erosive environments can be categorized into three distinct types (see Fig. 5.2):

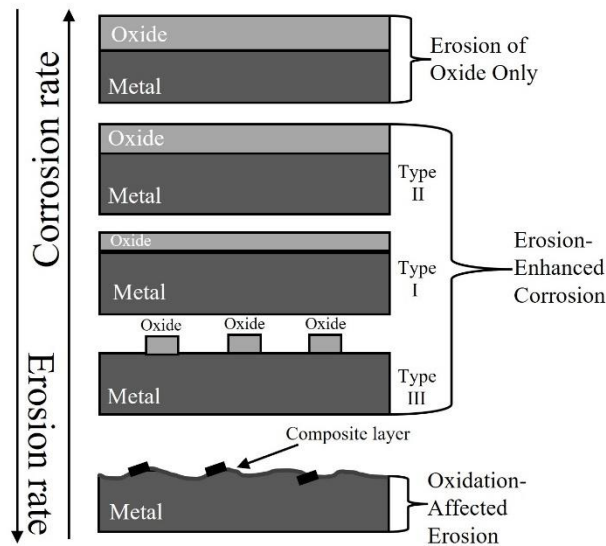


Fig. 5.2: Corrosion-Erosion regimes. Adapted from [127].

5.4.1 Erosion of oxide

The effect of erosion is negligible and mainly confined to weak erosion of the oxide layer [127].

5.4.2 Erosion-enhanced corrosion

Erosion-enhanced corrosion is divided into three subgroups, denoted as Types I, II and III (Fig. 2.9.2). Type I typically represents a scenario in which erosion leads to oxide scale thinning and the corrosion rate is increased as the diffusion path length through the oxide scale is reduced. In Type II, the oxide thickness is typically larger than that seen in cases of pure corrosion. This has been attributed to erosion-induced cracks and defects in the oxide layer, which act as short-circuit diffusion pathways, allowing corrosive species to reach more easily the underlying metal surface. This leads to less-protective properties of the oxide scale and accelerated corrosion [128]. Type III represents a scenario in which significant erosion leads to spallation of the oxide, exposing local areas of the underlying metal to the environment and significantly accelerating the corrosion rate. [127].

5.4.3 Oxidation-affected erosion

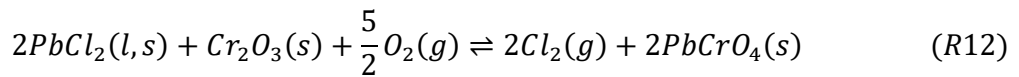
In oxidation-affected erosion, the intensity of erosion is so high that an oxide layer cannot be sustained. Instead, a composite layer is formed on top of the metal, comprising oxidation fragments,

deformed metal, and erosion particles. The properties of the composite layer determine whether or not accelerated degradation of the material occurs [127, 128].

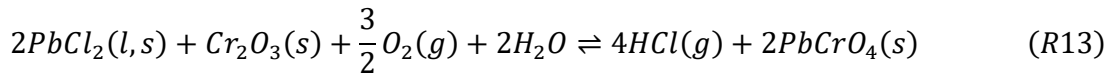
5.5 PbCl₂-induced corrosion

As this thesis deals specifically with PbCl₂-induced corrosion, a brief background of this topic will be provided in this section.

During the combustion of waste-derived fuels that contain Pb, the Pb may react with chlorine, forming PbCl₂, which has been shown to cause corrosion of heat exchanger materials [129]. In particular, water walls are frequently described as having deposits that are enriched for Pb. Depending on the composition of the deposit and the type of material being exposed, different mechanisms for PbCl₂-induced corrosion have been proposed. For chromia-forming alloys, such as stainless steels and Ni-based alloys, studies have suggested that PbCl₂-induced corrosion is triggered by lead-chromate formation, which destroys the primary protective oxide scale according to the following reaction in an oxidizing environment [26, 28]:



It is argued that the released Cl₂(g) further increases the corrosion rate through the formation of metal chlorides according to the active oxidation mechanism. In the presence of water vapor, Nunez et al. [28] have proposed that the following reaction occurs [28]:



It has also been suggested that when PbCl₂ combines with other relevant salts that are commonly present in the deposits on the water wall tubes of waste-fired boilers, the reactions between these salts and metal chlorides produce low-melting compounds, thereby further accelerating corrosion through melt-induced mechanisms [28].

In comparison to chromia-forming alloys, the roles of Pb and Cl in PbCl₂-induced corrosion of low-grade steels, such as low-alloyed steel and carbon steel, are less well understood. These steels are common materials for water wall applications in waste-fired boilers, primary due to their good mechanical properties and low price. For this alloy type, breakaway corrosion by chromate formation is not possible, as these alloys contain insufficient Cr to form a stable, protective Cr-rich oxide scale in oxidizing environments. Consequently, other corrosion mechanisms must dominate the corrosion behavior. Studies have indicated that the presence of a partially molten PbCl₂ salt-mixtures can enhance the corrosion rate of low-alloyed steels [130]. However, other investigations have demonstrated that the formation of molten PbCl₂ or eutectic mixtures containing PbCl₂ is not a necessary condition for accelerated corrosion to occur on low-alloyed steels. A previous study carried out by Bankiewicz et al. [131] on the corrosivity of Pb-containing salt mixtures for a low-alloyed steel (10CrMo910) revealed the extreme activity of pure PbCl₂. In that study, the low-alloyed steel was exposed to different PbCl₂ salt mixtures at 400 °C, 500 °C and 600 °C for 168 hours in air. At 400 °C, severe corrosion was observed for PbCl₂, without any indication of any melt being present. Furthermore, there were no significant differences in the corrosion rates of samples exposed to pure PbCl₂ or a mixture of PbCl₂-KCl, suggesting the high reactivity of PbCl₂. It has been proposed that PbCl₂ disrupts the presumed primary protective Cr₂O₃ layer by forming PbCrO₄, releasing Cl₂(g) in the process, which could further accelerate corrosion through the active

oxidation mechanism [131]. However, this conclusion is debatable, as the steel contains only 2.2 wt.% Cr, calling into question the likelihood of Cr_2O_3 formation under these conditions. Further investigations by Larsson et al. demonstrated that low-alloy steel exhibited significant corrosion in the presence of PbCl_2 at 400 °C in a humid environment, with localized corrosion attacks occurring near the regions where PbCl_2 particles were deposited [104].

Lastly, previous studies of PbCl_2 -induced corrosion have mostly been conducted for a fixed exposure time [26, 104, 131, 132]. In many cases, severe corrosion has already occurred by the time of the analysis [22], [27], [29]. This approach makes it challenging to distinguish between the initiation and propagation stages of the corrosion process. Since the initial corrosion process can significantly influence corrosion behaviors in later stages, gaining a deeper understanding of these early mechanisms is crucial for advancing knowledge of PbCl_2 -induced corrosion. Moreover, previous studies have attributed the corrosion mechanisms primarily to Cl-induced reactions and the formation of metal chlorides, either through melt formation or the rapid release of Cl from the reaction of PbCl_2 with the surrounding environment. While Pb in PbCl_2 has been shown to play a critical role in destroying the protective chromia layer on stainless steel and Ni-based steels, its impact on low-alloyed steel remains largely unexplored. A better understanding of the role of Pb is important for developing corrosion prevention strategies and addressing the rapid degradation observed in the water wall tubes of waste-fired boilers.

6. Analytical techniques

To address the corrosion challenges in biomass and waste-fired boilers, a deep understanding of the underlying corrosion mechanisms is required. These mechanisms are best studied by implementing analytical techniques and adequate sample preparation methods. In this work, scanning electron microscopy (SEM), broad ion beam (BIB) milling, x-ray diffraction (XRD) and kinetic modelling were employed to identify corrosion products and to assess corrosion rates and mechanisms.

6.1 Scanning electron microscopy

Scanning electron microscopy (SEM) is a non-destructive analytical tool used to characterize the microstructural features of the corrosion products and the metal substrate. The spatial resolution of an SEM is typically at the nanometer level. This allows detailed surface analysis of the specimen that would otherwise be inaccessible by optical microscopy. In addition, when coupled with an Energy-dispersive x-ray spectroscopy (EDX) detector, both qualitative and quantitative elemental analyses of the specimen can be performed for a defined region. This is of great importance and may provide valuable information on, for example, how chemical elements in the surrounding environment interact with the metal substrate/oxide scale and their effects on the corrosion rate. This can also provide us with information on whether breakaway corrosion has transpired by analyzing the chemical composition of the oxide scale [133].

The high spatial resolution and chemical element analysis offered by SEM and EDX relies on the interactions between electrons that are emitted from the SEM instrument (referred as incident electrons) and the atoms in the sample studied. Electron microscopy produces a focused accelerated electron beam that interacts with the electrons from the specimen, thereby generating signals that are converted to a high-resolution image. The signals detected from the beam-specimen interaction include secondary electrons (SE), backscattered electrons (BSE), and characteristic x-rays, among others. In this study, the SE, BSE and EDX signals have been studied, as they offer valuable insights into the sample's topography, microstructure, and chemical composition. The depth of interaction of the specimen depends strongly on the type of signal generated, the studied material, the accelerating voltage, and the incident angle of the generated electron beam [133].

Secondary electrons are low-intensity electrons (<50 eV) that are generated from inelastic interactions between the sample studied and the incident electrons (Fig. 6.1a). These interactions occur when the incident electrons contain sufficient energy to eject electrons from the outer atomic shells. Their relatively low energy limits the escape depth. Consequently, the majority of the SE that escape to the surface of the material and reach the detector originate from areas close to the specimen surface, which means that they carry useful information regarding the topography and complex surface features of the sample studied [133]. Secondary electrons can also be utilized for imaging grain contrast; however, compared to backscattered electrons, grain contrast obtained with SE is more sensitive to the choice and configuration of the detector [134].

Back-scattered electrons are generated by elastic scattering that occurs between the incident electrons and an atomic nucleus of the sample. Upon elastic interaction, the trajectory of the incident electrons changes, and the electron only loses minimal kinetic energy (Fig. 6.1b). This allows the electrons to attain a much higher escape volume than that seen for the SE. However, this also leads to reduced spatial resolution of the image, as compared with SE. The probability that

elastic scattering will occur is proportional to the atomic number, Z , and the density of the region of interest. That is, regions that possess increased concentrations of elements with high atomic numbers discharge more backscatter signals. Thus, heavy elements or dense regions of the sample will produce numerous BSE that reach the detector, resulting in a bright appearance in BSE images. Conversely, low-density areas or light elements will manifest as darker regions [133].

EDX signals are generated if sufficient energy is transferred between the incident electrons and the sample atom, such that the ejection of electrons from the inner electron shells of the atom occurs, leaving the atom in an excited state. As a direct consequence, the atom relaxes to its ground state by allowing electrons at higher energy levels to fill the vacant position (Fig. 6.1c). During this event, excess energy is emitted as x-ray photons with a defined energy that is characteristic for each element. By coupling an EDX detector to the SEM instrument, an EDX spectrum can be generated, and it is possible to identify the chemical composition and quantify the chemical elements of individual points or to map out the distribution of elements in the studied area. Compared to SE and BSE, the interaction volume is larger for x-rays, which limits the possibility to quantify precisely the chemical elements in small volumes of interest [133]. This limitation can be overcome by tilting your sample or lowering the accelerated voltage of the incident electron beam. In the latter case it is crucial to ensure that the beam energy remains above the threshold required to excite inner-shell electrons of the element of interest. If the accelerated voltage is set too low, the high energy characteristic x-rays may not be generated, leading to inaccurate quantification and reduced x-ray counts, which in turn worsens the peak-to-background ratio. However, in some cases, qualitative analysis may be more important than quantitative analysis. An example of this is when the presence of a specific element within a thin oxide scale is to be determined. In these situations, the accelerating voltage can be reduced to enhance spatial resolution and minimize interference from adjacent regions, as long as it remains sufficient to generate low-energy characteristic x-rays needed to detect the element of interest.

Some elements emit x-ray photons within similar energy ranges, which can result in peak overlap in EDX spectra and subsequently compromise the accuracy of both qualitative and quantitative analyses. For example, relevant to this study, the Mo L α peak and the Pb M α peak occur at 2.341 keV and 2.299 keV, respectively, making them difficult to resolve. To minimize analytical errors in such cases, it is crucial to adjust the accelerating voltage to excite higher-energy characteristic x-rays that are well separated between the two elements.

An important aspect to consider when performing EDX analysis is to ensure the accuracy of the elemental analysis. This is typically achieved by first conducting EDX analysis on a reference substrate with a known chemical composition. In this work, this has been done by carrying out EDX analysis on the alloy of interest, far away from the corrosion front. The resulting chemical composition has then been compared with a certified chemical composition provided by the different material suppliers. In cases where certified data were unavailable, the results were compared to compositions reported in the literature.

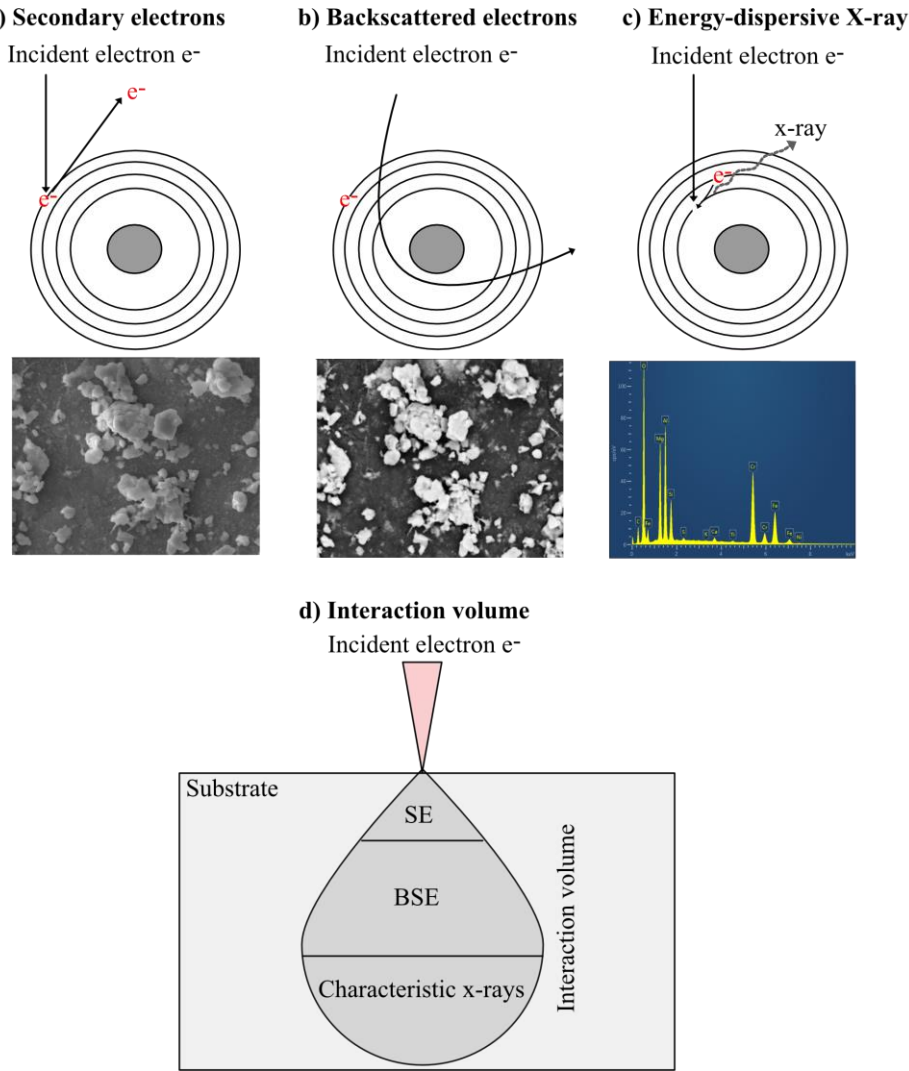


Fig. 6.1: Illustration of the different signals produced in the scanning electron microscope (SEM): a) Secondary electrons (SE); b) Backscattered electrons (BSE); c) Energy-dispersive x-ray (EDX); d) the interaction volume of the different signals.

In this work the surface and cross-sectional microstructural analysis were performed by an FEI Quanta ESEM 200, equipped with a detector for energy dispersive X-ray spectroscopy (EDX). The imaging was performed at an accelerated voltage range of 15-20 kV, while the EDX analysis was carried out at 10-20 kV.

6.2 Broad ion beam milling

Observing features at high magnification with SEM requires a careful sample preparation method. In some cases, conventional mechanical polishing may not be sufficient, so other means must be considered. Broad ion beam (BIB) milling is an effective surface preparation method that achieves surface finishes that are superior to those obtained using traditional polishing methods. The working principle of BIB milling is depicted in Fig. 6.2. The sample is placed in a vacuum chamber. An inert gas, commonly argon (Ar), is ionized in the Ar-gun component of the BIB instrument and accelerated towards the sample, producing an ion beam that interacts with the sample surface. Upon impact, the kinetic energy of the ions breaks atomic bonds and ejects material from the specimen's surface, allowing a controlled and gradual removal of the top surface of the sample. This not only allows the formation of a very fine surface, but also facilitates the removal of any artifacts that

might be introduced during the mechanical polishing steps required prior to BIB. The BIB instrumentation typically enables two distinct milling approaches: (a) cross-section milling; and (b) flat milling.

In cross-section milling (see Fig. 6.2a), a protective mask is applied in front of the sample. The region of interest is then raised above the mask, usually at a height of 10–100 micrometers depending on how much material is to be milled away. The surface above the mask is then selectively removed by milling at an almost parallel angle between the beam and the sample surface. Cross-section milling allows relatively deep milling and is generally used for samples that are difficult to polish mechanically.

In flat milling mode (see Fig. 6.2b), the incident angle of the argon ion beam can be altered over the range of 0°–90°. This allows stringent control of the surface roughness of the specimen. For instance, at angles close to 80°–85°, the beam is almost parallel to the sample, which allows the formation of a surface that has a high level of smoothness, which is important for detecting small features such as oxide grains. Compared with the cross-section milling mode, flat milling allows a wide area to be milled and more-complex geometries and dimensions to be milled.

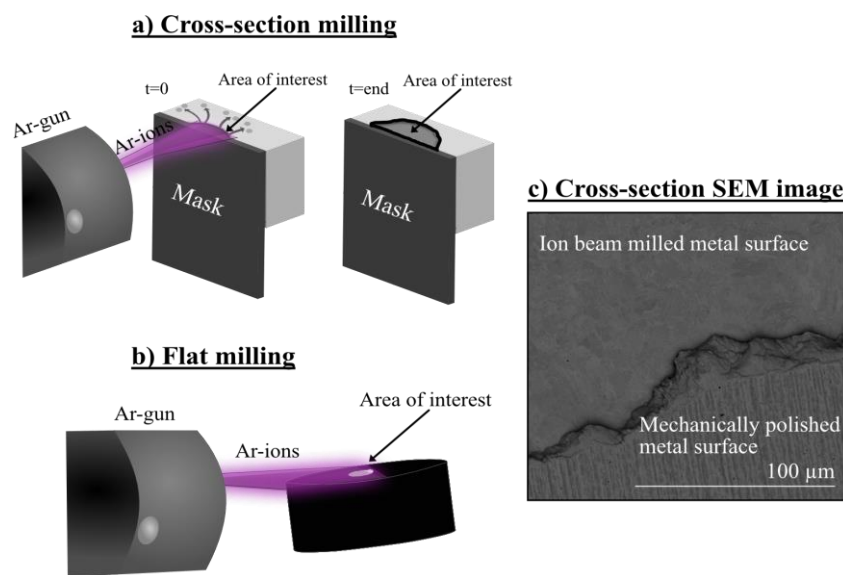


Fig. 6.2: Working principle of broad ion beam (BIB) milling: a) Cross-section milling; b) Flat milling; c) Comparison of the cross-sectional surfaces of an alloy prepared by cross-section BIB milling versus mechanical polishing. In the latter case, small features such as alloy grains are clearly visible.

In this work, the Leica TIX 3x BIB instrument equipped with three argon guns was used for cross-section milling. The samples were BIB milled for 6 h at 8 kV and 3 mA. Prior to BIB-milling the samples were polished down to 4000 grit paper.

The HITACHI ArBlade 5000 instrument equipped with one argon gun was used for flat milling. A two-step milling process was selected using 5 kV during 15 minutes in the first step and 1.5 kV during 30 minutes in the second step. The discharge voltage remained fixed at 1 kV. The Ar-ion beam was set to 85° with respect to the sample surface, i.e., 5° from being parallel to the sample surface. The sample was continuously rotated 60° relative to the fixed Ar-ion beam direction on both milling steps.

6.3 X-ray diffraction

X-ray diffraction (XRD) is a non-destructive analytical tool that is used in this work to characterize the crystalline phases of various corrosion products. The principle of XRD originates from the interaction of an x-ray source with a crystalline sample (see Fig. 6.3). A and B describe two crystallographic planes of a crystalline specimen, subjected to two parallel x-rays of a fixed wavelength (wave 1 and 2). When the x-ray beam encounters the regular arrangement of atoms in the crystal, constructive interference may occur at well-defined angles, reinforcing each other. These conditions are given when the Bragg's equation is fulfilled:

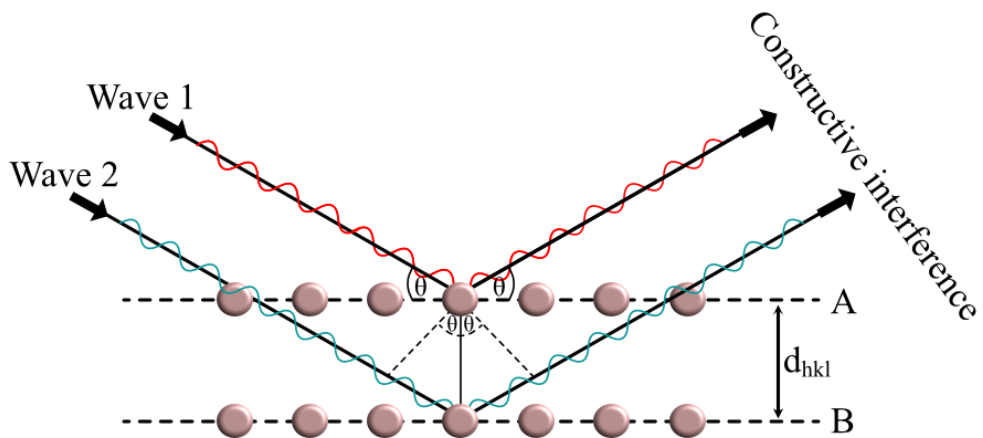


Fig. 6.3: Illustration of constructive interference of x-ray beams, where the incident beam is reflected by atoms arranged within a specific crystallographic plane

$$n\lambda = 2d_{hkl} \sin\theta \quad (\text{Eq. 10})$$

where n is an integer number, λ is the wavelength of the x-ray, d_{hkl} is the interplanar spacing of the lattice planes, and θ is the angle at which the x-ray source diffracts from the crystal plane. The x-rays undergo constructive diffraction when the path between waves 1 and 2 is equal to an integer multiple of the wavelength. The interaction of the x-ray with the substrate produces a characteristic XRD pattern, known as a diffractogram, which can be compared with an existing database to extract information on the crystalline phases, qualitative phase analysis, and determine space groups [135].

In this work, the traditional Bragg-Brentano set-up was used. In this setup, the source and detector move in opposite directions symmetrically and at the same rate (Fig. 6.4). As the angle of the detector and source increases relative to the sample, the x-ray penetration depth increases, thereby allowing the identification of crystalline phases throughout a relatively thick specimen. In this work, the Siemens Bruker 8 Discovery diffractometer equipped with a Cu source and with a measuring range of $10^\circ < 2\theta < 90^\circ$ was employed to analyze the corrosion products.

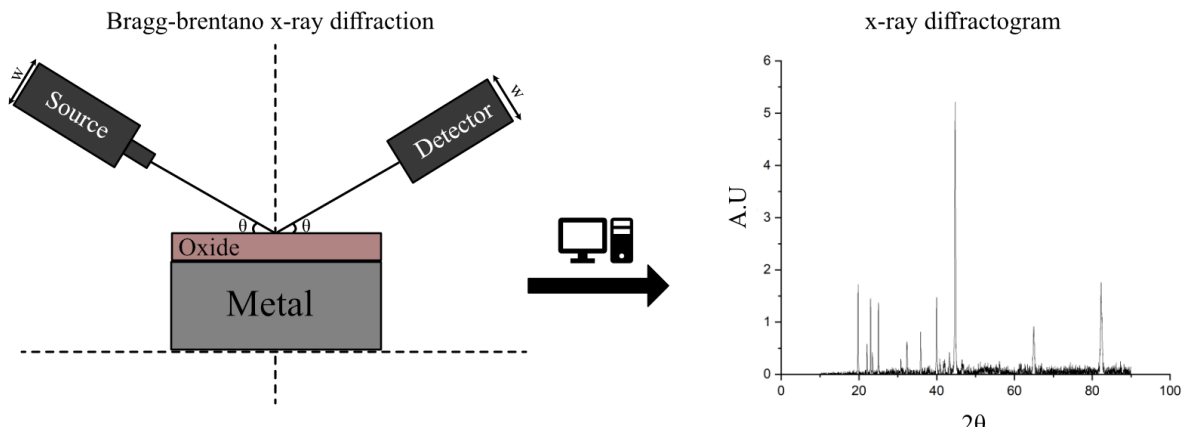


Fig. 6.4: XRD with Bragg-Brentano x-ray diffraction (left panel). Right panel, Diffractogram where the y-axis represents an arbitrary unit (A.U), and the x-axis is 2θ angle.

6.4 Average grain size measurement

In this work, the average oxide and alloy grain sizes were evaluated using SEM in BSE mode on BIB-milled cross-sections. Measurements were conducted using the Average Grain Intercept (AGI) method, in accordance with ASTM E112-12 standard [136]. In this method, several lines are drawn over a region of interest, and the number of intersections between the lines and the grain boundaries is noted. The average grain size is then determined by calculating the ratio of the interceptions to line length using the following equation:

$$\text{Average gain size} = \frac{\sum \text{line length}_i}{\sum X_i - 1} \quad (\text{Eq. 11})$$

Where X represents the number of intersections.

6.5 Electron backscatter diffraction

Electron backscatter diffraction (EBSD) is a characterization method integrated with scanning electron microscopy (SEM), which enables the analysis of crystallographic properties of materials. In comparison to XRD, EBSD offers phase identification locally. In this study, EBSD was employed to determine the crystalline phases present in both the oxide scales and the underlying bulk material. The technique operates by directing an electron beam onto a specimen tilted at approximately 70° , facilitating diffraction from various crystallographic planes within the sample. This interaction generates backscattered electrons with orientation-dependent intensities, which are recorded as grey-scale images using a charge coupled device (CCD) camera. The resulting diffraction patterns are displayed as Kikuchi bands on a phosphor screen, providing spatially resolved crystallographic information through electron channeling contrast. The geometry of Kikuchi bands observed in EBSD patterns directly reflects the spatial orientation of atomic planes within a crystalline structure [137]. This geometric configuration enables the extraction of detailed crystallographic data, such as phase identification and grain orientation, from the material under investigation. In this work phase identification using EBSD was carried out on a TESCAN GAIA3 dual-beam instrument operated at 20kV.

6.6 Kinetic modelling of oxide growth using the DICTRA approach

Modelling oxide growth is an important tool for extrapolating lifetime based on experimental data for longer times which would be impractical to achieve through conventional testing. Data required to develop appropriate models can be extracted from experiments with well-defined conditions that can be used as data sets and important boundary conditions for the developed model. Parabolic kinetics expressed as oxide growth, material loss, or mass gain during high-temperature corrosion are typically observed when the oxide scale remains dense and adherent to the metal substrate. As mentioned in *Section 3.4*, in these scenarios grain boundary diffusion plays a critical role in the oxidation rate at temperatures relevant to superheater and water wall application. Therefore, accurate modeling oxide growth under such conditions requires accounting for both bulk and grain boundary diffusion. Furthermore, to build up an accurate model for describing processes of high-temperature oxidation necessary thermodynamic data for calculation of interdiffusion coefficients and phase equilibria together are necessary.

This challenge has been addressed by the commercial software package DICTRA (**D**iffusion **C**ontrolled **p**hase **T**RAnsformation). The DICTRA approach combines thermodynamic equilibrium calculations, which determine stable phases by minimizing the system's Gibbs energy, with time-dependent modeling of phase evolution under the assumption of local equilibrium. This enables simulation of oxidation processes by accounting for both the kinetics and thermodynamics of the system [85].

In DICTRA, the mobility of species through both bulk (M_{bulk}) and grain boundaries (M_{gb}) can be expressed as following:

$$M_{bulk} = M_0^{bulk} * \exp\left(\frac{-Q}{RT}\right) \quad (Eq. 12)$$

$$M_{gb} = M_0^{bulk} * \exp\left(\frac{-\alpha Q}{RT}\right) \quad (Eq. 13)$$

Where M_0^{bulk} represents the frequency factor for mobility in the bulk, Q represents the activation energy for diffusion in the bulk, R is the universal gas constant and T is temperature. The α -factor represents the reduction in the activation energy for diffusion along grain boundaries compared to bulk diffusion. This coefficient should have a value < 1 and can differ based on the oxide [86]. the total mobility of species is expressed as follows:

$$M_{total} = f_{gb} * M_{gb} + (1 - f_{gb}) * M_{bulk} \quad (Eq. 14)$$

The area fraction of grain boundaries is expressed as the width of oxide grain boundaries (δ) divided by the oxide grain size (d):

$$f_{gb} = \frac{\delta}{d} \quad (Eq. 15)$$

Numerous efforts have been undertaken to simulate oxide scale growth using DICTRA in systems relevant to high-temperature corrosion. Larsson et al. investigated the oxidation of pure iron in dry oxygen at 600 °C for durations of up to 24 hours [138]. In their study, they successfully modeled the growth of hematite, magnetite, and wüstite. To validate the simulation results, they compared predictions, based on kinetic and thermodynamic databases, with independent experimental data.

The simulation results show good agreement with experimental observations, though longer exposure times are required to further substantiate the model's predictive capabilities.

Bigdeli et al. investigated the oxidation of Cr_2O_3 and Al_2O_3 on Fe-based alloys at 600 and 900 °C, respectively [86]. In their study, the DICTRA approach was applied using a combination of the phase boundary model and the moving phase boundary model [86, 139]. The α -value was employed as a fitting parameter for reproducing experimental data obtained from the literature, where the variation in α -value represents the effect of alloying elements on oxide growth kinetics. They showed that in different classes of materials, i.e. chromia and alumina formers, the oxide growth can be predicted using DICTRA simulation for the simple systems of Cr-O and Al-O respectively in different temperature regimes. They used this model to show that a systematic trend can be observed for variation of Cr and Al for α in different steels.

In the examples provided above, kinetic simulations have been carried out over a short period of time < 24 hours. Improving the predictive accuracy of such simulations for longer exposure times necessitates reliable input data, including oxide grain size, which is currently underrepresented in the literature. Specifically, for specimens exposed in full-scale biomass- and waste-fired boiler environments, there is a notable absence of published studies characterizing the oxide microstructure in terms of grain size. One reason for the lack of studies on oxide grains is the difficulty with obtaining high-quality cross-sections that are suitable for oxide grain size analysis. Studies that do investigate oxide grain size often rely on transmission electron microscopy (TEM), which require advanced operational skills and extensive sample preparation. In addition, TEM examines only a very small area, resulting in limited statistical reliability.

In this work, Thermo-Calc software (version 2024a) was used to calculate the equilibrium phase formation, utilizing the TCOX12 oxide database. Furthermore, Simulations in DICTRA were carried out with the moving phase boundary model which enables the simulation of diffusion-controlled growth under the assumption that local equilibrium is maintained at the phase interfaces. All simulations presented in this thesis were carried out by Dr. Torbjörn Jonsson (Chalmers University of Technology) with the assistance from Dr. Henrik Larsson (KTH Royal Institute of Technology) and Dr. Lars Höglund (KTH Royal Institute of Technology).

7. Part I:

Investigation of corrosion mechanisms in biomass and waste-fired boiler environments

The aim of **Part I** of this thesis is to advance the understanding of corrosion phenomena in biomass- and waste-fired boilers. Improved knowledge in this area is essential for mitigating material degradation and minimizing the risk of operational shutdowns, thereby enhancing the reliability and efficiency of the power plant. This objective has been addressed through a combination of field studies in an operational waste-fired boiler, controlled laboratory experiments, and the development of a novel approach for modeling material loss of superheater tubes. Fig. 7.1 provides an overview of the experimental approach adopted in the research carried out in this part of this thesis.

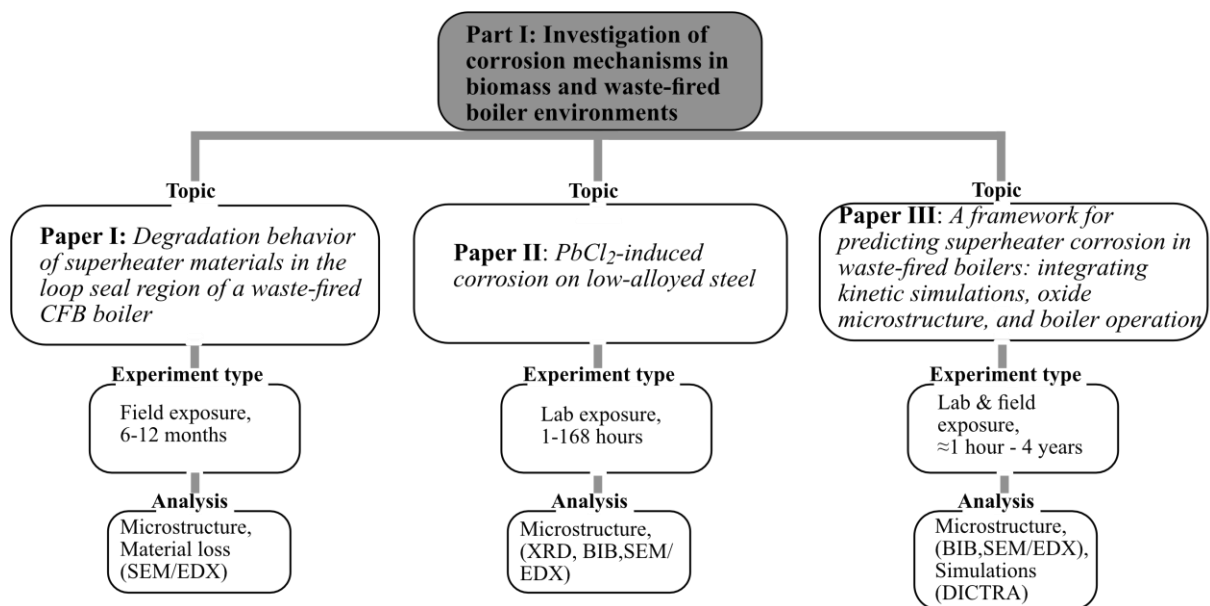


Fig. 7.1: Flowchart illustrating the approach used for the three studies conducted in Part I of this thesis.

- ❖ In **Paper I**, exposures were carried out in a large-scale waste-fired CFB boiler to study the degradation rate and mechanisms for superheater material positioned in the loop seal region. Specifically, the aim was to improve our understanding of the interplay between erosion and corrosion and how this affects material degradation in this environment. The motivations for this study were the limited existing literature covering material performance in the loop seal, and the desire to simplify the process of selecting materials for this particular application. In addition, two novel FeCrAl alloys were investigated and benchmarked with conventional superheater tube materials, to assess their performances.
- ❖ In **Paper II**, PbCl₂-induced corrosion of low-alloyed steel was studied in a controlled laboratory environment. While the existing literature has addressed PbCl₂-induced corrosion in similar environments and with similar materials, there remains a gap in the knowledge regarding the initial and propagating mechanisms for corrosion [104]. Given that the initial corrosion process strongly impacts the corrosion behaviors in subsequent stages, acquiring detailed knowledge of the initial corrosion mechanism is of great importance. Moreover, previous studies have attributed propagating corrosion mechanisms

mainly to Cl-induced corrosion and the formation of metal chlorides, either through melt formation or the rapid release of Cl as a result of PbCl₂ decomposition, with little discussion of the role that Pb plays in the corrosion process (see *Section 5.5*).

- ❖ **Paper III** aims to develop a framework that integrates oxide microstructure characterization (specifically oxide grain size), kinetic simulations, and operational boiler data to simulate material losses in superheater tubes exposed to waste-fired boiler environments. A key part was to investigate the influence on grain boundary diffusion (α -value), which represents the reduction in the activation energy for diffusion along grain boundaries compared to bulk diffusion, based on Cl load and material.

Table 7.1 describes the different alloys and their chemical compositions, studied in Part I of this thesis and the appended papers. All the materials are commercially available and were supplied by Alleima AB and Kanthal AB.

Table 7.1: Chemical compositions of the different alloys used in Papers I–III.

Name	Alloy type	Paper	wt.%									Supplier
			Fe	Cr	Al	Ni	Mn	Si	Mo	Cu	Minor elements	
316Ti	Austenitic stainless steel	I	Bal.	16.5	-	11	2	0.8	2.1	-	C, S, P, Ti	Alleima AB
SX	Austenitic stainless steel	I	Bal.	17.5	-	19.5	0.5	5.0	0.4	2.0	C, S, P	Alleima AB
Kanthal® EF100	FeCrAl	I	Bal.	10.1	4.0	-	< 0.2	0.3	-	-	C, RE*	Kanthal AB
Kanthal® EF101	FeCrAl	I	Bal.	12.4	3.7	-	< 0.1	1.3	-	-	C, RE*	Kanthal AB
Sanicro® 69	Ni-based	I	10	30	-	60	< 0.5	0.5	-	-	C, S, P	Alleima AB
T22	Low-alloyed steel	II	Bal.	2.2	-	-	0.5	0.3	0.9	-	C (0.08), P (0.01), S (0.01)	Alleima AB
13CrMo4-5	Low-alloyed steel	III	Bal.	0.7-1.15	-	-	0.4-1.0	<0.35	0.4-0.6	-	C (0.08-0.18)	N.A
16Mo3	Low-alloyed steel	III	Bal.	<0.3	-	-	0.4-0.9	<0.35	0.25-0.35	-	C (0.12-0.20)	N.A
10CrMo910	Low-alloyed steel	III	Bal.	2-2.5	-	-	0.4-0.8	<0.5	0.9-1.1	-	C (0.08-0.14)	N.A

*Reactive element

7.1 Experimental: Paper I

The exposures in **Paper I** were conducted in the loop seal section of an 85-MW_{th} waste-fired CFB boiler located in Sweden, owned and operated by E.ON Energy Infrastructure AB (see Fig. 7.2a for a schematic drawing of the boiler, and the position of the exposed samples). The circulating bed material consisted of roughly 70 wt.% fuel ash and 30 wt.% natural sand. The fuel composition is

shown in Fig. 7.2b and consists of industrial and household waste, with minor fractions of recycled waste wood, fuel oil, chromated copper arsenate (CCA)-treated wood, and forest residue.

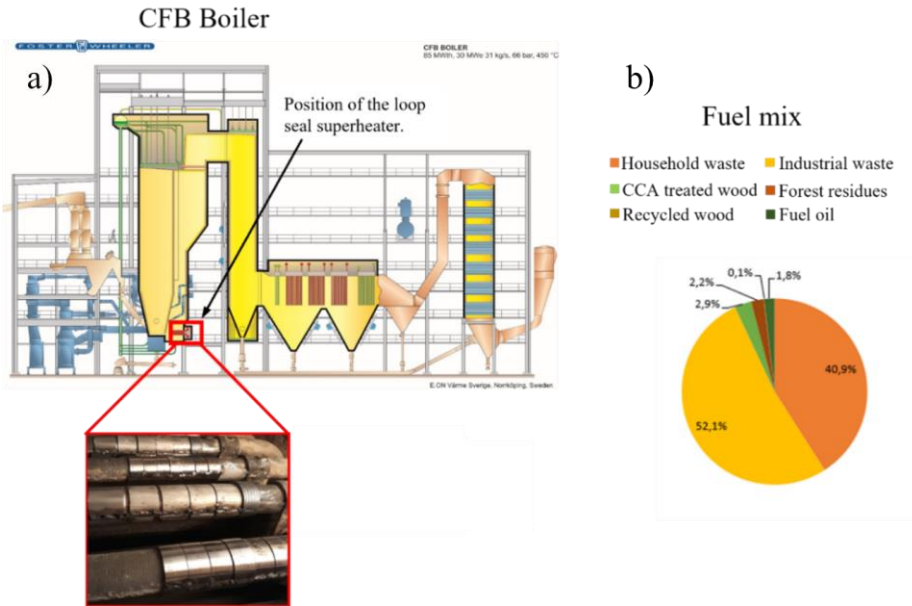


Fig. 7.2: (a) Schematic of the CFB waste-fired boiler and a photograph of the position of the exposed samples; (b) The fuel mix.

For each alloy type, two sets of half-moon sample rings were prepared and mounted on the top and bottom rows of the loop seal superheater tube bundle. The samples were mounted at two positions on the fluidized bed heat exchanger tubes, relative to the loop seal air flow direction, as follows:

- ❖ Windward position: facing downwards towards the loop seal air nozzles.
- ❖ Leeward position: facing upwards towards the return leg of the cyclone.

For this study, the samples positioned on the windward side were analyzed. Prior to exposure, the thicknesses of the clamps were measured three times around the sample using an Olympus 27MG ultrasonic thickness gage (UTG) with 0.01-mm resolution. The material surface temperatures facing the fireside were estimated using a boiler design software alongside the measured inlet and outlet steam temperatures. Based on the measured data, a material temperature in the range of 500°–520 °C was obtained.

After exposure the samples were embedded in epoxy and cut with an automated saw to obtain cross-sectional samples. The cross-sections were ground down to 4000 grit, using silicon carbide (SiC) abrasive papers. To enhance the conductivity and the imaging contrast for the SEM analysis, a thin gold film was deposited onto the samples using Au-sputtering with a Quorum 150 sputter coater. Material loss was quantified by comparing the original thickness measured with the UTG instrument before exposure and the remaining thickness measured with SEM (averaging nine datapoints across the entire cross-section). In this study, intergranular corrosion attack and internal nitridation were not included in the material loss assessment.

7.2 Experimental: Paper II

In **Paper II**, the aim was to investigate the corrosive effect of PbCl_2 on low-alloyed steel (T22) and, in particular, to address the individual roles of Pb and Cl. For this, a time-resolved study was

carried out in a well-controlled laboratory environment. Prior to exposure, the material was cut into coupons with nominal dimensions of $15 \times 15 \times 2$ mm, and holes were drilled at distances of approximately 7.5 mm and 2 mm from the edges. The surface edges were mechanically ground in water using SIC abrasive paper down to 1000 grit. Subsequently, the samples were automatically ground in water using the Struers TegraPol-31 polishing instrument with SIC abrasive paper down to 320 grit, and then polished with three diamond suspensions of 9, 1 and 0.5 μm until a mirror-like appearance was achieved. The samples were degreased and cleaned by immersion in acetone under ultrasonic agitation for 15 minutes using the Elmasonic P ultrasonic bath.

A total of 0.185 mg/cm^2 of PbCl_2 (0.0925 mg/cm^2 on each side) was deposited onto the polished sample surface by spraying a PbCl_2 -deionized water solution while continuously heating the sample using hot air, to ensure rapid solvent evaporation. To verify the correct amount of salt deposition, a SartoriusTM balance with microgram resolution was used to weigh the sample before and after deposition.

In addition, samples with 0.185 mg/cm^2 PbO were prepared using the same method, in response to findings obtained for the PbCl_2 -deposited samples (see *Section 7.4.2*). Reference samples without PbCl_2 or PbO deposition were also prepared for comparison study.

A schematic of the horizontal tube furnace setup is presented in Fig. 7.3. The exposures were carried out isothermally at $400^\circ\text{C} \pm 2^\circ\text{C}$ using an 80-mm-diameter silica tube. The samples were exposed to a continuous gas flow that contained $5\% \text{ O}_2 + 20\% \text{ H}_2\text{O} + \text{N}_2 \text{ bal.}$ at a flow rate of 3 cm/s for 1, 24 and 168 hours. Three samples were placed side-by-side in the alumina sample holders, parallel to the gas flow. The gas flow was measured with the Definer 2020 flowmeter, and the vapor content of the gas was measured by connecting a water bath, set at 60°C , to the system, whereby the water vapor was added to the gas via a Nafion membrane. The water vapor content was measured at the exit of the membrane just before the entrance to the horizontal tube furnace, using the Mitchell Instruments Optidew VisionTM chilled mirror humidity sensor.

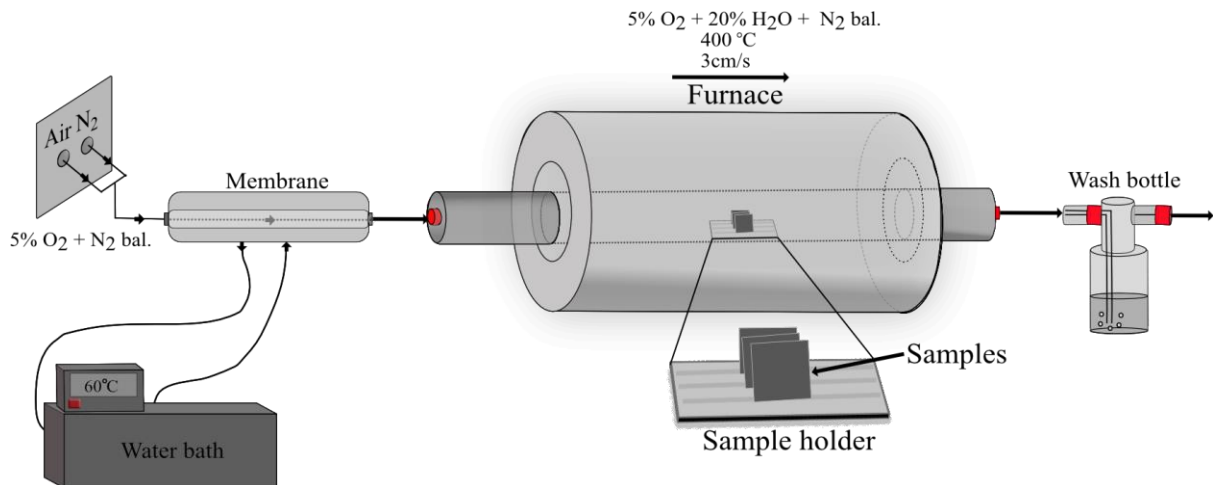


Fig. 7.3: Schematic of the furnace setup used in Paper II.

To generate high-quality cross-sections after exposure, the samples were prepared using BIB-milling. Before milling, a thin silica wafer was attached to the exposed surface of each sample and left to dry overnight. The samples were then sectioned and polished to a $0.5 \mu\text{m}$ surface finish using the Leica EM TXP instrument, which was operated at low speed and without lubricant. The cross-sectional BIB milling configuration described in *Section 6.2* was employed.

7.3 Experimental: Paper III

The development of the framework for modeling material degradation in superheater tubes within a waste-fired boiler, as presented in **Paper III**, is depicted in Fig. 7.4.

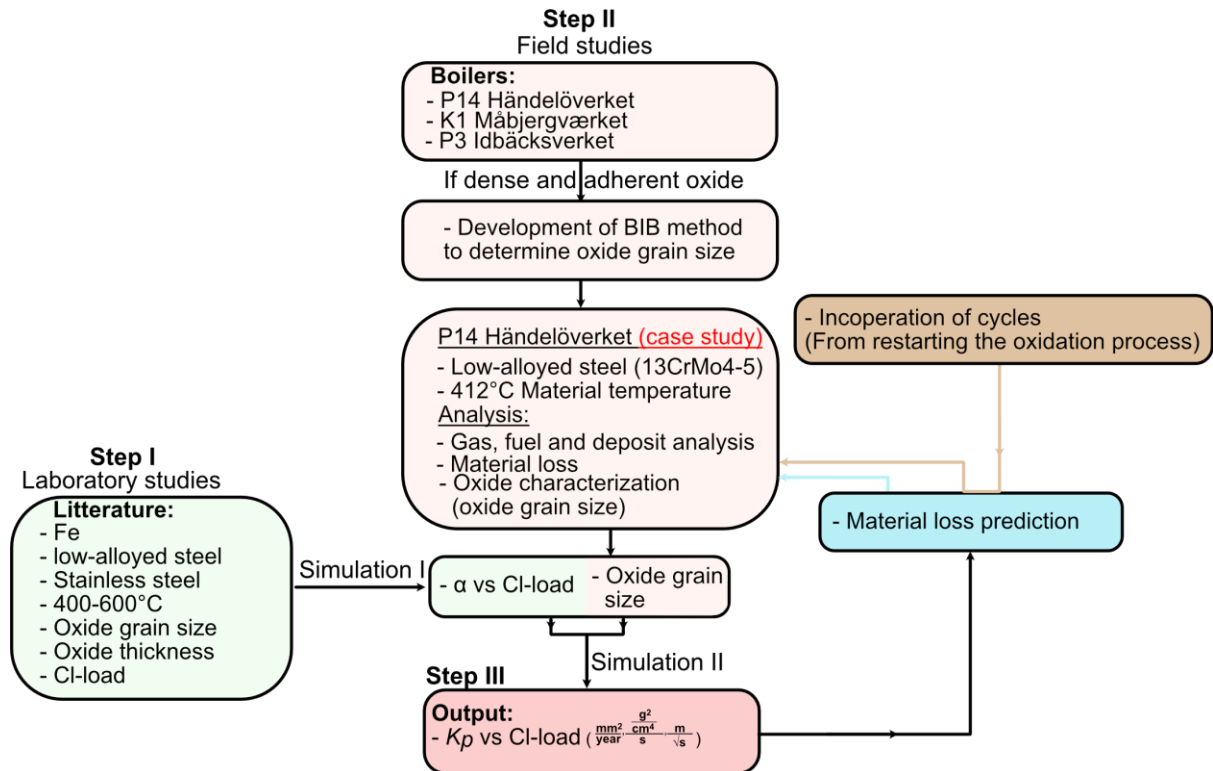


Fig. 7.4: Flowchart illustrating the workflow in *Paper III*. DICTRA simulations based on data from literature on well-controlled laboratory studies were carried out to determine α -values as a function of Cl-load. These simulation results were then combined with oxide grain size measurements from the field-exposed sample in the P14 boiler at Händelöverket to simulate derive K_p values vs Cl-load. From this, material loss calculations were carried out and compared with the actual material loss measured in the field sample. In cases of discrepancy, boiler operating conditions, specifically thermal cycling, were considered and discussed.

Step 1: a literature review was conducted on corrosion studies in well-controlled laboratory environments relevant for superheater application in this environment. The selection criteria for the literature were: 1) the oxide grain size is clearly visible, 2) the microstructure is considered representative of the environment and 3) variation of the concentration of Cl in the environment (i.e., different Cl-loads). From the literature review, the oxide thickness, average oxide grain size and Cl-load was determined. The oxide grain size was evaluated using SEM imaging and quantified through the Average Grain Intercept (AGI) method described in *Section 6.4*. DICTRA simulations were performed using literature-derived input data, assuming parabolic growth kinetics to model diffusion-controlled processes. While the simulations focus on the oxidation of pure iron, the experimental data also includes low-alloyed steel and stainless steel exposed to complex environments. The output of the DICTRA simulation generates a α -value and K_p value that varies as a function of Cl-load. It should be mentioned that due numerical difficulties associated with performing DICTRA simulations at low temperatures, all simulated K_p values presented in this work were extrapolated to the relevant temperature range using an Arrhenius-type relationship:

$$k = A \cdot e^{\frac{-E_a}{R \cdot T}} \quad (Eq. 16)$$

where k is a rate constant, A is a pre-exponential factor, E_a is the activation energy, R is the universal gas constant and T is the temperature. Three temperatures were used (600, 625 and 650 °C) and a generic temperature dependence of the K_p -value was calculated in each case.

Step 2: Microstructural analysis was conducted on low-alloyed steels exposed in three waste-fired boilers: P14 Händelöverket, K1 Måbjergværket and P3 Idbäcksverket. The samples were cut to obtain cross-section and polished down to 1µm using a diamond suspension. The samples were subsequently BIB-milled using the flat-milling technique described in *Section 6.2*. Oxide scales from the three boilers were analyzed for grain size using the AGI method outlined in *Section 6.4* and the oxide microstructure and adherence was evaluated. The two latter characteristics serve as indicators of parabolic oxide growth kinetics, thereby supporting the applicability of the DICTRA modeling approach employed in Step 1.

Among the three boilers, a case study was conducted on the P14 circulating fluidized bed (CFB) waste-fired boiler at Händelöverket (Fig. 7.5a). The position of the superheater tube analyzed is shown in Fig. 7.5b. The material of the superheater tube was the low-alloyed steel 13CrMo4-5 (see Table 7.1 for its chemical composition). The exposure lasted for a total of 4.1 years (36 000 hours), with an average material temperature of 412 °C, calculated based on measured steam temperature, flue gas temperature, and superheater geometry. Oxide grain sizes measured from this sample were incorporated into the DICTRA model, alongside α -values derived from laboratory experiments. The simulation results provided varying parabolic growth rate constants (K_p) as a function of Cl-load. Additionally, comprehensive gas-, fuel-, and deposit analyses were performed to characterize the operational environment and support the interpretation of the corrosion behavior. The flue gas composition and measured flue gas temperatures throughout the exposure period are provided in the appended Paper III. The installed superheater tubes were evaluated by remaining material thickness during revision stops continuously over their full installation time. This was done by ultrasonic measurements using a Echometer 1077. In total, 9 measurements were performed over the course of about 3.7 years.

Step 3: The derived K_p values were subsequently used to calculate the predicted material loss of the superheater tube from Händelöverket. This calculated material loss was then compared with the

actual material loss measured. The impact of operational conditions and cyclic oxidation was also considered in the analysis and discussion of material loss rate.

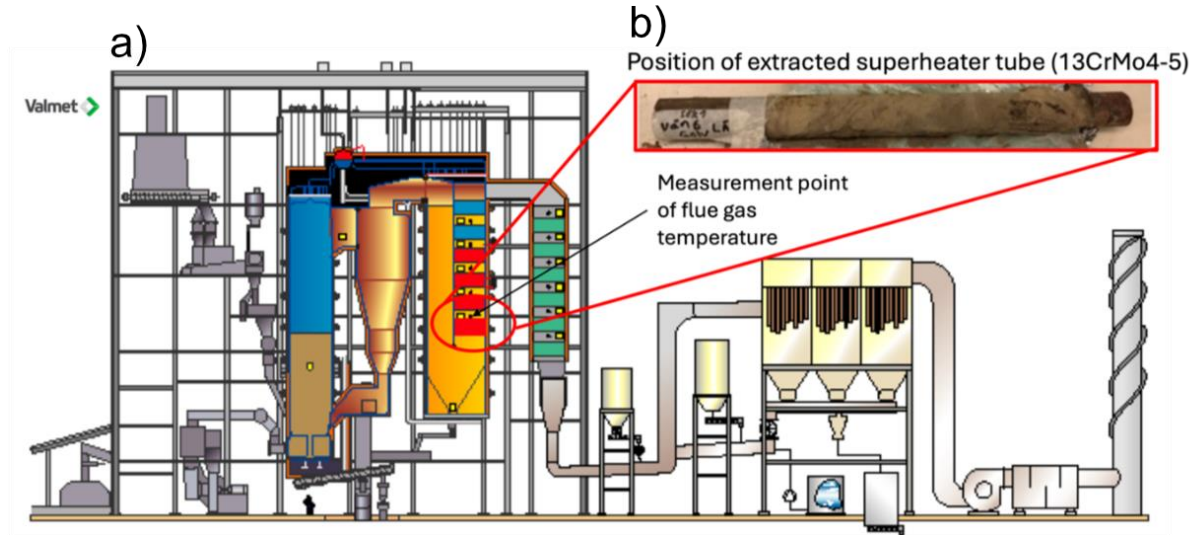


Fig. 7.5: a) Schematic of the P14 waste-fired boiler in Händelöverket, designed by Valmet. Courtesy of E.ON AB; b) Photograph of the superheater tube analyzed in the case study, highlighting the area from the location from which the tube was extracted, and measurement point of the flue gas temperature.

7.4 Results & discussion

7.4.1 Paper I- degradation behavior of superheater materials positioned in the loop seal of a waste-fired CFB boiler

7.4.1.1 Material loss

Fig. 7.6 presents the material loss for each sample. A notable increase in material loss was observed for the austenitic stainless steel 316Ti after 6 months of exposure, as compared with the other alloys, with a similar trend persisting after 12 months of exposure. The austenitic stainless steel SX exhibited minimal material loss after 6 months of exposure. Both FeCrAl alloys demonstrated high-level resistance to material degradation, with EF100 maintaining this trend even after 12 months of exposure. The Ni-base alloy Sanicro 69 showed slightly higher material loss than the SX after 6 months of exposure. Unfortunately, the EF101 and Sanicro 69 alloys exposed for 12 months could not be recovered.

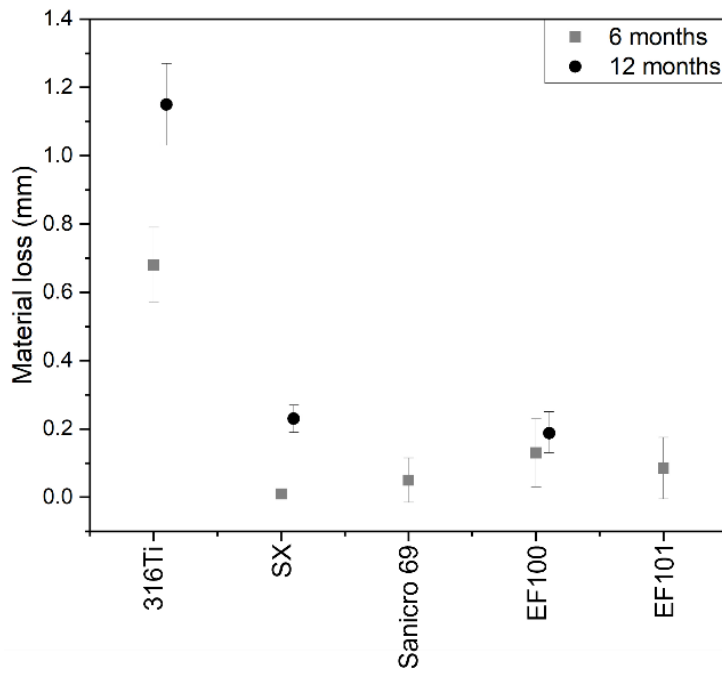


Fig. 7.6: Extent of material loss for each alloy type tested.

7.4.1.2 Microstructural analysis

Cross-sectional analyses were carried out to identify the corrosion products of the exposed alloys. These analyses were performed to improve understanding of the interplay between erosion and corrosion attacks in this environment. A summary of the observed corrosion products and material losses is presented in Table 7.2.

Table 7.2: Summary of the results of the microstructural analyses carried out in Paper 1.

Name	Alloy type	Exposure time (months)	Average material loss (mm)	Average internal/intergranular corrosion (mm)	Average nitridation zone (mm)	Deposit composition	Breakaway corrosion
316Ti	Austenitic stainless steel	6	0.70 ± 0.10	0.13 ± 0.03	-	-	Yes
SX	Austenitic stainless steel	6	0.01 ± 0	0.07 ± 0.01	-	O, Ca, S, Cl, Na	Yes
Sanicro 69	Ni-based	6	0.05 ± 0.01	0.23 ± 0.04	-	O, Ca, S, P, Mg	Yes
EF100	FeCrAl	6	0.13 ± 0.10	-	0.1 ± 0.90	O, Mg, Ca, S, P, Si	Yes
EF101	FeCrAl	6	0.09 ± 0.10	-	0.42 ± 0.22	O, Ca	Yes
316Ti	Austenitic stainless steel	12	1.15 ± 0.12	0.23 ± 0.02	-	-	Yes
SX	Austenitic stainless steel	12	0.23 ± 0.04	0.19 ± 0.04	-	O, Ca, S, Cl, Na	Yes
EF100	FeCrAl	12	0.19 ± 0.06	-	0.43 ± 0.07	O, Ca, S, Mg, Cl	Yes

The microstructural investigation showed that all the materials experienced breakaway corrosion after 6 months of exposure (see Figs. 7.7–7.9). In the case of the austenitic stainless steel 316Ti, severe spallation of the oxide scale was observed after both 6 and 12 months of exposure. It is

possible that the oxide and deposit scale detached either during operation or sample preparation. The limited areas in which the oxide scale remained on the alloy surface were enriched for Cr, together with Fe, as confirmed by EDX mapping and point analysis (see Fig. 7.7). The oxide scale is assumed to be the remnant of an inward-growing Cr-rich spinel and should not be confused with a primary protective $(\text{Fe,Cr})_2\text{O}_3$ corundum. This conclusion is supported by several factors, including the high level of material loss observed for 316Ti and the intergranular corrosion attack observed below the oxide scale.

The intergranular corrosion primarily consisted of a Cr-rich oxide along the grain boundaries. A similar oxide morphology has been reported in previous studies using comparable materials and environments [54]. According to the SEM/EDX point analysis (not shown), the Cr content at the center of the alloy grain in the intergranular corrosion region was 3–6 at.% (3–9 wt.%), indicating severe Cr-depletion. It is argued that this concentration of Cr is insufficient to support the formation of a continuous oxide layer in this region. Furthermore, at this temperature and with this material, grain boundary diffusion occurs rapidly, which explains why the oxidation is preferential at the grain boundaries. After 12 months of exposure, intergranular corrosion was observed to a greater extent (see Fig. 7.7b). In general, internal oxidation, such as intergranular oxidation, offers poor protection for the material, as it fails to form a continuous oxide scale that restricts ion diffusion to the metal/oxide interface. Furthermore, internal oxidation causes embrittlement, which can cause affected zones to flake off [96].

A comparison of the material losses between the two austenitic stainless steels SX and 316Ti, shows that SX manifests better resistance towards material degradation. The deposit formed on SX consisted mainly of O, S, Ca, and traces of Na and Cl. Underlying this layer, an oxide scale with a thickness ranging from approximately 10 to 70 μm was observed, characterized by localized enrichment of Cr and the presence of Si. Similar observations were made after 12 months of exposure (Fig. 7.7d). However, after 12 months of exposure, internal oxidation had propagated significantly in the alloy, and at a depth of approximately 60 μm below the metal/oxide interphase, there was notable depletion of Cr within the grain boundaries. In this region, the grain boundary was instead decorated with a Si-rich oxide. The phase of this oxide was not determined. Previous studies have highlighted the beneficial effect of alloying austenitic stainless steel with Si in enhancing its corrosion resistance [140, 141]. Specifically, investigations on austenitic stainless steel (353MA, containing 2.42 wt.% Si) exposed temperatures ranging from 700 °C to 900 °C in a humid environment demonstrated the formation of a silica layer. This layer propagated into the steel's grain boundaries, similar to what was observed in the present study [140, 141]. Silica is widely recognized for its excellent high-temperature corrosion resistance, serving as an effective diffusion barrier and enhancing the corrosion-protective properties of stainless steels [84]. It is tempting to conclude that the formation of a Si-rich oxide at the metal/oxide interphase and at the grain boundaries accounts for the observed reduced corrosion rate of SX, as compared with 316Ti. However, compared with 316Ti, SX contains higher concentrations of both Cr and Ni. Studies have shown that increased contents of these alloying elements in austenitic stainless steels enhance the protective properties of the resulting oxide scale, beyond breakaway corrosion [100]. With the current experimental setup, it becomes challenging to define the impact of each individual element on the corrosion properties. However, when comparing the material losses of the conventional austenitic steels 316 Ti and SX, it becomes apparent that SX acquires superior corrosion resistance in this environment.

It is important to note that the material loss mentioned in this study does not cover the intergranular corrosion attack. This choice was made because these regions were observed to be rather heterogeneous throughout the surface, making it challenging to define the actual material loss. It is evident that the intergranular attack on SX propagates over time, and this should be taken into consideration when discussing the performance of this alloy type, as it may reduce the mechanical properties of the alloy over time. The average thicknesses of the intergranular corrosion regions for SX and 316Ti after 12 months of exposure were 0.19 mm and 0.23 mm, respectively (see Table 7.2).

Austenitic Stainless steel

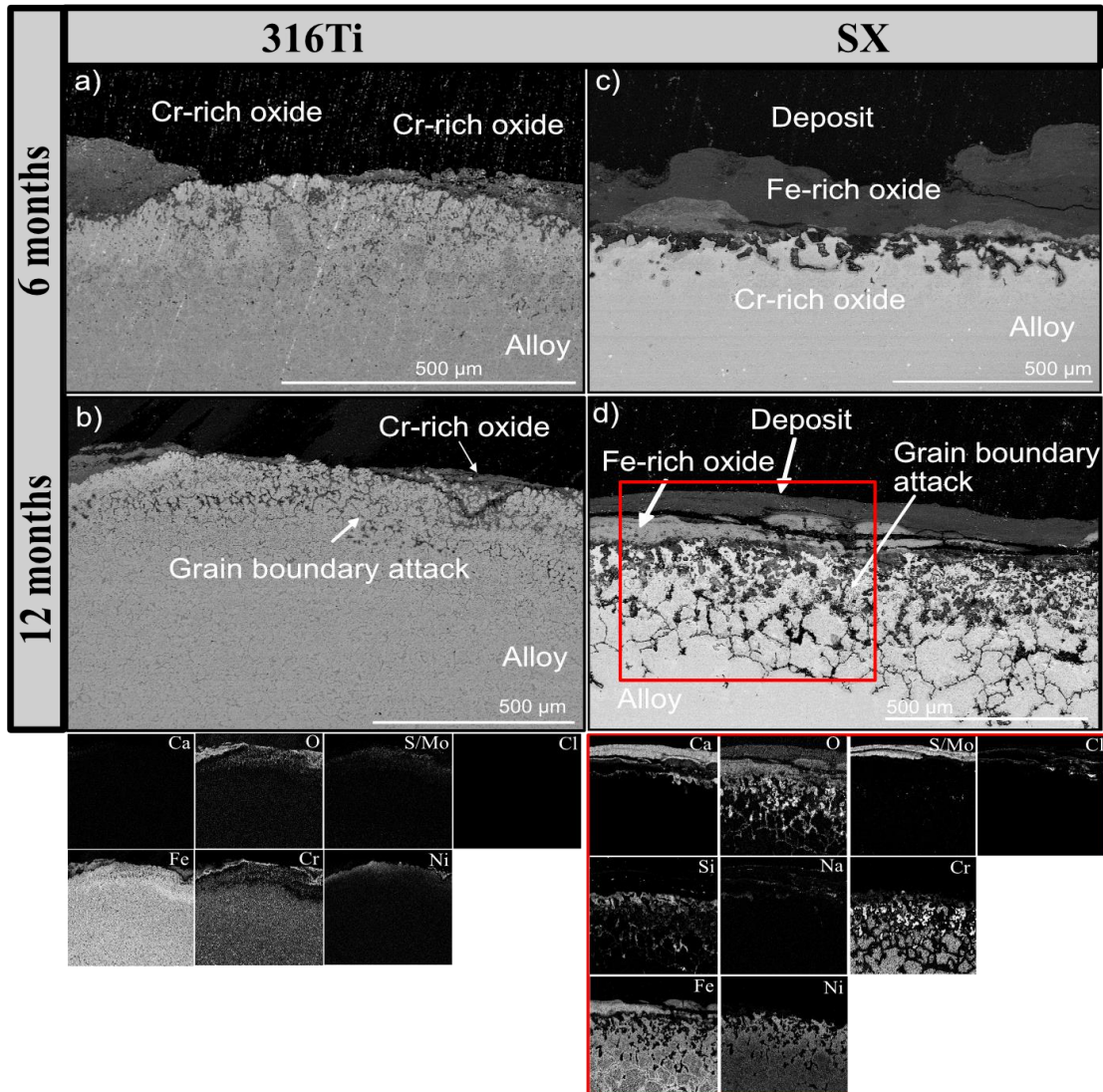


Fig. 7.7: SEM BSE cross-sectional images of 316Ti and SX: (a) 316Ti after 6 months of exposure; (b) 316Ti after 12 months of exposure and, in the bottom panels, EDX mapping of (b); (c) SX after 6 months of exposure; (d) SX after 12 months of exposure and, in the bottom panels, EDX mapping of (d).

Fig. 7.8 shows the cross-sectional SEM image of the Ni-based alloy, Sanicro 69 alloy after 6 months of exposure. A deposit layer with thickness of roughly 50 µm was observed that contained mainly S, Ca, and O, with traces of P and Mg. Although not apparent on the SEM/EDX map, EDX point analysis revealed a Cl content of approximately 2 at.% at the deposit layer. Beneath the deposited

layer, a Ni-rich oxide was present, indicating that breakaway corrosion had occurred. Below this, a Cr-rich oxide was detected. Unlike the stainless steels discussed previously, this Cr-rich oxide scale was not confined to the alloy grain boundaries but was distributed more uniformly across the alloy surface. Previous studies have demonstrated that the ability to form a more-continuous protective oxide scale beyond breakaway corrosion is highly dependent upon the Cr content of the alloy [100]. The Ni-based alloy used in this study contained over 30 wt.% Cr, which is roughly twice the amount of Cr in the two austenitic stainless steels. This elevated chromium content likely facilitates the development of a more uniform and adherent Cr-rich oxide scale, which can serve as an effective diffusion barrier. As a result, the transport of corrosive species to the alloy surface is reduced, thereby contributing to the comparatively low material loss observed for Sanicro 69.

In addition, a Cr-rich oxide was observed further into the metal, at a depth of approximately 80 µm below the corrosion product layer, most likely representing a 3D effect in this 2D cross-sectional image (Fig. 7.8a). Below the Cr-rich oxide scale, internal oxidation in the form of Cr-rich oxide precipitates was observed (see Fig. 7.9b). The Cr concentration in the alloy substrate in this region was around 12 wt.%, indicating significant Cr depletion. About 0.2 mm further down, the Cr content was similar to the original value for the alloy.

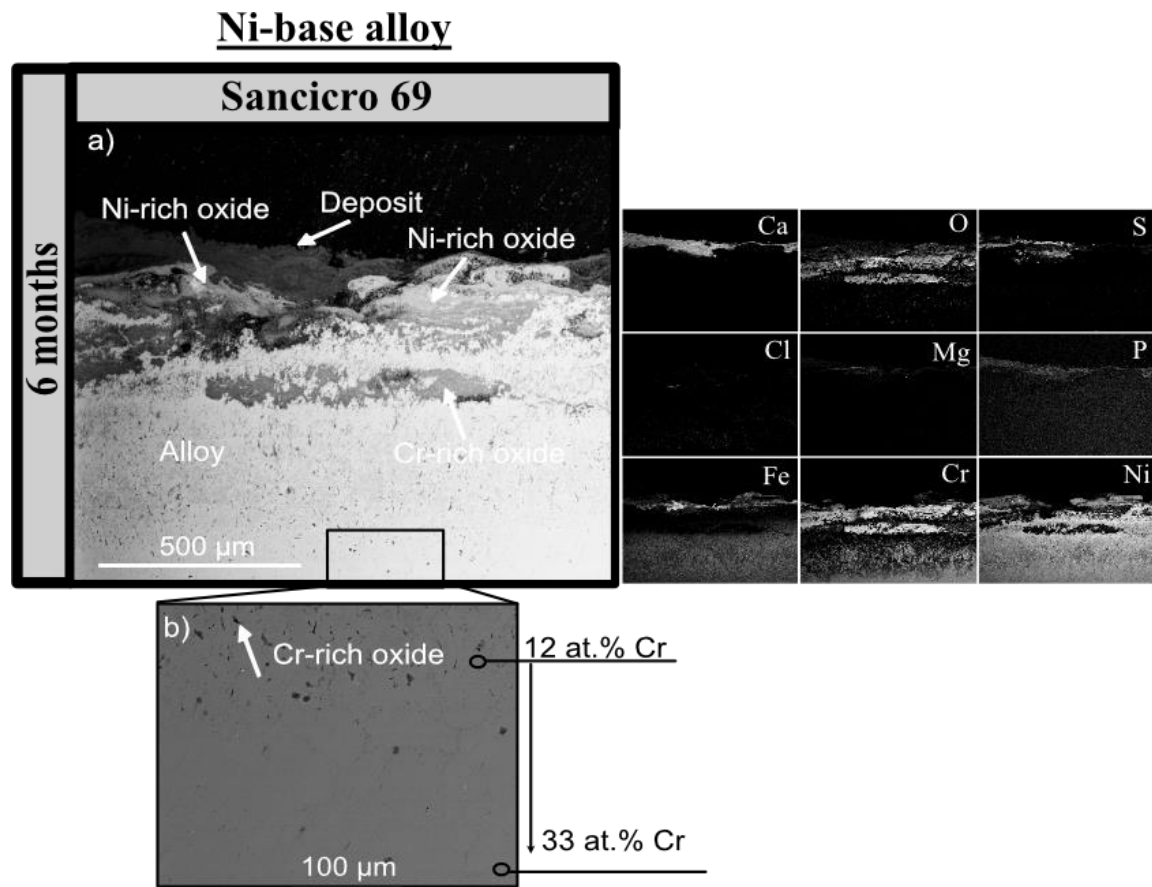


Fig. 7.8: SEM BSE cross-sectional images of Sanicro 69 after: (a) 6 months of exposure and, to the right, the EDX mapping of (a); (b) higher-magnification image of the area highlighted in (a), showing traces of Cr-rich oxide precipitates and the Cr concentration profile in the region of the oxide precipitate and the adjacent region below where no oxide has formed.

The FeCrAl alloys EF100 and EF101 exhibited comparable material losses after 6 months of exposure. Both alloys showed the presence of an outward-growing, Fe-rich oxide scale, indicating breakaway corrosion (Fig. 7.9, a and c). Traces of an Al/Cr-rich oxide scale were observed on both

alloys at the metal/oxide interphase after 6 months of exposure. Furthermore, both alloys exhibited Al-nitridation after 6 months of exposure at different severities (shown for EF100 in Fig. 7.9b). EF100 showed a patch-wise nitridation zone throughout the cross-section, while the nitridation zone in EF101 was more significant and homogeneous over the whole cross-section (Fig. 7.9, a and c). Furthermore, in the nitridation zone, a low concentration of Cr (<3 at.%) was observed for both samples. The nitridation zone in EF100 became more extensive after 12 months of exposure, yet the level of material loss was low (Fig. 7.9d). The low material losses exhibited by these alloy types while undergoing severe nitridation may seem counterintuitive, as the formation of Al-nitrides locks the Al in place, which could otherwise be utilized for the formation of a more-protective Al-rich oxide scale. In this study, the material temperature was in the range of 500°–520 °C. At these temperatures, FeCrAl alloys form a transient alumina scale rather than α -Al₂O₃ as a primary protective oxide scale. It has been reported that such transient alumina contains high concentrations of Cr, and that breakaway corrosion in this regime is primarily driven by Cr-depleting mechanisms, such as chromate formation [98]. However, the Al-content of the inward-growing oxide formed beyond breakaway corrosion has been shown to play a significant role in resistance to corrosion in harsh environments [98]. From the mechanical standpoint, nitridation-related precipitates may cause alloy embrittlement and reduced ductility, potentially compromising the integrity of the material. While nitridation did not result in significant material losses in this study, further research is required to assess its long-term impacts on the mechanical properties and corrosion behaviors of different alloys.

FeCrAl alloy

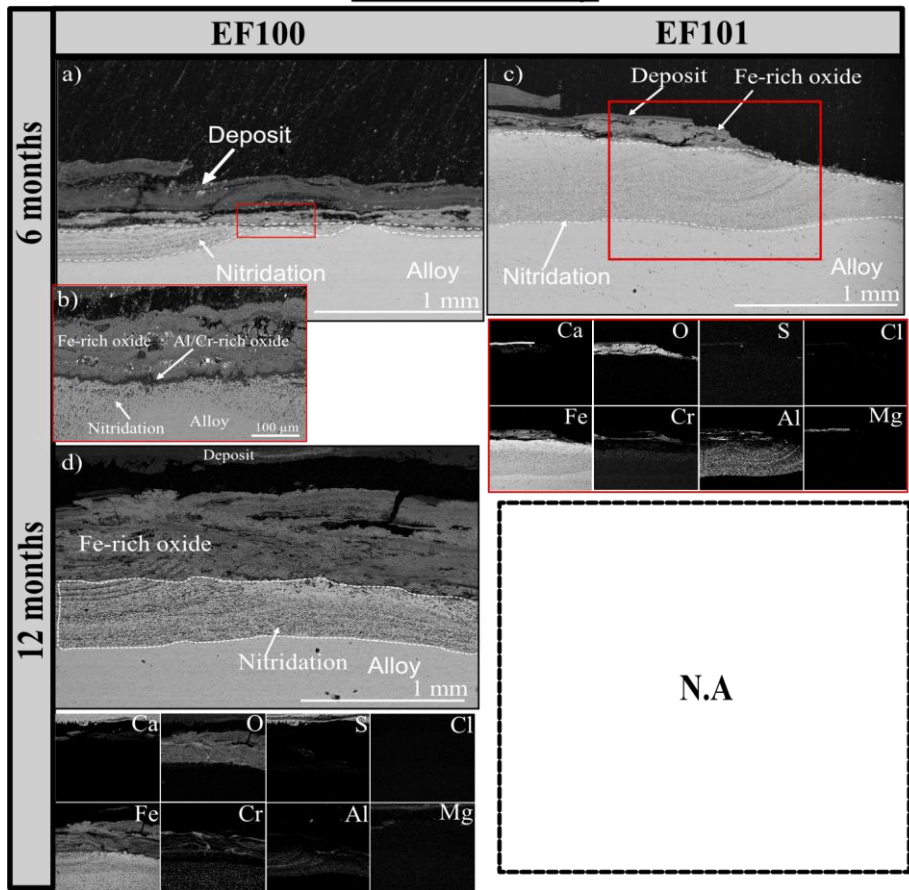


Fig. 7.9: SEM BSE cross-sectional images of EF100 & EF101: (a) EF100 after 6 months of exposure, (b) higher-magnification image highlighted area in (a). (c) EF101 after 6 months of exposure. (d) EF100 after 12 months of exposure and EDX map below.

❖ Corrosion vs erosion

Revisiting the question as to whether corrosion, erosion or a combination of both drives the degradation rate of superheater materials in the loop seal region of waste-fired boilers, the answer turns out to be highly complex under actual operating conditions. In boiler environments, the positioning of the superheaters plays a significant role in the corrosion behavior, as local conditions strongly influence deposit accumulation, the incident angle of bed material hitting the superheating tube (i.e., erosion rates), and ultimately the degradation rate [142, 143]. Therefore, the discussion in this section will consider the broader context. Further, more well-controlled studies are needed to understand fully the interplay between corrosion and erosion in this area of the boiler.

The microstructural analyses showed that all of the tested alloy types had undergone breakaway corrosion after 6 months of exposure, confirming that the environment is corrosive. Although a detailed analysis of the deposit composition was not conducted, the deposits generally contained high levels of sulfur and alkali species. The relatively low Cl content suggests a low Cl/S ratio in the loop seal. In general, alkali sulfates are considered to be less aggressive than alkali chlorides; however, the presence of Cl in some areas of the deposits might still contribute to increased corrosion. In this study, the Sanicro 69 sample displayed a Cr-rich oxide scale beneath a Ni-rich oxide scale, which is argued to enhance the corrosion resistance properties. The FeCrAl alloys also showed the formation of an Al/Cr-rich oxide scale beneath the Fe-rich oxide scale, which is suggested to improve the resistance to corrosion [100].

Studies conducted in well-controlled laboratory environments have shown that Ni-based alloys can experience higher degradation rates than stainless steel in erosive-corrosive environments at 550 °C, as compared with a pure corrosive environment [144]. This was attributed to the slower growth rate of the oxide scale on Ni-based alloys, which under severe erosion conditions, prevents the formation of a continuous and protective oxide layer. This is what is shown in Fig. 5.2 and described as being within the oxidation-affected erosion regime. As a result, the underlying alloy is exposed to the environment, leading to accelerated degradation. However, no such mechanisms were observed in the present study, as the Ni-based alloy Sanicro 69 demonstrated low material loss and formed an adherent oxide scale.

For the 316Ti samples, hardly any deposits or oxide layers were observed, regardless of the exposure time (see Fig. 7.7a, and d). Previous studies conducted by Norling et al. have shown that areas subjected to high erosion can exhibit thicker oxide scales that adhere more strongly to the alloy substrate compared with regions without the influence of erosion [128]. This phenomenon has been attributed to the formation of voids at the metal/oxide interface, which occurs due to vacancy transport to this area, driven by the outward diffusion of cations. In the presence of erosion, however, short-circuit diffusion through cracks and pores becomes the rate-determining step, leading to the relief of stress in the oxide scale, enhancing its adherence. Furthermore, this has been linked to accelerating the transport of corrosive species to the metal/oxide interface, in a process known as ‘Type II erosion-enhanced corrosion’ (Fig. 5.2). Thicker oxide layers also increase the risk of spallation during sample preparation. Therefore, it is possible that the significant material loss observed for the 316Ti sample is due to severe oxidation promoted by erosion, with the oxide scale detaching during preparation owing to its thickness.

Based on the analyses conducted in this study and using the theoretical framework for erosion-corrosion described in Fig. 5.2, it is argued that the degradation mechanisms for various alloy types in the loop seal region of a waste-fired boiler cannot be attributed solely to erosion or oxidation-assisted erosion. For all the samples studied, degradation appears to result from either pure corrosion or corrosion-enhanced erosion, with erosion potentially playing a relatively minor role. This conclusion is supported by the microstructural analyses, which revealed signs of breakaway corrosion across all the samples, as well as the presence of oxide scales and deposits on most of the exposed surfaces. From the corrosion perspective, nitridation of the FeCrAl alloys EF100 and EF101 seems to have little effect on their degradation rates in this environment.

7.4.2 Paper II- PbCl₂-induced corrosion on low-alloyed steel

7.4.2.1 Oxide thickness

Fig. 7.10 shows the average oxide thicknesses of T22 exposed for 1, 24, and 168 hours in the following three environments: 5% O₂ + 20% H₂O (Reference); PbCl₂ + 5% O₂ + 20% H₂O; and PbO + 5% O₂ + 20% H₂O. In the presence of PbCl₂, a noticeable oxide thickness (of approximately 4 µm) was observed after just 1 hour of exposure. This thickness was roughly 40-times greater than those of samples exposed to PbO or samples without deposits after 1 hour of exposure. Over time, for the samples exposed to PbCl₂, the oxide thickness continued to increase, reaching approximately 6 µm after 24 hours and 15 µm after 168 hours. The samples exposed to PbO acquired a significantly thinner oxide than the PbCl₂-exposed samples. After 24 hours of exposure, the oxide thickness was similar to those of the samples exposed without any deposit, measuring approximately 0.1 µm and 0.7 µm after 1 hour and 24 hours, respectively. However, after 168

hours, the oxide of the PbO-exposed sample appeared to be thinner than that of the sample without any deposit.

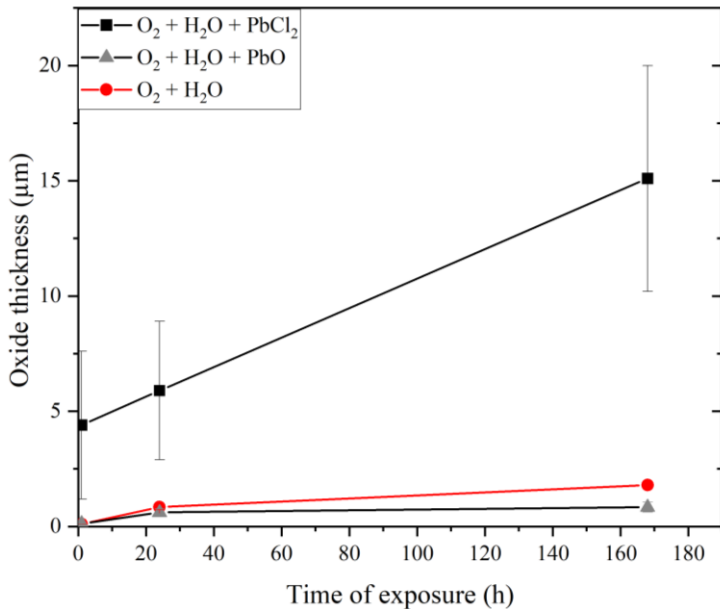


Fig. 7.10: Average oxide thickness of T22 following exposures for 1, 24 and 168 hours at 400 °C to 5% O₂ + 20% H₂O + N₂ bal. + PbCl₂, 5% O₂ + 20% H₂O + N₂ bal. + PbO, and 5% O₂ + 20% H₂O + N₂ bal. (reference).

7.4.2.2 Microstructural analysis

Figs. 7.11–7.13 show SEM images of BIB-milled cross-sections of T22 after exposure to PbCl₂ for 1, 24 and 168 hours respectively. XRD and SEM/EDX analyses confirmed that, following 1 hour of exposure, PbCl₂ reacted to form mendipite (Pb₃Cl₂O₂) on the sample surface (refer to Fig. 7.11a and b for SEM/EDX analysis, and to appended Paper II for the corresponding XRD spectra). Furthermore, from the SEM/EDX map analysis, it was evident that Cl had migrated from the surface to the metal/oxide interface (see Fig. 7.11a and the corresponding EDX maps). The SEM/EDX point analysis (not shown) and map analysis suggested the formation of iron chlorides. The oxide scale comprised an outward-growing, Fe-rich oxide and an inward-growing (Fe,Cr)₃O₄ oxide. Lastly, severe delamination of the oxide scale was observed beneath the areas with high concentrations of Pb₃Cl₂O₂ while a more-adherent oxide scale was observed in regions that had little or no Pb₃Cl₂O₂ present.

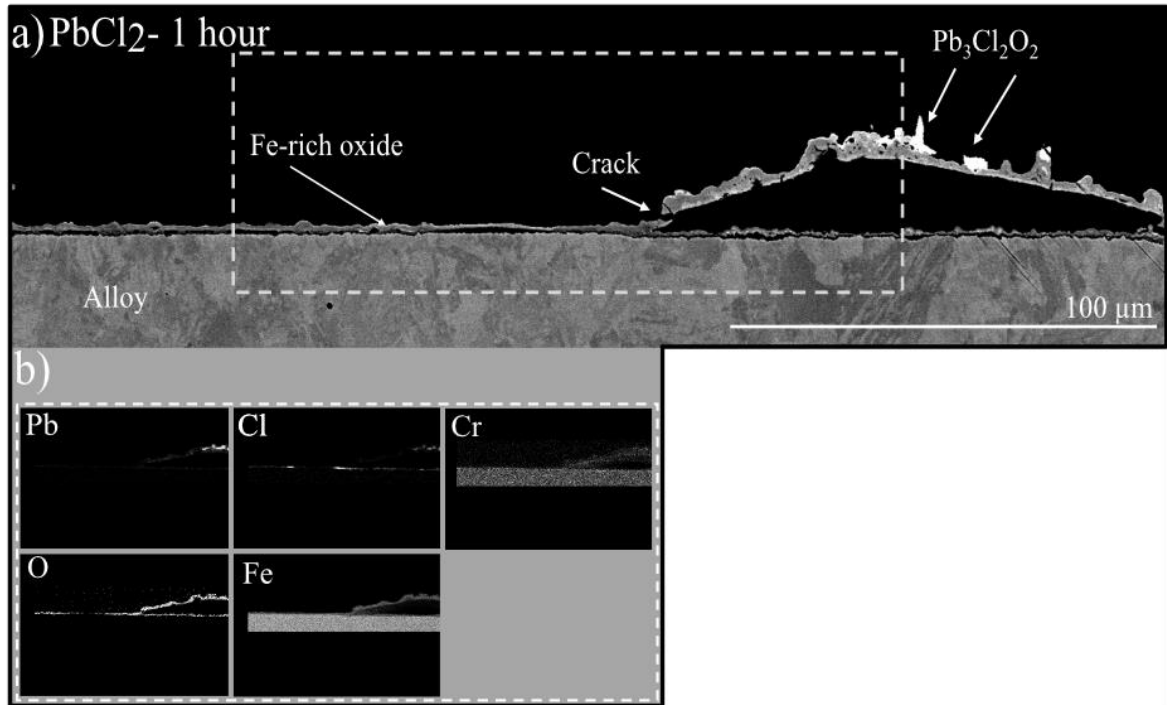


Fig. 7.11: BIB-milled SEM BSE cross-sectional image of T22 exposed at 400 °C to $\text{PbCl}_2(s)$ + 5 % O_2 + 20% H_2O + N_2 bal. for 1 hour: (a) Overview; (b) EDX map of highlighted dashed-box area in (a).

Fig. 7.12a shows the BIB-milled cross-section after 24 hours of exposure to PbCl_2 . Mendipite had further reacted to form PbO . This was confirmed by SEM/EDX map analysis (for the corresponding EDX maps, see Fig. 7.12c), and XRD (see appended Paper II for the corresponding XRD spectra). Similar to the sample exposed for 1 hour, delamination of the oxide scale was observed in regions with high concentrations of the original PbCl_2 deposit. Typical features of these oxide layers are shown in Fig. 7.12b. An Fe-rich oxide scale had grown on top of a delaminated Fe-rich oxide scale that appeared to have hematite whiskers forming on top. Below the Fe-rich oxide scale, a $(\text{Fe},\text{Cr})_3\text{O}_4$ oxide had formed. The bright spots visible in the $(\text{Fe},\text{Cr})_3\text{O}_4$ oxide are Mo. A similar multilayered oxide has been described in previous studies for T22 exposed at high temperatures [103]. Chlorine was detected near the metal/oxide interface, most likely in the form of iron chlorides.

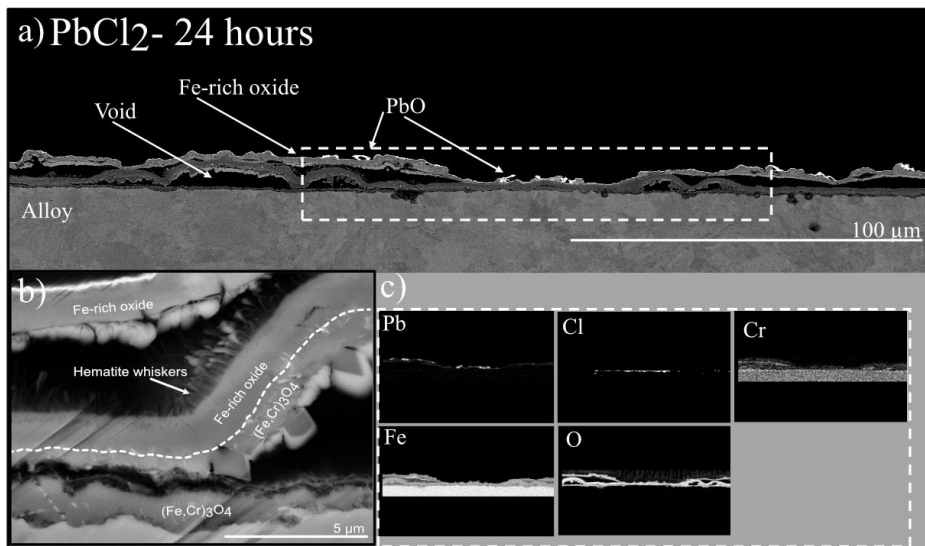


Fig. 7.12: BIB-milled SEM BSE cross section image of T22 exposed at 400 °C in $\text{PbCl}_2(s)$ + 5% O_2 + 20% H_2O + N_2 bal. for 24 hours: (a) Overview; (b) High-magnification image of region with delamination occurring, (c) EDX map of highlighted dashed-box area in (a).

After 168 hours of exposure, similar features were observed, with increased thickness observed in regions close to the original PbCl_2 particles (see Fig. 7.13a). The scales were more porous and exhibited cracks, delamination, and voids. Severe cracking of the oxide was observed in areas where the oxide grew inside pre-existing voids. The oxide scales in these regions were highly fragmented and it was challenging to determine their exact compositions. For the more-adherent oxide scales, SEM images revealed bright regions on top of the oxide scale (see Fig. 7.13b). This was confirmed by XRD analysis to be either PbO or Pb_3O_4 (see appended Paper II for corresponding XRD spectra). An Fe-Pb-O oxide layer, approximately 1–2 μm in thickness, was observed at the oxide/air interface in proximity to the original PbCl_2 particles. This oxide phase was not consistently present throughout the scale. The SEM/EDX analysis indicated that these regions contained approximately 3 at.% Pb, 38 at.% Fe, and 59 at.% O. Below this layer, an outward-growing, Fe-rich oxide was identified. The inward-growing oxide consisted of $(\text{Fe},\text{Cr})_3\text{O}_4$, with bright spots corresponding to Mo precipitates. In addition, EDX mapping revealed the presence of Cl at the metal/oxide interface.

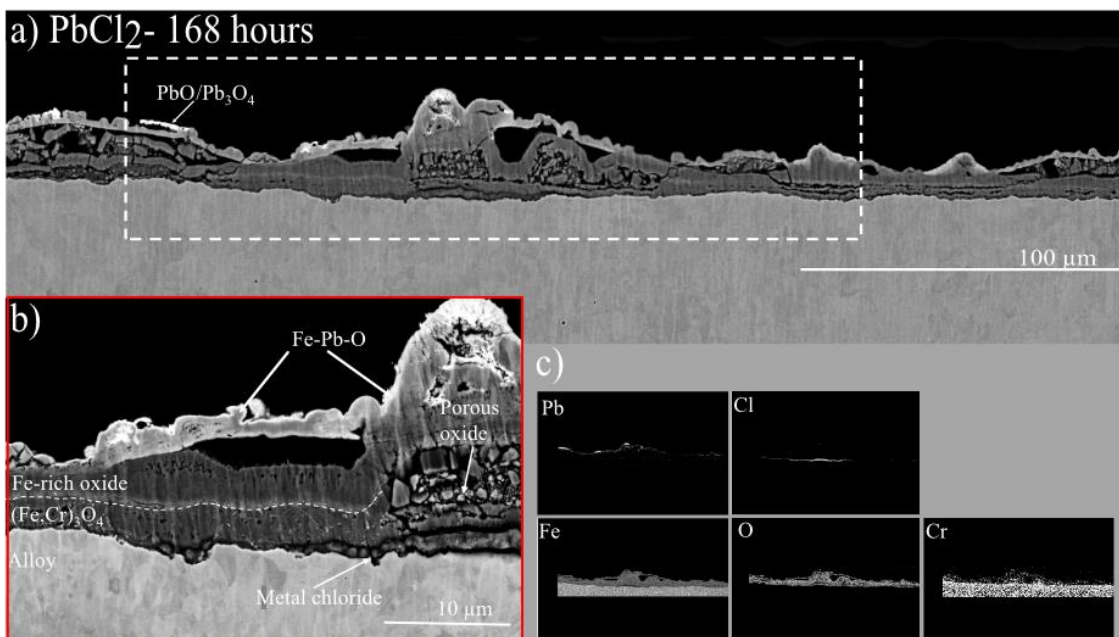


Fig. 7.13: BIB-milled SEM BSE cross-sectional image of T22 exposed at 400 °C to $\text{PbCl}_2(s)$ + 5% O_2 + 20% H_2O + N_2 bal. for 168 hours: (a) Overview; (b) High-magnification image of the area highlighted in the dashed-box in (a); (c) EDX map of the area highlighted in the dashed-box in (a).

The presence of PbO on the samples after just 24 hours of exposure raises questions regarding its influence on the rate of corrosion of T22. To investigate further its role in PbCl_2 -induced corrosion, T22 was exposed to PbO under the same conditions and for the same duration. The corrosion of T22 was lower in the presence of PbO compared to exposure in the presence of PbCl_2 (Fig. 7.10). Furthermore, the oxide thicknesses of the samples exposed to PbO were similar to those of the reference samples. BIB-milled SEM cross-sections of T22 exposed to PbO , along with reference samples, are shown in Fig. 7.14. In both cases, inward-growing $(\text{Fe},\text{Cr})_3\text{O}_4$ was observed on the alloy substrate, followed by an outward-growing Fe-rich oxide. These features were most-pronounced after 168 hours of exposure, as the oxide scale remained very thin and difficult to detect after 1 hour and 24 hours with the current SEM setup. Notably, there were differences in surface oxide morphology between the two conditions. On the reference sample, hematite whiskers were present on the surface, resembling those seen for PbCl_2 -exposed samples in areas distant from the PbCl_2 deposit. In contrast, when exposed to PbO , hematite formation appeared to be disrupted, and instead an Fe-Pb-O layer was present throughout the cross-section. XRD analysis suggested the formation of magnetoplumbite ($\text{Fe}_{12}\text{PbO}_{19}$) on the sample surface (see appended Paper II for corresponding XRD spectra). Notably, in both cases, no signs of spallation or crack formation of the oxide scales were evident. Therefore, oxide growth in these two scenarios is likely to be strictly diffusion-controlled via the oxide scale. Based on these findings, it is concluded that $\text{Fe}_{12}\text{PbO}_{19}$ plays a key role in the observed reduction in corrosion rate, likely due to its ability to slow the diffusion of ionic species through the oxide scale.

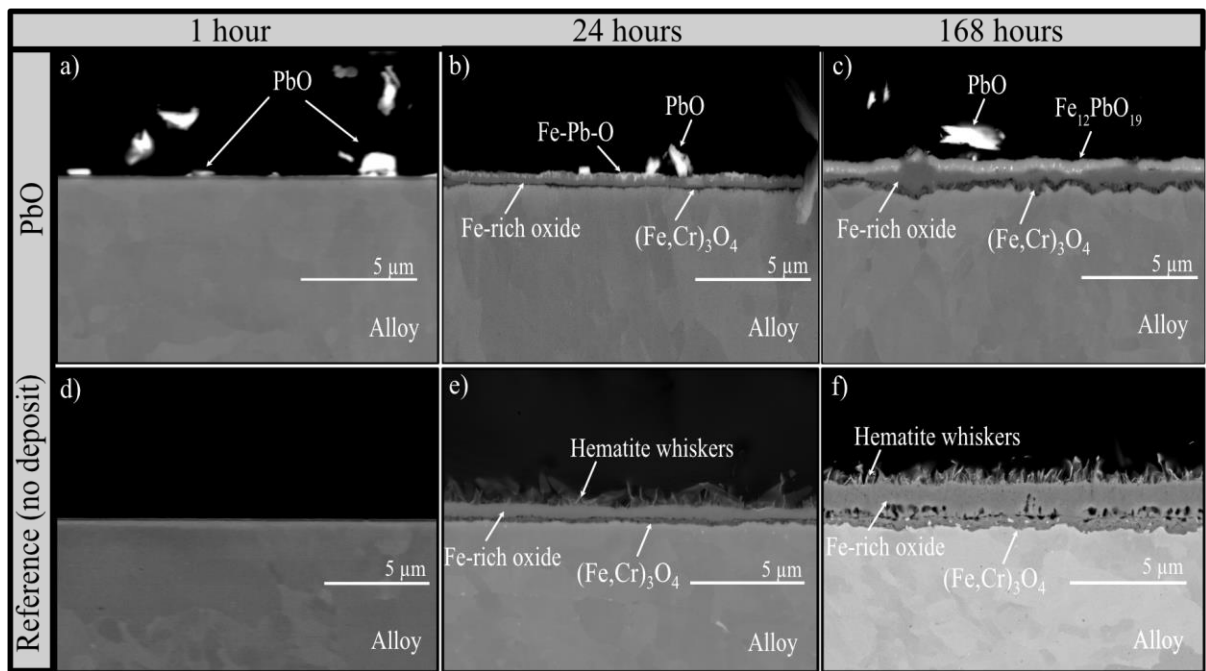
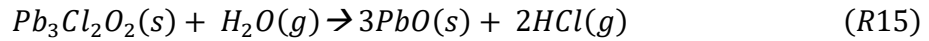
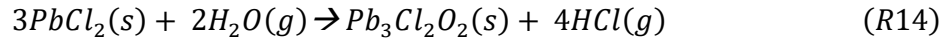


Fig. 7.14: BIB-milled SEM BSE cross-sectional images of T22 exposed at 400 °C to $\text{PbO}(s) + 5\% \text{O}_2 + 20\% \text{H}_2\text{O} + \text{N}_2 \text{bal}$. and to $5\% \text{O}_2 + 20\% \text{H}_2\text{O} + \text{N}_2 \text{bal}$. (reference): (a-c): 1–168 hours of exposure in the presence of PbO ; (d–f): 1–168 hours of exposure for the reference samples.

7.4.2.3 Proposed corrosion mechanism in the presence of $PbCl_2$

Based on the obtained results, a corrosion mechanism for T22 in the presence of $PbCl_2$ is proposed and illustrated in Fig. 7.15. It is proposed that Cl is released from $PbCl_2$ through a two-step process, resulting in the formation of $HCl(g)$:



Some $HCl(g)$ is then suggested to dissociate on the oxide surface, forming Cl ions in accordance with the electrochemical approach developed by Folkeson et al. [114]. By deploying an ion-based transport mechanism rather than gaseous species, as discussed in relation to active oxidation mechanisms, it is suggested that the inward diffusion of monovalent Cl^- occurs more rapidly than that of divalent O^{2-} . This faster diffusion of Cl^- relative to O^{2-} leads to a lower oxygen concentration in proximity to the metal/oxide interface, promoting the accumulation of iron chlorides in this region, as confirmed by the presented SEM cross-sectional analysis.

The microstructural analysis indicates that in the presence of $PbCl_2$, the oxide scales formed on T22 appear to be less-adherent to the alloy surface, as compared with regions distant from $PbCl_2$. Areas close to the deposited $PbCl_2$ particles experienced severe delamination of the oxide layer after just 1 hour of exposure (see Fig. 7.11a). The buildup of metal chlorides at the metal/oxide interface has been previously documented for T22 exposed to high-temperature corrosion with $KCl(s)$, and has been linked to a significant reduction in oxide scale adhesion to the metal surface [82]. This detachment persisted in samples that were exposed for 24 hours in this study and is suggested to initiate a cyclic process in which a new oxide scale forms, thereby repeating the cycle. After 168 hours of exposure, the voids appeared as filled due to the continuous oxide formation within them. Once the oxide scale detaches, its continued growth generates stress, leading to buckling and subsequent cracking. These cracks allow O_2 and H_2O and HCl to diffuse rapidly as gases to the metal/oxide interface, facilitating the formation of a new oxide scale and rapid oxidation.

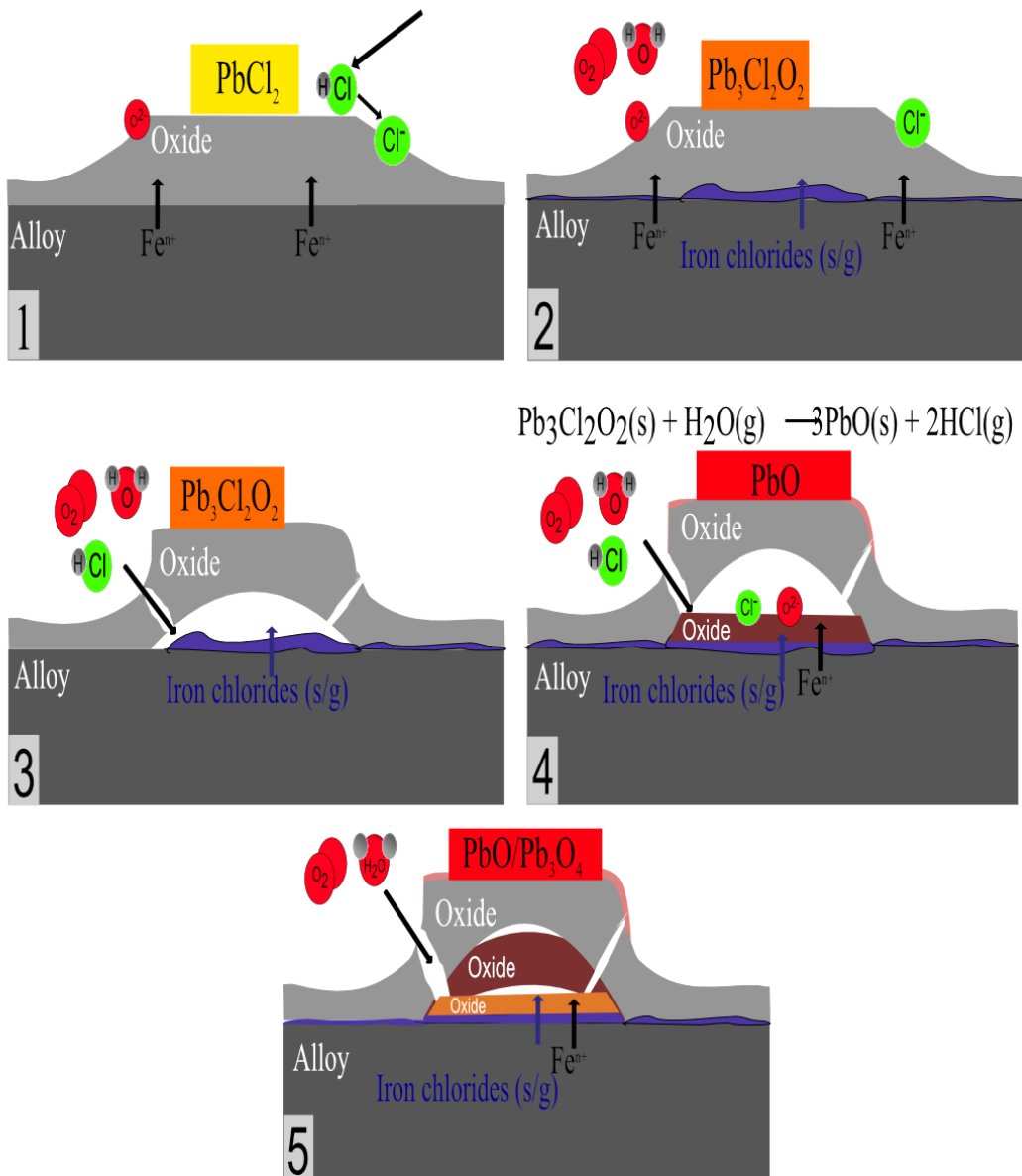
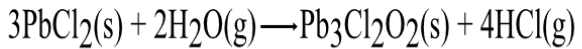


Fig. 7.15: Proposed corrosion mechanisms for T22 in the presence of PbCl_2 : (1) PbCl_2 reacts with the surrounding environment, leading to the formation of mendipite ($\text{Pb}_3\text{Cl}_2\text{O}_2$) and the release of HCl , which dissociates at the oxide surface to produce Cl^- ions. The Cl^- ions diffuse to the metal/oxide interface, where they form iron chlorides. (3) The formation of iron chlorides reduces the adhesion between the metal and the oxide scale, leading to delamination and crack formation. These macro defects promote the rapid diffusion of oxygen, HCl , and water vapor to the metal surface, thereby accelerating corrosion. (4) mendipite ($\text{Pb}_3\text{Cl}_2\text{O}_2$) reacts with the surrounding environment, releasing additional HCl that may dissociate at the oxide surface and promote further metal chloride formation. (5) The newly formed oxide scale exhibits similar poor adhesion due to the underlying iron chloride layer, resulting in repeated delamination and reformation of the oxide scale.

It is important to emphasize that the proposed delamination mechanism alone does not fully account for the accelerated corrosion of T22 in the presence of PbCl_2 . Fig. 7.16 compares the oxide scale thicknesses of samples exposed for 1 hour to three different environments: PbCl_2 , PbO , and reference. Fig. 7.16a shows a region deliberately selected away from areas with high PbCl_2 concentrations. In such regions, no evidence of delamination or crack formation was observed; instead, a dense multilayered oxide scale was present. This suggests that in these areas, oxide growth is primarily controlled by ion diffusion through the scale. However, when comparing the oxide thicknesses in these regions to those of samples exposed to PbO and the reference

environment (see Fig. 7.16), it is evident that oxidation progresses more rapidly in the presence of PbCl_2 . It has been proposed that Cl^- segregation along oxide grain boundaries enhances ion diffusion through the oxide, thereby accelerating corrosion [114]. However, this could not be confirmed in the present study. For a more detailed microstructural investigation, high-resolution analytical techniques, such as TEM or atom probe tomography, must be implemented.

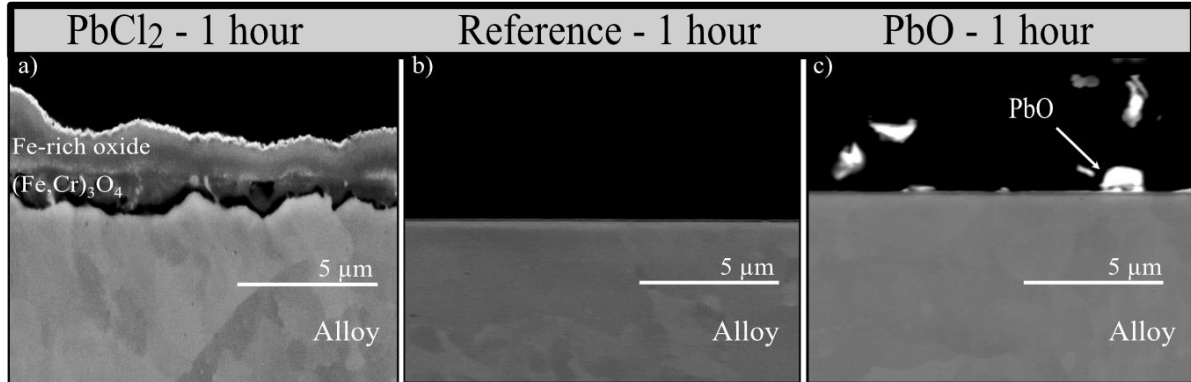


Fig. 7.16: Comparison of the alloy microstructures from the three different exposures carried out after 1 hour of exposure: (a) A region in which no delamination of the oxide scale was present after 1 hour of exposure in presence of PbCl_2 . The oxide scale is notable thicker, as compared to the reference sample (b) and sample exposed to PbO (c).

While it is argued that Cl plays a major role in accelerating the corrosion of PbCl_2 on low-alloyed steel under the present conditions, Pb does not appear to contribute to an increased corrosion rate. After 24 hours of exposure, the corroded surface displayed PbO , along with a Fe-Pb-O oxide layer at the top oxide scale near the initial PbCl_2 particles. In contrast, parallel exposures of T22 to PbO resulted in minimal corrosion, with the microstructure showing the development of a dense, slowly growing oxide layer. Additionally, magnetoplumbite ($\text{Fe}_{12}\text{PbO}_{19}$) was suggested to form on top of this oxide scale. Although magnetoplumbite was not identified in the XRD analysis of PbCl_2 -exposed samples, the atomic percentage from SEM/EDX analysis in these regions was similar to that of magnetoplumbite. However, due to the severe cracking and spallation of the oxide layer shown in the presence of PbCl_2 , it is assumed that the suggested protective properties of this oxide layer are compromised in samples exposed to PbCl_2 .

Lastly, PbCl_2 -induced corrosion is often associated with the formation of molten phases that accelerate degradation (see *Section 5.2*). However, no evidence of melt formation was observed in the present study.

7.4.3 Paper III- A framework for predicting superheater corrosion in waste-fired boilers: integrating kinetic simulations, oxide microstructure, and boiler operation

7.4.3.1 Deriving α -values from literature and DICTRA simulations

Table 7.3 presents a summary of the results obtained from the literature review and the simulations discussed in *Section 7.3*, Part I. The literature review encompassed a range of materials, including pure iron, low-alloy steel (T22 and Fe-2.25Cr), and stainless steel (SVM12) (see cited studies in Table 7.3 for chemical composition of the alloys). These materials were selected based on the availability of studies that provided measurable oxide grains, quantified oxidation kinetics (mass gain data), and exposure to varying chlorine loads at relevant temperatures, the three criteria mentioned in step 1 in *Section 7.3*. All the referred studies show parabolic kinetics (see cited studies

in Table 7.3 for further details), making the DICTRA simulation approach suitable. In Table 7.3, bolded K_p -values represent experimentally measured values, while the remaining K_p -values are derived from these through additional calculations. For the DICTRA simulated K_p -values, input parameters were extracted from the measurements of oxide scale thickness and grain size.

Across the studied temperature range, the simulated K_p -values show good agreement with the experimental data in terms of order of magnitude. However, minor deviations exist and are attributed to methodological differences. Specifically, K_p -values derived from mass gain data represent spatially averaged behavior across the sample surface, thus incorporating microstructural as well as compositional heterogeneities. In contrast, simulated K_p -values based on oxide thickness measurements by SEM are by default localized and may not fully reflect the surface-wide variability.

The activation energy for oxide grain boundary diffusion, expressed as the α -value, was also determined through simulations (see Table 7.3). This parameter reflects the relative reduction in activation energy for diffusion along grain boundaries compared to lattice diffusion, as discussed in *Section 6.6*. It should be noted that the DICTRA model incorporates the effects of alloying elements and environment (e.g., water vapour and the presence of chlorine) by adjusting the α -value, thereby accounting for their influence on grain boundary diffusion rates which is the primary diffusion path in the studied temperatures [82].

Representative α -values were obtained from laboratory-scale exposures performed in chlorine-containing environments (e.g., involving KCl and/or HCl), enabling assessment of their influence on corrosion behavior. Three scenarios based on chlorine-load were considered: chlorine-free (No Cl), intermediate chlorine load (Mid Cl), and high chlorine load (High Cl). These α -values are relative and derived from a comparative literature review. The High Cl condition was based on a laboratory study involving the deposition of KCl(s) and the presence of both KCl(g) and HCl(g) in the gas phase. The referred study demonstrated that the presence of KCl(g) significantly reduces the evaporation of the deposited KCl(s), thereby maintaining high Cl-load throughout the duration of the experiment. This interpretation is further supported by the consistent α -values observed for the Mid Cl condition at both 400 °C and 600 °C. At 400 °C, the reduced volatility of KCl(s) is attributed to the lower temperature, whereas at 600 °C, the introduction of KCl(g) similarly inhibits KCl(s) evaporation, maintaining a stable chlorine load.

The α -values reported for the Mid Cl condition at 500 °C should be interpreted with caution. Examination of the experimental setup in the study referred to revealed that only a fraction of initially deposited KCl(s) remained on the sample, and no residual KCl was observed post-exposure. Given the high volatility of KCl(s) at this temperature and under the specific atmospheric conditions, it is likely that the KCl(s) evaporated rapidly from the sample surface. This could account for the α -value being comparable to that observed under the No Cl condition at the same temperature, as both exposures were likely conducted for a long period of time in similar environments dominated ($O_2 + H_2O$).

*Table 7.3: Summary of the literature review for oxide growth kinetics in the temperature range of 400-600 °C. * is the measured grain size/thickness, ** pre-oxidation followed by exposure to KCl, and *** describes experimental where KCl is not expected to have remained on the sample for the whole duration due to evaporation.*

Source	Time	Environment	Material	Fe ₂ O ₃ *	Fe ₃ O ₄ *	Thickness	K _{p1}	K _{p2}	K _{p3}	Ref.	Case	α-value
	hours	O ₂ +		nm	nm	μm	mm ² /year	g ² /cm ⁴ /s	m/√s			
Input data 400 °C							Output data 400 °C					
Massgain	24	-	Fe	-	-	-	1.2E-03	8.5E-13	5.5E-09	[145]	-	-
DICTRA	24	-	Fe	150	300	4.5	1.5E-03	4.8E-12	1.5E-08	[145]	No Cl	0.37
Massgain	24	H ₂ O	Fe	-	-	-	2.4E-04	7.5E-13	6.0E-09	[145]	-	-
Massgain	168	H ₂ O	T22	-	-	-	1.6E-04	5.2E-13	5.0E-09	[146]	-	-
DICTRA	168	H ₂ O	T22	165	330	2.8	2.9E-04	9.3E-13	3.6E-09	[146]	No Cl	0.47
Massgain	168	H ₂ O + KCl(s)	T22	-	-	-	7.7E-04	2.5E-12	1.1E-08	[146]	-	-
Massgain	12	H ₂ O + KCl(s)	T22	-	-	-	2.6E-03	8.3E-12	2.0E-08	[116]	-	-
DICTRA	12	H ₂ O + KCl(s)	T22	190	230	4.6	3.2E-03	1.0E-11	2.2E-08	[116]	Mid Cl	0.36
DICTRA	12/168**	H ₂ O/H ₂ O + KCl(s)	T22	330	470	4/10.1	1.1E-03	3.4E-12	1.3E-08	[147]	Mid Cl	0.38
DICTRA	168	H ₂ O + KCl(s)	T22	330	380	9	8.7E-04	2.7E-12	1.2E-08	[146]	Mid Cl	0.37
Input data 500 °C							Input data 500 °C					
Massgain	24	-	Fe	-	-	-	2.2E-02	1.2E-08	2.8E-08	[145]	-	-
DICTRA	24	-	Fe	570	1000	15	1.7E-02	5.3E-11	5.1E-08	[145]	No Cl	0.37
Massgain	168	H ₂ O	T22	-	-	-	8.9E-04	2.8E-12	1.2E-08	[146]	-	-
DICTRA	168	H ₂ O	T22	330	830	12.8	1.8E-03	5.5E-12	1.6E-08	[146]	No Cl	0.46
Massgain	168	H ₂ O + KCl(s)	T22	-	-	-	1.1E-03	3.4E-12	1.3E-08	[146]	-	-
DICTRA	168	H ₂ O + KCl(s)	T22	330	590	17	3.1E-03	9.8E-12	2.2E-08	[146]	Mid Cl	0.43 ***
Input data 600 °C							Input data 600 °C					
Massgain	24	-	Fe	-	-	-	2.3E-01	9.4E-13	8.8E-08	[145]	-	-
DICTRA	24	-	Fe	770	2500	34	8.7E-02	2.7E-10	1.2E-07	[145]	No Cl	0.37
Massgain	168	-	Fe2.25Cr	-	-	-	1.6 E-02	5.0E-11	4.9E-08	[148]	-	-
DICTRA	168	-	Fe2.25Cr	1500	2770	50	2.7 E-02	8.5 E-11	6.4 E-08	[148]	No Cl	0.40
DICTRA	168	H ₂ O + KCl(s)+KCl(g)	SVM12	560	1170	97	1.0 E-01	3.2 E-10	1.3 E-07	[102]	Mid Cl	0.38
DICTRA	168	H ₂ O + KCl(s)+KCl(g) +HCl	SVM12	1180	2170	120	1.5 E-01	4.9 E-10	1.5 E-07	[102]	High Cl	0.34

Based on this study, three chlorine-loading scenarios were identified for the prediction of the low-alloyed superheater tube exposed in the waste fired boiler, with corresponding α-values of 0.32 for High Cl, 0.36 for Mid Cl, and 0.46 for No Cl.

7.4.3.2 Field sample exposed to P14 Händelöverket

As the case study focused on a sample exposed in the P14 boiler at Händelöverket, the microstructural analysis will be limited for the sample exposed to this boiler. Fig. 7.17 shows a cross-sectional image of the low-alloyed steel sample (10CrMo4-5), showing a dense and adherent oxide layer at the metal–oxide interface, (see Fig. 7.17) SEM/EDX point analysis of the innermost oxide layer identified it as predominantly iron oxide with trace amounts of Cr and Mo. Electron backscatter diffraction (EBSD) analysis confirmed this oxide phase to be magnetite (Fe_3O_4). The Average oxide grain size in this layer was approximately 200–400 nm.

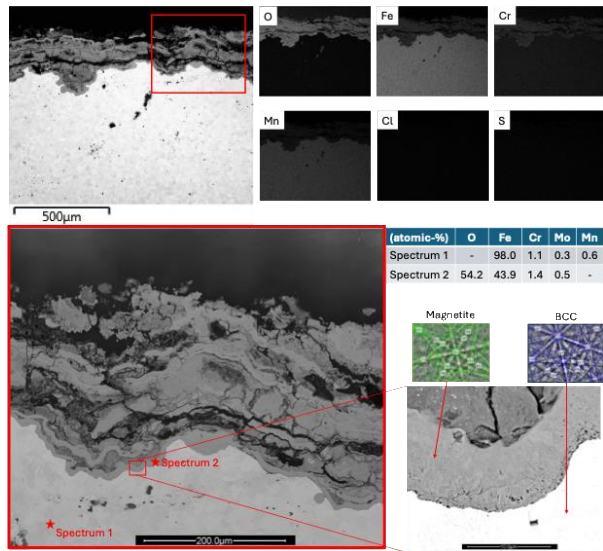


Fig. 7.17: Microstructural analysis of 10CrMo4-5 exposed for 4.1 years in P14 Händelöverket.

7.4.3.3 Predicted material loss vs. Measured material loss

The α -values derived from DICTRA simulations, corresponding to the three chlorine-loading scenarios, were combined with experimentally measured oxide grain sizes obtained from the sample exposed in the P14 boiler at Händelöverket. These parameters served as inputs for simulating the parabolic rate constants (K_p) at 412 °C, representing the material temperature of the exposed sample. Notably, the grain size of hematite was fixed at 100 nm for all simulations, as no distinct hematite layer was identified on top of the inner oxide scale under the current SEM resolution. Given that 100 nm represents the lower limit of allowable grain size for DICTRA input, this value was uniformly applied across all chlorine conditions. The resulting K_p -values for each scenario are presented in Table 7.4. These values were subsequently used to estimate the predicted material loss of the boiler-exposed sample, under the assumption that oxide growth follows parabolic kinetics. For this calculation, Equation (6) was employed, with the integration constant C=0.

Table 7.4: Summary of simulated K_p values, derived from simulations incorporating oxide grain size measurements of magnetite from the sample exposed to the P14 Händelöverket boiler, along with α -values obtained from laboratory simulations. The hematite grain size was fixed at 100 nm, while the α -values varied for different chlorine load scenarios.

Source	Material	Material temperature	Fe_2O_3 *	Fe_3O_4 *	K_{p1}	K_{p2}	K_{p3}	Case	α -value
		°C	nm	nm	mm^2/year	$\text{g}^2/\text{cm}^4/\text{s}$	$\text{m}/\sqrt{\text{s}}$		
DICTRA	10CrMo4-5	412	100	360	3.1E-02	9.6E-11	6.9E-08	High Cl	0.32
DICTRA	10CrMo4-5	412	100	360	4.8E-03	1.5E-11	2.7E-08	Mid Cl	0.36
DICTRA	10CrMo4-5	412	100	360	1.8E-04	5.5E-13	5.2E-09	No Cl	0.46

Fig. 7.18a presents the experimentally measured material loss from the Händelöverket boiler, based on a total of nine data points. The final data point, shown in red, represents an extrapolated value corresponding to the full exposure duration of 4.1 years, at which point the total material loss was estimated to be approximately 3.4 mm. Fig. 7.18b shows simulated material loss under varying chlorine-loading scenarios. Even under the high chlorine-load condition, the predicted material loss after 4.1 years substantially underestimates the extrapolated value derived from measured material loss. Analysis of the measured data reveals a linear trend in material loss over time (Fig. 7.18a). However, microstructural examinations indicate that the innermost oxide layer is dense and well-adherent, which contradicts the assumption of linear oxidation kinetics. These observations, instead, support a diffusion-controlled mechanism, consistent with parabolic growth behavior, where transport of charged species through the oxide scale is the rate-limiting step.

To account for the observed deviation between measured and predicted material loss, it is proposed that the predictive model needs to be refined to include a parameter representing the re-initiation of oxidation processes due to delamination of the oxide scale, herein referred to as *cycles*. These re-initiation events may be triggered by various factors, including thermal fluctuations, increasing oxide thickness, or by Cl as discussed in *Section 5.1.3*. As an initial estimate, the frequency of thermal cycling was employed to approximate the number of such oxidation restarts. Operational data from the Händelöverket boiler (see Appended Paper III) were evaluated to identify periods during which the surface temperature dropped below 200 °C, a threshold considered indicative of a cooling cycle. This analysis revealed a total of 34 thermal cycles over the monitored exposure period. To visualize the effect of cycles on the overall material loss, 10, 20 and 40 cycles were simulated for the High Cl case (Fig. 7.18a). Nonetheless, even when the number of cycles was conservatively increased to 40 in the simulations, the predicted material loss was limited to approximately 2.25 mm, substantially lower than the extrapolated value of ~3.4 mm based on experimental measurements.

This discrepancy suggests either that the actual number of oxidation restarts/cycles is substantially greater than 40, or that the α -value derived from laboratory-scale exposures in high-chlorine environments underestimates the ion diffusion rate in field conditions. To explore this, the number of oxidation cycles in the high Cl scenario was adjusted in the model (see Fig. 7.18d). When the number of cycles increased to 87, the predicted material loss aligned closely with the experimental value of 3.4 mm. The requirement for such a high number of cycles exceeds the number of thermal cycles. This suggests that oxidation restarts are not solely driven by thermal cycling. This interpretation is further supported by laboratory experiments (Fig. 5.1), where oxidation restarts were observed even under isothermal conditions, indicating that other factors may contribute to repeated oxide-scale breakdown and regrowth in service. However, further investigation is required to fully understand these contributing mechanisms. Nevertheless, repeated re-initiation of oxide growth may contribute to the apparent linear trend observed in the measured material loss. This interpretation is further supported by the presence of a dense and well-adherent oxide scale at the metal/oxide interface, which is characteristic of diffusion-controlled oxidation processes. Therefore, despite the apparent linear trend in material loss, the corrosion process is more likely governed by parabolic kinetics, consistent with diffusion-controlled oxide growth.

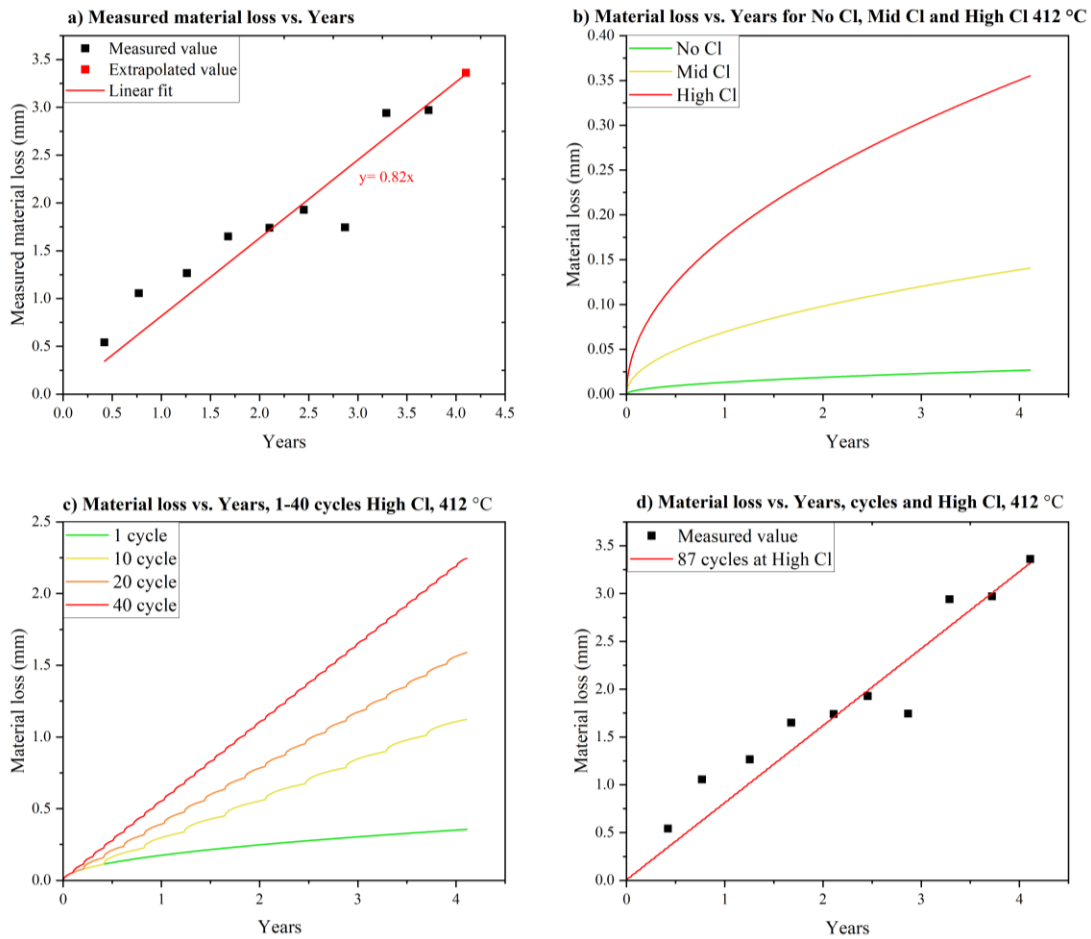


Fig 7.18: (a) Measured material loss for the 10CrMo4-5 sample exposed in the P14 boiler at Händelöverket; the red data point represents the extrapolated material loss at the time of sample extraction; (b) Simulated material loss as a function of Cl; (c) Predicted material loss incorporating oxidation restarts (cycles), varying from 1 to 40; (d) Comparison of measured material loss and predicted material loss incorporating 87 oxidation cycles.

8. Part II: Potential corrosion challenges in chemical looping combustion of biomass

8.1 Background

Chemical looping combustion (CLC) is often promoted for its high CO₂ capture rate and the low energy penalty associated with the separation of CO₂ from the flue gas [149, 150]. Research on CLC has primarily focused on improving these parameters by optimizing process parameters, such as development of appropriate oxygen carriers and improving the conversion rate of volatile species, among others [76, 150]. These are, of course, important aspects to consider when exploring both financial and environmentally sustainable approaches to achieving negative CO₂ emissions in the heat and electricity production sector. However, another distinct advantage of CLC is its potential to enhance the steam data associated with the combustion of biomass and waste-derived fuels. This advantage is even more prominent when compared with other carbon capture technologies considered for heat and electricity production (see *Section 2.2.3*), which not only impose a high energy penalty for CO₂ separation but also offer little to no opportunity to mitigate the corrosion challenges associated with combusting solid biomass and waste. This is because the superheaters in these technologies are placed in the corrosive flue gas stream. In contrast, the CLC two-reactor configuration minimizes the levels of corrosive species in the air reactor (AR), making it an ideal region for final steam heating. This setup could enhance steam performance with biomass and waste fuels, potentially achieving levels comparable to those in advanced coal-fired boilers. To maximize electrical efficiency in CLC and ensure long-term operational reliability, understanding high-temperature corrosion of superheaters and heat exchangers is important in both the AR and FR. Different corrosion challenges can be expected from the two reactors, as their environments are significantly different.

8.1.1 Corrosion in the fuel reactor

Online alkali ionization detector measurements performed in a pilot-scale CLC of biomass with low sulfur content have suggested that alkali release in the FR is dominated by the sublimation of alkali chlorides, such as KCl(s) to KCl(g), or the decomposition of alkali salts, such as K₂CO₃(s) to KOH(g) [37]. From studies carried out in conventional biomass-fired boiler environments, it is clear that these elements lead to severe corrosion [151-153]. However, several key differences set the FR environment apart from that of conventional biomass- and waste-fired boilers. Since fuel conversion in CLC is facilitated by oxygen carriers rather than by direct contact with air, the flue gas is less diluted with N₂, resulting in an environment that is enriched for CO₂ and H₂O upon complete fuel conversion. In addition, given that many oxygen carriers support fuel conversion without releasing molecular O₂, the FR is anticipated to have a lower oxygen concentration compared with conventional biomass-fired boilers where excess oxygen is supplied by air.

Although there are no published studies on the corrosion of heat exchange materials in the FR at pilot scale, there have been attempts to explore this issue on the laboratory scale. Eriksson et al. have shown that at 450 °C, low-alloyed steel starts to corrode when exposed to an environment that aims to simulate the conditions in the FR of a unit designed for CLC of biomass (50% H₂O/50% CO₂) [154]. In particular, the corrosion attack became significant when KCl(s), HCl(g) and minor

oxygen were introduced, and at 550 °C the corrosion attack became even more severe. It was proposed that these corrosion attacks occurred primarily due to the formation of metal chlorides, partial melt formation between the corrosion products, and the release of chlorine gas via the active oxidation mechanism. Nevertheless, the emerging oxide scales are notably dense and adherent, indicating Cl⁻ ion diffusion-controlled growth rather than gas-controlled diffusion growth. Notably, no significant corrosion was reported for the austenitic stainless steel. However, that study did not present microstructural analyses of the oxide scales or provide a detailed discussion of this alloy type, making it difficult to assess the features of the formed oxide scale and corrosion products for these steel types in this environment. It is important to note that this laboratory-based study is a simplified representation of large-scale operation conditions. For instance, in a CLC system, unreacted fuel gases may occur as a result of suboptimal oxygen carrier-fuel interaction, limitations in reaction kinetics, or fuel bypassing, particularly when utilizing solid fuels [155]. In such cases, it has been suggested that implementing oxy-polishing steps downstream may be necessary for full fuel conversion, which could result in some parts of the FR side having increased oxygen concentrations. This could accelerate chromate formation and rapid degradation of the primary protective Cr₂O₃/(Fe,Cr)₂O₃ oxide scale, in the presence of alkali (Reaction 9).

The environment becomes even more complex when utilizing waste-derived fuels. Waste-derived fuels are highly heterogeneous, and may contain relatively high concentrations of alkali chlorides, HCl(g) and heavy chlorides such as PbCl₂, which have been shown to accelerate corrosion in conventional waste-fired boilers [18]. The corrosion challenges associated with using waste-derived fuels in the FR side remain unclear, as no corrosion studies have been conducted in this specific setup. However, from the results presented in **Paper II** of Part I of this thesis, it appears that the formation of metal chlorides and their impacts on oxide scale spallation result in severe corrosion of low-alloyed steels that are exposed to PbCl₂ in an environment relevant to conventional biomass-fired boilers. Furthermore, as shown in Reaction 14, the release of HCl from PbCl₂ appears to be influenced by the partial pressure of water vapor. Given the expected high concentration of water vapor in the FR, both the release of HCl and the formation of metal chlorides are likely to present challenges in the FR during the combustion of waste. Furthermore, as presented in Reaction 13, stainless steel is susceptible to chromate formation in the presence of heavy metal chlorides and H₂O(g), such as PbCl₂. It is important to note that this is a relatively new area of study, and limited research has been conducted on this topic. There is significant potential for further investigations aimed at understanding the corrosion mechanisms in this context, although this falls outside the scope of the present thesis.

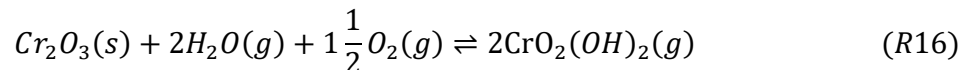
8.1.2 Corrosion in the air reactor

The anticipated environment of the AR has certain advantages in relation to the placement of the final heating of the steam, i.e., superheaters, on this side of a CLC unit. The oxidation of the oxygen carrier in the AR (see Reaction 2) is exothermic, generating substantial heat. Furthermore, in an ideal scenario, referred to in this thesis as the *Clean scenario*, the AR is expected to maintain an atmosphere that is primarily composed of oxygen-depleted air, regardless of the fuel type used, as it remains separate from the fuel conversion process occurring in the FR. This makes positioning the superheater tubes in this section of the CLC unit optimal from a corrosion perspective. It is important to note that the *Clean scenario* assumes minimal transport and release of corrosive species from the FR to the AR. However, the presence of alkali species in the air reactor (AR) has been identified during combustion of biomass [79]. This phenomenon, referred to in this thesis as

the *Alkali-slip scenario*, could introduce additional corrosion challenges that were not initially anticipated. The following section will discuss corrosion issues that may arise in both the *Clean* and *Alkali-slip scenarios*.

8.1.2.1 Clean scenario

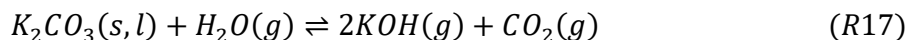
In the *Clean scenario*, the environment in the AR should in theory be only mildly corrosive as the gas composition mainly comprises oxygen-depleted air. Austenitic stainless steels and Ni-based alloys achieve good protective properties due to their abilities to form $(\text{FeCr})_2\text{O}_3/\text{Cr}_2\text{O}_3$ in mildly corrosive environments. Nevertheless, in the presence of water vapor and at high temperatures, volatile Cr species such as $\text{CrO}_2(\text{OH})_2$ are formed by the reaction of Cr_2O_3 , as described by Reaction 16:



This can result in the rapid depletion of Cr in the oxide, potentially leading to breakaway corrosion. The rate of Cr evaporation is strongly influenced by the temperature, water vapor content, and gas flow rate. Studies have indicated that austenitic stainless steels undergo breakaway corrosion under conditions relevant to CLC superheater applications in the AR ($600^\circ\text{--}900^\circ\text{C}$) when exposed to air that contains 3% H_2O [55–59]. The ability to resist breakaway corrosion under humid conditions has been associated with increased Cr and Ni contents. For instance, Pettersson et al. investigated austenitic stainless steels with Ni contents ranging from 14 wt.% to 43 wt.% at 700°C in air, with water vapor concentrations ranging from 0% to 62% H_2O . The results showed a strong correlation between higher Ni content and improved resistance to breakaway corrosion, particularly under humid conditions [156].

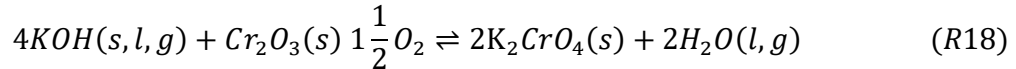
8.1.2.2 Akali-slip scenario

The *Clean scenario* should be considered as an ideal situation. Work carried out by Gogolev suggests that this might not always reflect actual operational conditions [36]. In his work, Gogolev measured gaseous alkali release, which accounted for 0.1%–7.0% of the fuel alkalis from several different pilot-scale CLC units burning biomass. Although the origin of the alkali in the AR is not yet fully understood, it has been proposed to arise from carryover from the FR through unreacted char, unconverted fuel, or absorption of alkali to the oxygen carriers. Furthermore, in terms of the specific alkali composition, it has been suggested that most of the alkali chlorides, such as KCl , are likely to be released rapidly in the FR. This is further supported by measurements carried out by Gogolev et al. where only traces of KCl were detected in the fly ash in the AR of a 60-kW CLC pilot plant combusting biomass [157]. Thus, it appears that most of the alkali in the char conversion phase consists of K_2CO_3 when combusting low-sulfur-containing biomass. In the case of uncovered char being transported to the AR, the increased temperature in the AR and presence of water vapor from the air may promote the decomposition of K_2CO_3 , leading to the release of gaseous $\text{KOH}(g)$ according to the following reaction:



KOH -induced corrosion at high temperatures has received less attention than alkali chloride-induced corrosion. Blomberg et al. have suggested that $\text{KOH}(g)$ plays a significant role in fireside corrosion of heat transfer materials in conventional biomass-fired boilers [38–40]. Blomberg et al. conducted studies on pure Cr_2O_3 at temperatures ranging from 25°C to 800°C , demonstrating that

KOH readily reacts with Cr₂O₃ at temperatures as low as 200 °C, leading to the formation of K₂CrO₄, as described by Reaction 18 [20]:



However, this study was conducted on pure chromia, making it challenging to predict the corrosion effects of chromate formation on chromia-forming alloys, such as stainless steel and Ni-based alloys. For these materials, the alloy substrate provides a reservoir of Cr that can diffuse to the corrosion front, replenish the chromia scale, and delay breakaway corrosion in a satisfactory manner. Nonetheless, a sudden slip of alkali-containing compounds from the FR could alter the environment in the AR, making it potentially more corrosive than initially predicted.

8.1.3 Material selection for superheater applications in CLC

To meet the superheated steam conditions of state-of-the-art, coal-fired boilers, an important benchmark for CLC of biomass and waste, superheater tubes material temperatures are expected to reach around 650 °C. Research aimed at further increasing the steam temperature, potentially to >700 °C, makes a material temperature of up to 700 °C a reasonable target in the AR of a CLC unit [105]. In mildly corrosive coal-fired boilers, superheater tubes are often made out of high-strength ferritic steels due to their low cost, good creep strength, and thermal fatigue resistance. However, ferritic steel becomes limited in terms of corrosion resistance and creep strength at temperatures above 600 °C. Therefore, high-alloyed steels, such as austenitic stainless steels or nickel-based alloys that offer good creep strength and corrosion resistance, are likely to be considered for superheaters in CLC when pushing the superheated steam temperature towards 700 °C [158]. However, since the primary protection for austenitic stainless steel and Ni-based alloys relies on the formation and stability of a Cr-rich oxide scale such as Cr₂O₃/(Fe,Cr)₂O₃ over extended operational periods, it is reasonable to argue that the environment in the AR could lead to sudden breakaway corrosion (see Reaction 16 and Reaction 18). Thus, alternative materials should also be evaluated.

FeCrAl alloys are generally appreciated for their protective properties at temperatures >900 °C, owing to their ability to form a protective α-Al₂O₃ oxide scale. At lower temperatures, the formation of transient alumina is observed with an increase in Cr content, making the material more-susceptible to Cr-depleting corrosion mechanisms [101, 106]. For instance, at 600 °C, alkali promotes breakaway corrosion through alkali-chromate formation, leading to breakaway corrosion of FeCrAl alloys [106]. However, studies carried out by Josefsson et al. showed that the concentrations of Fe and Cr in the Al₂O₃ oxide scale formed on a commercial ferritic FeCrAl alloy were significantly lower at 700 °C than at 500 °C or 600 °C in an oxidizing environment [159]. This suggests that the protective properties at 700 °C should be improved for this alloy type when exposed to alkali or water vapor. This is further supported by corrosion studies of the FeCrAl alloy Kanthal EF101 conducted at 700 °C, which have demonstrated low rates of Cr-evaporation compared to conventional stainless steels, when exposed to air with 3% H₂O [160].

Not only does temperature have an important impact on the protective properties of the primary protective oxide scale of FeCrAl, but so does the addition of minor alloying elements. Eklund et al. demonstrated that the addition of 2 wt.% Si to an FeCrAl model alloy prevented breakaway corrosion when exposed to K₂CO₃ in 5% O₂ and 95% N₂ at 600 °C for up to 2000 hours [161]. The results of research carried out by Asokan et al. on FeCrAl alloys at 600 °C suggest that Si enhances

Al activity in the alloy substrate, significantly increasing the Al content of the primary protective oxide scale [162]. Sand et al. observed that the addition of 1-2 wt.% silicon to FeCrAl alloys significantly reduced chromium evaporation at 800 °C in humid air [163].

8.2 Experimental overview- Part II

The aim of Part II of this thesis was to improve our understanding of the potential corrosion challenges related to superheater positioning in the AR side of a CLC unit combusting biomass or waste. This is important for choosing the optimal material, in terms of corrosion protection, for this application. An overview of the experimental approach adopted is shown in Fig. 8.1. As the literature on corrosion studies is scarce, it was vital to determine the environment anticipated in the AR of a CLC unit with biomass. The literature reviewed in *Section 8.1* provided the necessary foundation for developing a well-controlled laboratory setup, enabling the study of two relevant scenarios in the AR, termed the *Clean scenario* and *Alkali-slip scenario*. The results will be presented in the context of the following research questions:

- ❖ What material is suitable for superheater application in the AR side of a CLC unit combusting biomass?
- ❖ How does a significant alkali load affect the corrosion rates of the different materials and consequently, their suitability for use in the CLC unit?

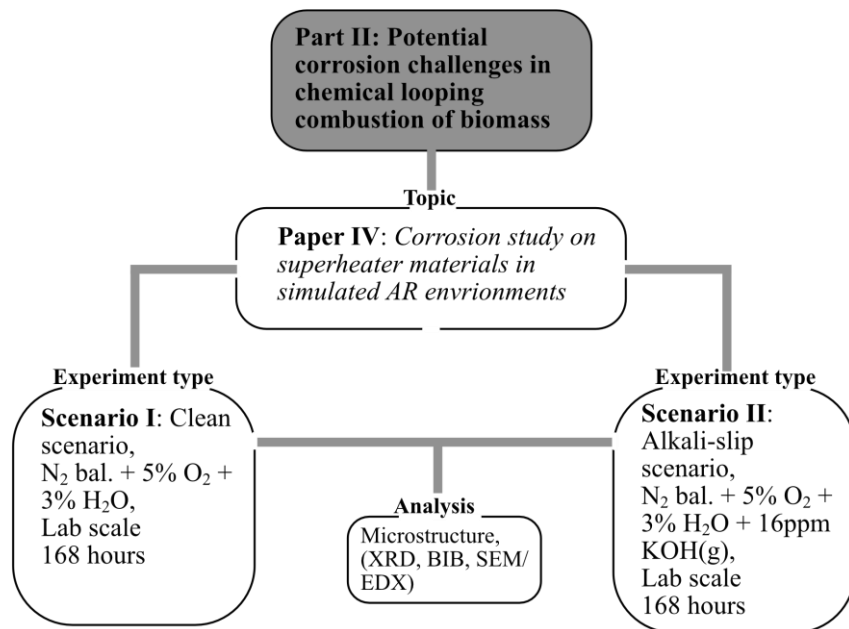


Fig. 8.1: Flowchart illustrating the approach used for the study conducted in Part II of this thesis.

Table 8.1 shows the different alloys exposed and their chemical compositions, expressed in wt.%. The alloys were supplied by Alleima AB and Kanthal AB.

Table 8.1: Chemical compositions of the different alloys used in Paper IV.

Name	Alloy type	Wt.%												Supplier
		Fe	Cr	Al	Ni	Mn	Si	Mo	Co	Cu	W	Nb	Minor elements (< 0.5)	
Sanicro® 25	Austenitic stainless steel	Bal.	22.5	-	25	0.5	-	-	-	3	3.6	0.5	C, N, S	Alleima AB
AISI 310H	Austenitic stainless steel	Bal.	24.5	-	21	1.5	0.8	-	-	-	-	0.7	C, S	Alleima AB
AISI 347H	Austenitic stainless steel	Bal.	17.5	-	11	1.8	-	-	-	-	-	-	C, S, Si	Alleima AB
Kanthal® EF101	FeCrAl	Bal.	12.4	3.7	-	-	1.3	-	-	-	-	-	C, Mn, RE*	Kanthal AB
Sanicro® 63x59	Ni-based	11.1	22.1	-	Bal.	-	-	4	-	-	-	-	C, Al, Si, Ti, Mn	Alleima AB
Sanicro® 625	Ni-based	4	21.5	-	Bal.	-	-	8.7	-	-	-	3.5	C, P, S, Si, Mn	Alleima AB

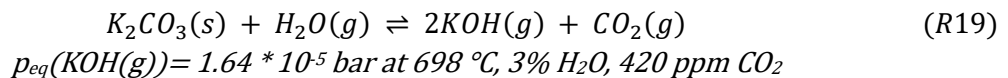
* Reactive element.

8.3 Experimental: Paper IV

Prior to exposure, the samples were polished and cleaned following the procedure outlined in the first part of *Section 7.2*.

An illustration of the setup for the corrosion tests is shown in Fig. 8.2. The exposures were performed using a horizontal tube furnace with a sintered alumina tube with inner diameter of 40 mm. Two different corrosion tests were carried out. In the first corrosion test, the samples were subjected to a gas composed of 5% O₂ + 3% H₂O + N₂ bal. at 700 °C for 168 hours (see Fig. 8.2a). Three samples were placed in parallel on an alumina sample holder for each corrosion test. The gas flow was set at 3 cm/s and controlled using the MesaLabs Bios DryCal Definer 220 Primary Flow calibrator. The humidity of the gas was established by coupling a water bath set at 24 °C, corresponding to 3% H₂O, to the gas stream. Water vapor was introduced to the dry gas through a Nafion membrane. The humidity of the gas was measured using the Mitchell Instruments Optidew Vision™ chilled mirror humidity sensor, prior to entering the horizontal tube furnace.

In the second corrosion test, the samples were exposed at 700 °C under continuous KOH(g) in a 5% O₂ + 3% H₂O + N₂ bal. environment for a period of 168 hours. Continuous KOH(g) exposure was achieved by placing an alumina boat containing K₂CO₃(s) in front of the subjected samples at 698°C (see Fig 8.2b). In this environment, K₂CO₃(s) reacts with the water vapor to form KOH(g) according to the following reaction:



The equilibrium pressure of KOH(g) was calculated using FactSage 7.1 and the FactPS database. To verify the concentration of KOH(g) in the gas stream, the mass of K₂CO₃ in the alumina boat was measured before and after each exposure. Prior to measurement, the K₂CO₃-loaded boat was heated in a furnace at >100 °C overnight, to remove any residual moisture. It was then stored in a

desiccator containing SICAPENT as desiccant. Once cooled to room temperature, the boat was weighed and then placed in the horizontal tube furnace for corrosion testing. After exposure, the sample was cooled once again in the same desiccator and weighed once it had reached room temperature. The change in mass, along with the temperature, gas flow rate (1,000 mL/min), and the ideal gas law were used to calculate the average KOH(g) concentration, which was found to be 16 ± 9 ppm (range, 6–25 ppm). This result aligns well with the equilibrium vapor pressure of KOH(g) at 698 °C, as described by Reaction 19.

By positioning the K₂CO₃(s)-containing alumina boat upstream at a temperature lower than that at the positions of the samples, condensation of KOH(g) on the samples is prevented. The temperature of the K₂CO₃ boat and the positions of the exposed samples were individually controlled prior to each exposure.

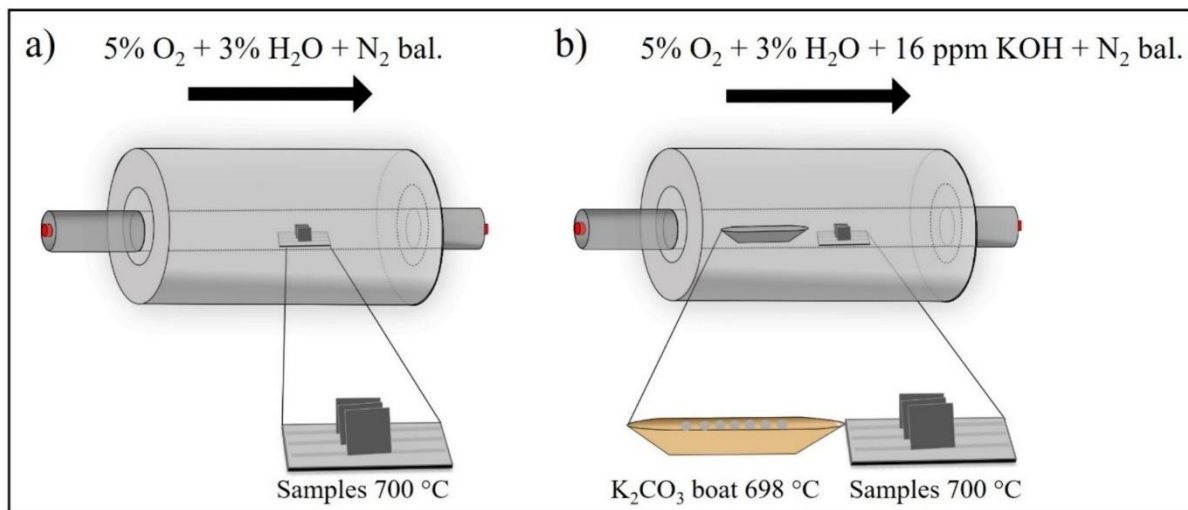


Fig. 8.2: Illustration of the furnace set-up and exposure conditions: a) exposure without KOH(g); b) exposure with 16 ppm KOH.

To verify that condensation of alkali at the position of the sample coupons was minimal, three gold coupons (15.0×15.0×0.3 mm) were placed at 700 °C in the same position used for the sample coupons, downstream of the K₂CO₃-containing alumina boat (which was situated at a position with temperature of 698 °C). The selected gas composition for this exposure was 5% O₂ + 3% H₂O + N₂ bal., with 16 ppm KOH(g) and an exposure time of 168 hours. The mass gain analysis from this test indicated negligible condensation of KOH(g) on the sample surface (see Fig. 8.3). Notably, all samples exhibited a slight negative mass change (within 5 µg/cm²). This minor decrease may be attributed to residual moisture on the sample or to measurement uncertainties within the microscale balance's margin of error.

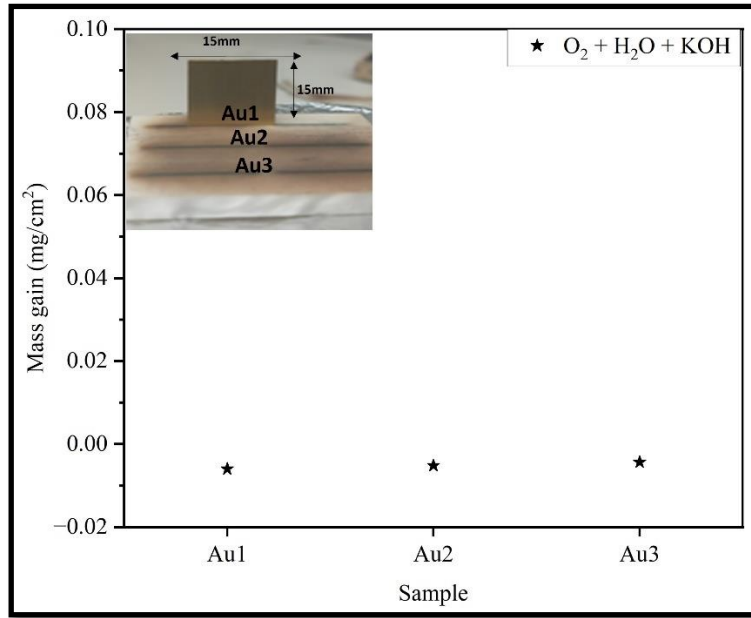


Fig. 8.3: Assessment of mass gains of gold coupons to predict the rate of alkali condensation on samples exposed in the setup described in Fig. 4.2b. This test suggests that minimal condensation of alkali occurs. The negative values observed for each sample are potentially due to either residual moisture on the sample or measurement uncertainties within the microscale balance's margin of error.

Two exposures of the selected alloys were performed for each corrosion test. The samples' position was altered on the alumina sample holder for each exposure (i.e., alternating middle and side positions), so as to register possible local effects. The furnace was flushed at 900 °C overnight without the alumina boat and samples prior to the exposure. After the exposure, the samples were stored in a desiccator, using SICAPENT as desiccant. Upon cooling, the mass gain of the exposed samples was recorded using a Sartorius balance with microgram resolution.

In this study, cross-sectional BIB samples were prepared for SEM/EDX analysis. Before milling, a thin silica wafer was attached to the exposed surface of each sample and left to dry overnight. The samples were then sectioned and polished to a 0.5 µm surface finish using the Leica EM TXP instrument, operated at low speed and without lubricant. Cross-sectional BIB milling was performed using the instrument and parameters detailed in *Section 6.2*.

8.4 Results & discussion: Paper IV

The results are divided into two sections, categorized according to the primary protective oxide scale that is formed. The first section focuses on chromia-forming alloys, including austenitic stainless steels and Ni-based alloys. The second section addresses the alumina-forming alloy, represented by the FeCrAl alloy EF101.

8.4.1 Chromia-forming alloys

8.4.1.1 Mass gain

When comparing the mass gains from the two exposures it becomes evident that the introduction of KOH(g) significantly increases the mass gain for all types of chromia-forming alloys (Fig. 8.4a). The mass gain is argued to be the result of corrosion, as the gold sample tests described in the experimental section indicated no condensation of KOH(g) on the samples. Regarding the mass gain from the *Clean scenario*, i.e., exposure to 5% O₂ and 3% H₂O, the majority of the alloys

showed a mass gain of roughly 0.01 mg/cm^2 , with the exception of 347H, indicating that no breakaway corrosion had occurred.

The 347H sample showed significant mass gain, indicating severe corrosion even in the *Clean scenario*. Another important observation was that this material demonstrated poor resistance to thermal cycling. This was evident upon removing the samples from the furnace. Within seconds after removal, significant spallation of the oxide scale was observed. Similar spallation was observed on the sample exposed to KOH(g) (see Fig. 8.4b). One of the important criteria for an oxide scale to be defined as protective is good adhesion to the substrate. This since the oxide scale functions as a protective barrier towards the environment and the substrate, which slows down the corrosion and degradation rate of the alloy substrate. In power plants, planned maintenance is common and can be expected to occur several times per year. Thus, thermal cycling is expected. If a severe spallation of the oxide scale occurs during cooling, the surface of the substrate will become exposed to the atmosphere that may lead to rapid corrosion upon re-start, potentially resulting in severe material loss.

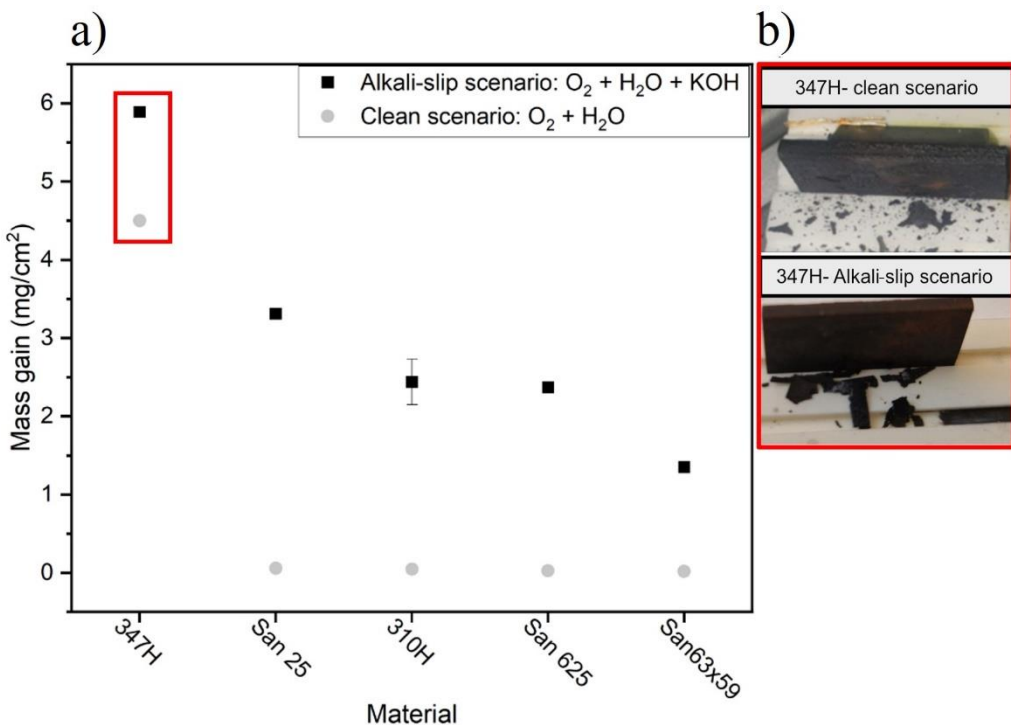


Fig. 8.4: a) Mass gains for the chromia-forming alloys exposed to the Clean scenario and Alkali-slip scenario. b) Photographs of 347H in both environments, taken seconds after removal from the tube furnace.

8.4.1.2 Microstructural analysis

Fig. 8.5, a and b show a BIB-milled SEM/EDX cross-sectional image of 347H exposed in the *Clean scenario* and *Alkali-slip scenario*, respectively. The oxide microstructures were similar in both scenarios. Therefore, the discussion will focus on the results from the sample exposed to the *Clean scenario*, though similar conclusions can be made for the case with the presence of KOH(g). Traces of a Fe-rich oxide growing on top of an inward-growing oxide scale were noted, indicating that the alloy had transitioned to the secondary protective regime (see Fig. 8.5c). Underneath this, an Fe,Cr-rich, inward-growing oxide scale was detected, followed by a thick internal oxidation zone. The depth of the internal oxidation zone was marginally greater when the alloy was exposed to KOH(g) (see Fig. 8.5, a and b). Internal oxidation is generally described as occurring when the local partial

pressure of oxygen and the activities of alloying elements reach levels that promote the selective oxidation of specific elements [84]. Unlike a fully protective inward- or outward-growing oxide scale, the internal oxidation zone forms a discontinuous layer of dispersed oxide precipitates, leaving behind an alloy matrix that is enriched in elements that are not fully oxidized. In the case of 347H, selective oxidation resulted in an internal oxidation zone that was composed of Fe and Cr oxides, while Ni and Fe remained in the metal substrate, as identified by SEM/EDX analysis (see Fig 8.5d). Studies have suggested that the network of interfaces between the oxide and metal within the internal oxidation zone facilitate the rapid transport of ions, potentially accelerating corrosion and leading to void formation that could cause spallation [164]. Research carried out by Persdotter et al. has suggested that the resistance towards internal oxidation is highly dependent upon alloying elements such as Cr and Ni for FeCrNi alloys [165]. Considering the relatively low concentrations of these alloy elements in 347H, as compared to the other chromia-forming alloys, it is possible that 347H lacks sufficient Cr at the given temperature and environmental conditions to prevent rapid breakaway corrosion, internal oxidation and the formation of a continuous healing layer. These factors collectively result in the alloy's limited corrosion resistances over the evaluated exposure period.

Stainless steel

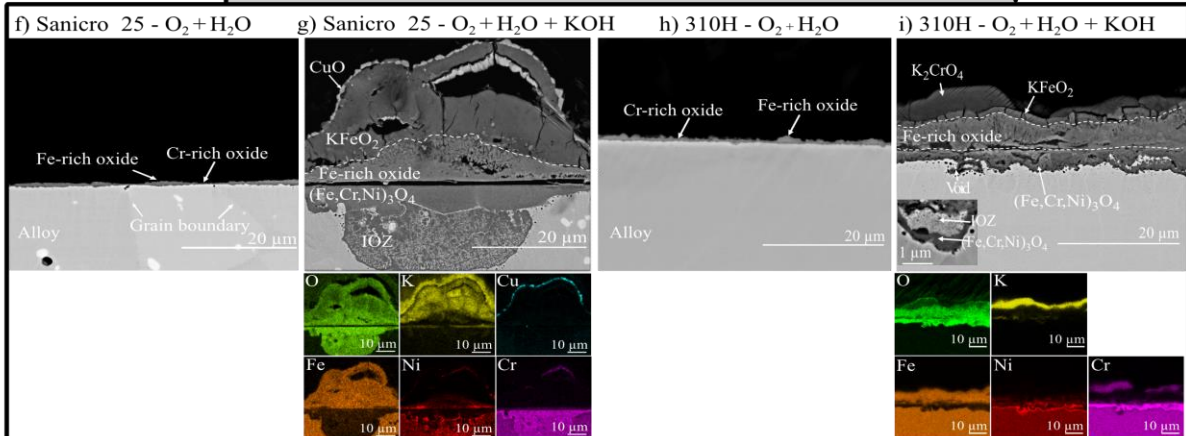
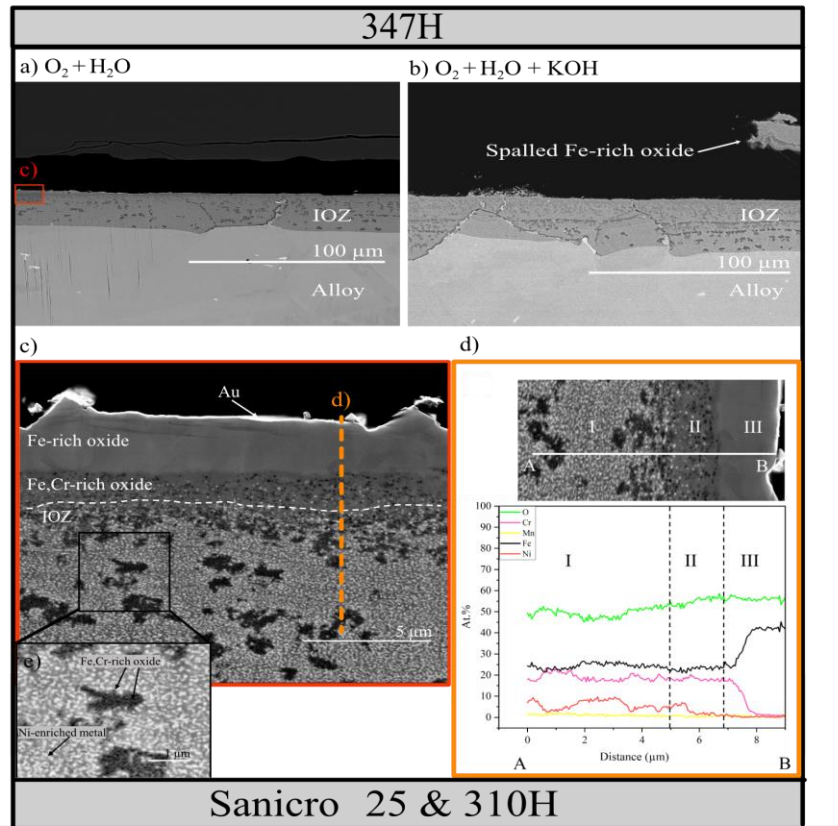
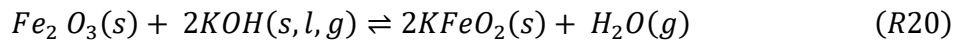


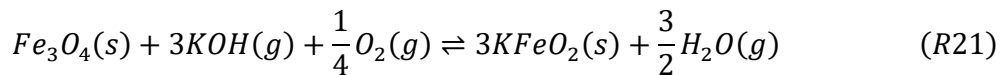
Fig. 8.5: BIB-milled SEM BSE cross-section images of the austenitic stainless steels exposed in the Clean scenario and Alkali-slip scenario for 168 hours at 700 °C: (a) 347H exposed in the Clean scenario; (b) 347H exposed in the Alkali-slip scenario; (c) high-magnification image of the area highlighted in (a); (d) EDX line scan of the selected area in (c);(f) Sanicro 25 exposed in the Clean scenario; (g) Sanicro 25 exposed in the Alkali-slip scenario with the corresponding EDX maps below; (h) 310H exposed in the Clean scenario; (i) 310H exposed in the Alkali-slip scenario with the corresponding EDX maps below.

The oxide morphologies of the austenitic stainless steels Sanicro 25 and 310H in the *Clean scenario* reveal the formation of local, Fe-rich oxide nodules (see Fig. 8.5, f and h). In the case of Sanicro 25, this degradation is mainly observed at the center of the alloy grains, whereas no clear pattern is evident for 310H. Although local breakaway corrosion is evident on the surface, it should be noted that the corrosion attack is slow, and the oxide scale remains strongly adherent to the alloy, with large areas retaining the primary protective Cr-rich oxide scale.

Upon exposure to KOH(g), breakaway corrosion over the entire surface was detected for both Sanicro 25 and 310H (see Fig. 8.5, g and i). Specifically, KFeO₂ was detected above a Fe-rich oxide scale on both samples (see Fig. 8.5, g and i, and the corresponding EDX maps). In addition, K₂CrO₄ was identified in the cross-sectional image of 310H (see Fig. 8.5i, and the corresponding EDX maps). Although not shown in the SEM image, XRD analysis suggested the formation of K₂CrO₄ on the surface of Sanicro 25. These findings indicate that KOH(g) accelerates the breakdown of the primary protective oxide scale by reacting with the primary protective Cr-rich oxide scale, as described by Reaction 18. It is further suggested that the Fe-rich oxide scale subsequently reacts with alkali, forming KFeO₂. Previous studies have proposed that hematite (Fe₂O₃) reacts with KOH to form KFeO₂ [166]:



It is suggested that similar reactions can occur in the presence of magnetite:



While the role of alkali in the primary protective oxide scale is clear, the impact of KFeO₂ formation on the corrosion rate beyond breakaway corrosion, i.e., in the secondary protective regime, is not yet fully understood. However, it is evident that the release of alkali in the form of KOH(g) will significantly accelerate the corrosion rate of austenitic stainless steels in the AR environment.

Sanicro 25 developed patchy internal oxidation zones following exposure to KOH(g), and these were particularly prominent in areas experiencing the most-significant corrosion (Fig. 8.5g). These regions were typically located at the center of the alloy grains. At the metal/internal oxidation interface, a continuous Cr-rich oxide layer was observed. However, the exact composition or phase of this oxide remains unknown. In addition, a Cu-rich oxide scale, likely CuO was detected on the surface of Sanicro 25 (from SEM/EDX analysis). The migration of Cu to the atmosphere/oxide interface is not yet fully understood. However, research on similar alloy types carried out by Intiso et al. suggests that Cu ions migrate via the oxide grain boundaries in the Cu²⁺ oxidation state under oxidizing conditions [167].

The Ni-based alloys showed no signs of breakaway corrosion in the *Clean scenario* (Fig. 8.6, a and c). This aligns well with the existing literature on the protective properties of Ni-based alloys in the presence of water vapor [156]. However, upon exposure to KOH(g), both alloys experienced breakaway corrosion. For Sanicro 63x59 and Sanicro 625, the presence of K₂CrO₄ and K₂(Mo,Cr)O₄, was detected by SEM/EDX (see Fig. 8.6, b and e, and the corresponding EDX maps). Both Sanicro 63x59 and Sanicro 625 formed an outward-growing, Ni-rich oxide that contained traces of Fe. Previous studies have suggested that Ni-rich oxides may serve as an effective barrier against Cr-evaporation, allowing recuperation of Cr near the metal/oxide interface, so as to form a protective healing layer [168]. A similar barrier effect may be present in the environment containing KOH(g), as in this study, there were no signs of interaction between the Ni-rich oxide and KOH(g). However, this remains to be confirmed. Nevertheless, signs of a Cr-rich oxide scale were observed beneath the Ni-rich oxide in both alloys, and this may contribute to the development of a continuous and stable healing layer over time. It was not determined if the oxide phase of this Cr-rich oxide is a spinel or a more-protective corundum.

Ni-base alloy

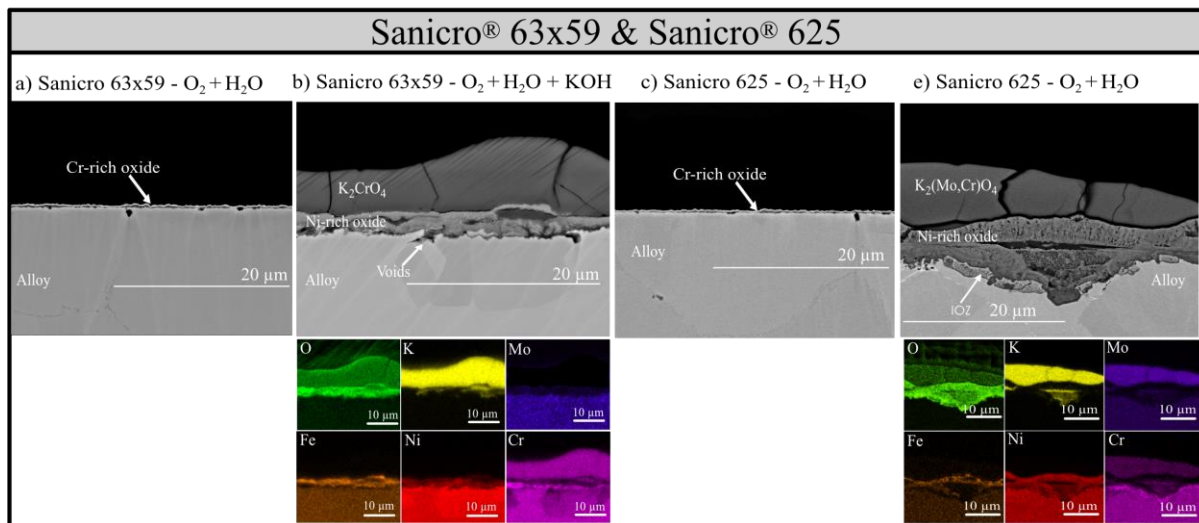


Fig. 8.6: BIB-milled SEM BSE cross-section images of the Ni-base alloys exposed in the clean and alkali slip scenario for 168 hours at 700 °C: (a) Sanicro® 63x59 exposed in the clean scenario; (b) Sanicro® 63x59 exposed in the alkali slip scenario with corresponding EDX maps below; (c) Sanicro® 625 exposed in the clean scenario; (e) Sanicro® 625 in the alkali slip scenario with corresponding EDX maps below.

8.4.2 Alumina-forming alloy

The FeCrAl alloy EF101 exhibited high levels of corrosion resistance in both environments, as indicated by the mass gains presented in Fig. 8.7a. SEM/EDX analysis of BIB-milled cross-sections suggested that the primary protective oxide scale remained intact regardless of the environment, and this scale was identified as being Al-rich according to EDX mapping (see Fig. 8.7, b and c). In both cases, the oxide scale remained within the nanometer size range and adhered well to the alloy. Upon exposure to KOH(g), a thin alkali-rich layer containing traces of Al was detected on top of the Al-rich oxide scale. However, due to its thickness, the exact composition could not be confirmed using the current XRD or SEM/EDX setup. Nevertheless, previous studies have suggested the formation of potassium-aluminates, such as KAlO₂ and Kal₉O₁₄, on Al-rich oxide scales [106, 169]. Further microstructural studies are required to determine the exact composition. Nevertheless, these findings support the discussion in Section 8.1.3, confirming that a predominantly pure Al-rich oxide scale forms on the EF101 surface in these environments. As a result, accelerated corrosion due to Cr-evaporation (Reaction 16) or Cr depletion by KOH(g) (Reaction 18) is non-existent after 168 hours of exposure. This suggests that EF101 exhibits excellent corrosion resistance in environments that contain both water vapor and KOH(g).

It is important to note that the FeCrAl alloy lacks the necessary pressure-bearing properties for them to be used as a bulk material for superheater tubes. Instead, this alloy is more suitable for applications such as weld overlay. However, this may affect its protective capacity. Research carried out by Ssenteza et al. has demonstrated that the corrosion resistance of a commercial FeCrAl alloy decreases when it is used as a weld overlay, as compared to a bulk material, at high temperatures and in the presence of alkali chlorides [170]. This was attributed due to microstructural changes introduced during the welding process. Another potential application of

the alloy is in co-extruded materials, where FeCrAl can be used as the outer layer to enhance corrosion resistance, while a pressure-resistant steel core provides structural integrity.

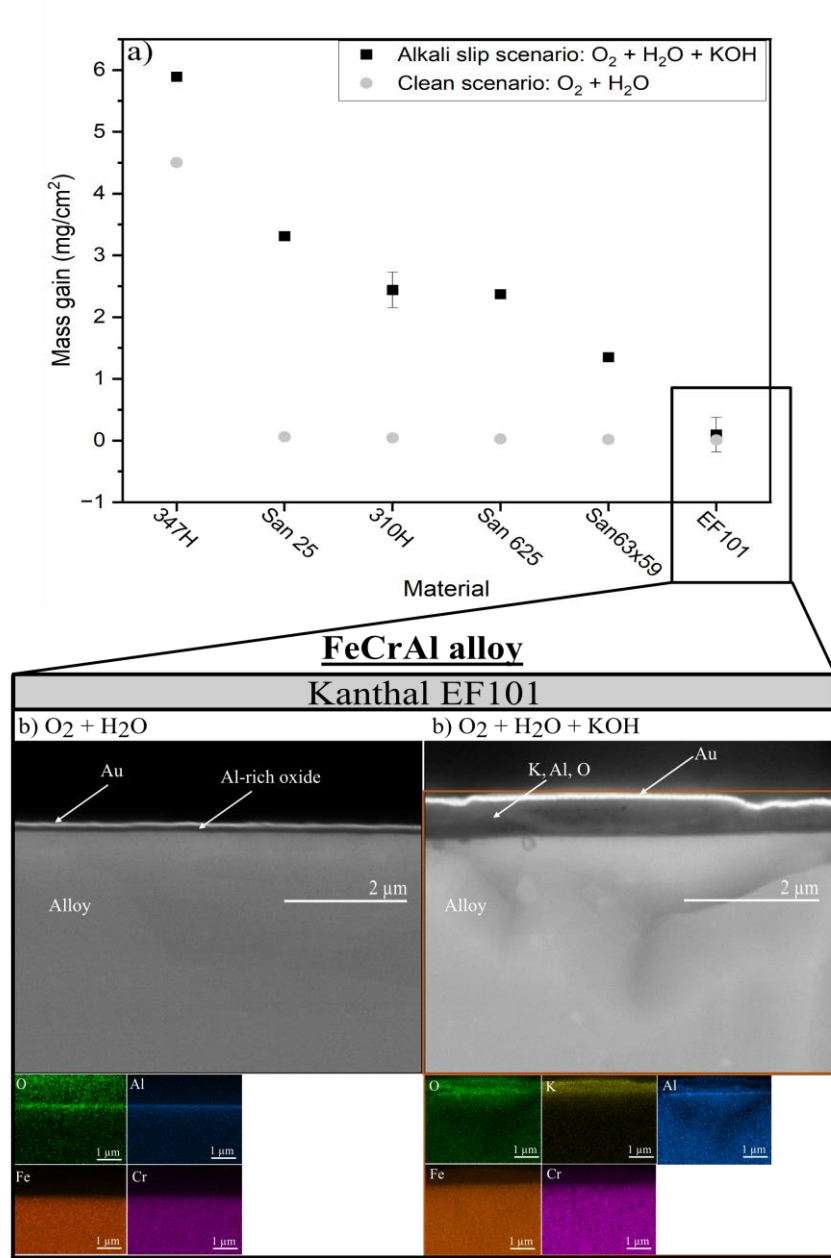


Fig. 8.7: Mass gain and BIB-milled SEM BSE cross-sectional images of the FeCrAl alloy EF101 exposed in the Clean scenario and Alkali-slip scenario for 168 hours at 700 °C: (a) mass gain; (b) EF101 exposed in the Clean scenario with the corresponding EDX maps below; and (c) EF101 exposed in the Alkali-slip scenario with the corresponding EDX maps below.

9. Concluding remarks

This thesis addresses the corrosion challenges associated with the combustion of biomass and waste-derived fuels for heat and electricity generation. The primary objective is to enhance the understanding of corrosion mechanisms under these conditions, thereby supporting the selection of suitable materials which can ultimately contribute to improved plant efficiency. The work includes corrosion studies on operational boilers, well-controlled laboratory set-ups, and the development of a new framework for lifetime prediction models of superheaters used in waste-fired boilers. In particular, this thesis identifies suitable materials for loop seal superheater applications, investigates PbCl₂-induced corrosion of low-alloyed steel, and introduces a novel framework to model the material degradation rates of superheater tubes by studying the relationships between material degradation, oxide scale microstructure, and operational conditions. Finally, this thesis explores the corrosion challenges related to chemical looping combustion of biomass and waste. A summary of the findings and concluding remarks is presented below.

9.1 Part I- Investigation of corrosion mechanisms in biomass and waste-fired boiler environments

In Paper I, long-term performance of various alloy types positioned in the loop seal of a CFB waste-fired boiler was investigated to address the following questions:

- ❖ What type of alloy material is suitable for this application?
- ❖ Does corrosion or erosion exert the strongest influence on the degradation rate of the material, or is there a synergism between erosion and corrosion?

All of the investigated alloys experienced breakaway corrosion after 6 months of exposure. Based on their performances over this period, the materials can be ranked (from best to worst) as follows: SX > Sanicro 625 > EF100 > EF101 > 316Ti. The SX alloy developed a thin oxide layer that was enriched in Cr and Si at the metal/oxide interface, which progressed along the grain boundaries within the alloy. The Si-rich oxides detected in stainless steels have been reported in previous studies to mitigate corrosion. Although intergranular corrosion increased over time, the total material loss after 12 months remained relatively low at 0.24 mm for the SX alloy. The Ni-based alloys formed a uniform, outward-growing, Ni-rich oxide scale, with an underlying Cr-rich oxide layer. This Cr-rich oxide is suggested to play a key role in reducing the degradation rate observed after 6 months of exposure. The corrosion performances of the FeCrAl alloys EF100 and EF101 were on par with those of the Ni-based alloys Sanicro 625 and SX after 6 months of exposure. However, EF100 and EF101 experienced significant nitridation, which became more pronounced with longer exposure time in the case of EF100. While this did not appear to result in substantial corrosion, as evidenced by the relatively low material loss for EF100 after 12 months (0.19 mm compared to 0.13 mm after 6 months), the long-term mechanical properties may have been negatively affected.

Finally, the microstructural analyses confirmed that, in many cases, thick oxide scales and deposits remained on the samples, suggesting that the degradation mechanisms are primarily driven by corrosion and not by erosion.

In paper II, A time-resolved study of PbCl₂-induced corrosion of a low-alloyed steel was conducted in a well-controlled laboratory environment to address the following questions:

- ❖ How do the initiation and propagation corrosion mechanisms differ from each other?
- ❖ How do the individual elements of Pb and Cl affect the corrosion rate?

After only 1 hour of exposure, the low-alloyed steel exhibited severe corrosion in the presence of PbCl₂. The predominant corrosion mechanism was significant delamination of the oxide scale. It is proposed that the initiation of the corrosion attack is the result of Cl release following a two-step reaction between PbCl₂ and the surrounding environment (see Reactions 14 & 15). This process leads to the diffusion of Cl ions to the metal/oxide interface, promoting the formation of iron chlorides, which reduces the adhesive properties of the oxide scale. After 24 hours of exposure, no Cl-containing compounds were detected on the oxide surface. Nevertheless, the high corrosion rate persisted. It is likely that iron chlorides remain at the metal/oxide interface and continue to promote delamination of the oxide scale throughout the exposure period. Some regions of the alloy exhibited significant degradation despite having dense, well-adherent oxide scales. In these cases, it is proposed that Cl enhances the diffusion rate of ions through the oxide scale.

The PbO formed after 24 hours of exposure reacts with the Fe-rich oxide scale on the surface, presumably resulting in the formation of magnetoplumbite (Fe₁₂PbO₁₉). This compound is suggested to promote protective properties by reducing diffusion through the dense oxide layers. However, the presence of PbCl₂ promotes the formation of cracks and delamination of the oxide scale, creating rapid diffusion pathways that bypass the surface oxide structure. As a consequence, the protective effects of magnetoplumbite are negligible.

The aim of **Paper III** was to develop a predictive framework that integrates characterization of the oxide microstructure (specifically, the oxide grain size), kinetic simulations, and boiler operational data to model long-term material degradation in superheater tubes that are exposed to waste-fired boiler environments. When simulating scenarios with high Cl loads and comparing the predicted material losses to the experimentally measured material losses, discrepancies were observed both in the absolute values and in the kinetic behaviors. The simulation predicted parabolic growth of material loss, whereas the measured data exhibited a linear growth trend. Microstructural analyses of samples exposed to waste-fired boilers suggest that oxide growth is primarily governed by the diffusion of charged species through the oxide scale. Consequently, it is argued that simulating material losses using parabolic kinetics remains a valid approach. However, it is proposed that oxide growth cannot be accurately represented in terms of continuous, single oxide scale formation. Instead, the oxidation process is likely to involve periodic restarts of the oxide scale formation, which, over extended periods, may approximate a linear relationship. The precise mechanisms underlying the delamination and subsequent restart of the oxide scale remain speculative, although it is suggested that Cl species and thermal cycling participate in this process. Given the complexity of the suggested framework and the limited availability of long-term, high-resolution datasets, further field measurements and microstructural analyses are strongly recommended to validate and refine the proposed predictive framework.

9.2 Part II- Potential corrosion challenges in chemical looping combustion of biomass

A novel experimental set-up was developed to study corrosion related to CLC of biomass in **Paper IV**, aiming to address the following questions:

- ❖ What material is suitable for superheater application in the AR side of a CLC unit combusting biomass?
- ❖ How does significant alkali release affect the corrosion rate of the different materials and consequently, their suitability for use?

In the first study, the alloys were exposed to the so-called *Clean scenario*, which refers to the laboratory setup designed to simulate an environment in the AR of CLC without any influence from the FR (5% O₂ + 3% H₂O + N₂ bal.). Under these conditions, all of the tested alloys, with the exception of 347H, demonstrated strong resistance to corrosion. Localized breakaway corrosion was observed on the AISI 310H and Sanicro 25 stainless steels. However, the mass gain was minimal, and the oxide scales remained dense and adherent to the substrate. It is argued that local breakaway corrosion is triggered by Cr evaporation. The Ni-based alloys (Sanicro 625 and Sanicro 63x59) and the FeCrAl alloy EF101 showed no signs of breakaway corrosion. Cr-rich and Al-rich oxide scales were present on the Sanicro 625 and Sanicro 63x59 alloys, respectively. In contrast, the AISI 347H alloy suffered severe breakaway corrosion in both scenarios. Significant oxide scale spallation during cooling further indicated the unsuitability of AISI 347H for superheater applications in this environment.

In the *Alkali-slip scenario*, a laboratory setup was developed to simulate the continuous release of KOH(g) in the AR (5% O₂ + 3% H₂O + N₂ bal. + 16 ppm KOH(g)). Under these conditions, all the stainless steels and Ni-based alloys underwent breakaway corrosion. The dominant mechanism was identified as the reaction between KOH(g) and the Cr-rich oxide scale, resulting in the formation of potassium chromate. This reaction leads to Cr depletion of the oxide layer, which initiates the transition to the secondary corrosion regime and the formation of a less-protective, multilayered oxide scale. In contrast, the FeCrAl alloy Kanthal EF101 maintained an Al-rich oxide scale in the presence of KOH(g). It is argued that the oxide scale contains a low amount of Cr, thereby preventing rapid breakdown of the primary protective oxide related to Cr depletion via Cr evaporation or the formation of potassium chromates. Potassium aluminate formation was observed on the surface when exposed to KOH(g), although this did not influence the corrosion rate, which remained low after 168 hours of exposure.

10. Outlook

10.1. Part I- Investigation of corrosion mechanisms in biomass and waste-fired boiler environments

- ❖ For the novel FeCrAl alloys to become strong contenders as commercial alloys for loop seal superheater applications, it is important to expand our understanding of the effects of nitridation on corrosion over longer periods of time. Well-controlled laboratory studies on this subject should be undertaken. A possible approach would be to develop an experimental set-up with low partial pressure of oxygen in the presence of nitrogen, so as to “pre-nitridate” the samples and then expose them to a corrosive environment, while comparing with samples that do not undergo the pre-nitridation step.
- ❖ PbCl₂ is argued to promote delamination of the oxide scale formed on the low-alloyed steel T22. To investigate further the delamination mechanisms, additional microstructural analyses using TEM are needed. Combining TEM with EDX would allow high-magnification imaging, which would provide us with more information of the composition of each oxide scale observed in this study. This approach would help to determine whether delamination occurs during exposure or if it is a result of sample preparation. If delamination happens during exposure, a consistent oxide morphology should be seen across all delaminated scales, specifically an outward-growing oxide composed of hematite and magnetite, growing on top of an inward-growing (Fe,Cr)₃O₄ spinel.
- ❖ While the novel approach for predicting material loss in superheater tubes through the integration of microstructural characterization, boiler operating conditions, and kinetic simulations, shows potential, its accuracy and reliability are currently limited by the availability and quality of input data. Notably, the present model assumes a constant oxide grain size, thereby overlooking the effects of grain growth over time. Future model developments should incorporate time-dependent grain coarsening, as this could significantly impact diffusion kinetics by reducing grain boundary density and thus modifying the parabolic oxidation behavior. Time-resolved field exposures would be particularly valuable in assessing oxidation dynamics during operational. It is also acknowledged that the current literature review that was used to derive α -values from laboratory-scale studies can be much improved. However, the aim of this study was not to establish a comprehensive database of α -values, but rather to initiate a discussion on the feasibility and structure of the proposed modeling framework. That said, expanding the literature review particularly with studies covering a range of materials, temperatures, and chlorine-loading conditions will be important to improve the framework. In the current study, it was difficult to determine whether a re-initiation of oxide growth had occurred via microstructural analysis, due to extensive spallation and challenges in conducting reliable EDX analysis on the remaining oxide layers above the dense scale.

10.2 Part II- Potential corrosion challenges in chemical looping combustion of biomass

Long-term corrosion studies are essential to follow up the results presented in this thesis. These studies will help to determine if any of the alloy types can form healing layers that effectively

reduce the corrosion rate well beyond breakaway corrosion. Indications of the formation of a healing layer were observed on the Ni-based alloys, although longer exposure times are needed for clarification of this phenomenon. Furthermore, it will be important to follow up the results obtained for the FeCrAl alloy EF101 with experiments that entail longer exposures, to see if the potassium-aluminate compound promotes breakaway corrosion over time.

The experimental set-up developed in this study has certain limitations. The approach to simulating the continuous release of KOH(g) depends on the equilibrium pressure established by the reaction between K₂CO₃(s) and the surrounding environment. As such, the gas composition and the temperature directly affect the KOH(g) levels. This means that key parameters, such as temperature, cannot be adjusted independently without also affecting the KOH(g) concentration. To address this, an alternative approach for generating KOH(g) should be considered. A method that has proven successful in previous studies is to introduce alkali in the form of sub-micron particles suspended in a gas [171, 172]. This could be carried out using an aerosol particle atomizer, where the mass concentration of KOH is controlled by adjusting the concentration of the liquid KOH solution fed into the atomizer. Furthermore, this technique is advantageous because it can be adapted for various alkali solutions relevant for corrosion studies of materials in CLC of biomass.

While the studies described in this thesis provide valuable insights into the corrosion challenges associated with CLC of biomass, they were conducted under well-controlled laboratory conditions that do not fully represent the complexities of actual operational environments. Laboratory-scale investigations are important for isolating and understanding the effects of individual parameters. In this case, the continuous release of KOH(g) was simulated to identify potential corrosion challenges in the AR. However, to gain a more-comprehensive understanding of corrosion, follow-up studies in pilot-scale and full-scale setups are essential. Future work should include corrosion measurements using probes positioned on both the AR side and FR side. These measures will enable direct observations of corrosion under actual operating conditions. These studies will also be critical for analyzing the deposits formed on the corrosion probes, particularly those on superheater surfaces, to determine what, if any, chemical species are transported from the FR to the AR. This information will help us to develop laboratory experimental setups that more-accurately represent the environment in the AR. Such studies have yet to be conducted for CLC of biomass or waste but are scheduled to be carried out in Year 2025 in pilot-scale CLC units at Chalmers University of Technology (Sweden) and in Darmstadt (Germany), within the CETPartnership-funded project *ACLOUD – Advancing Chemical-Looping Combustion of Domestic Fuels* [173].

11. References

1. Yoro KO, Daramola MO. CO₂ emission sources, greenhouse gases, and the global warming effect. *Advances in carbon capture*: Elsevier; 2020. p. 3-28.
2. Li T, Baležentis T, Makuténienė D, Streimikiene D, Kriščiukaitienė I. Energy-related CO₂ emission in European Union agriculture: Driving forces and possibilities for reduction. *Applied Energy*. 2016;180:682-94.
3. Meinshausen M, Meinshausen N, Hare W, Raper SC, Frieler K, Knutti R, et al. Greenhouse-gas emission targets for limiting global warming to 2 C. *Nature*. 2009;458(7242):1158-62.
4. Allen MR, Frame DJ, Huntingford C, Jones CD, Lowe JA, Meinshausen M, et al. Warming caused by cumulative carbon emissions towards the trillionth tonne. *Nature*. 2009;458(7242):1163-6.
5. Lee H, Calvin K, Dasgupta D, Krinner G, Mukherji A, Thorne P, et al. AR6 Synthesis Report: Climate Change 2023. Summary for Policymakers. 2023.
6. Pörtner H-O, Roberts DC, Adams H, Adler C, Aldunce P, Ali E, et al. Climate change 2022: Impacts, adaptation and vulnerability: IPCC Geneva, Switzerland:; 2022.
7. Jamieson MA, Trowbridge AM, Raffa KF, Lindroth RL. Consequences of climate warming and altered precipitation patterns for plant-insect and multitrophic interactions. *Plant physiology*. 2012;160(4):1719-27.
8. Lindmark M, Audzijonyte A, Blanchard JL, Gårdmark A. Temperature impacts on fish physiology and resource abundance lead to faster growth but smaller fish sizes and yields under warming. *Global Change Biology*. 2022;28(21):6239-53.
9. Kennedy J, Trewin B, Betts R, Thorne P, Foster P, Siegmund P, et al. State of the Climate 2024. Update for COP29. 2024.
10. Information NNCfE. Climate at a glance: Global time series 2022 [Available from: <https://www.ncdc.noaa.gov/cag/>].
11. Studies NGIfS. GISS ModelE: Well-Mixed Greenhouse Gases – Global Mean Annual GHG Concentrations 2022 [Available from: <https://data.giss.nasa.gov/modelforce/ghgases/Fig1A.ext.txt>].
12. Laboratory NGM. Trends in Atmospheric Carbon Dioxide – Data. 2024.
13. Agency IE. CO₂ Emissions in 2022 2023 [Available from: <https://www.iea.org/reports/co2-emissions-in-2022>].
14. IEA (2020) GER, IEA, Paris <https://www.iea.org/reports/global-energy-review-2019>, Licence: CC BY 4.0.
15. Mitigation CC. IPCC special report on renewable energy sources and climate change mitigation. *Renewable Energy*. 2011;20(11).
16. Association WB. Global bioenergy statistics 2019. World Bioenergy Association. 2020.
17. Brunner T, Fluch J, Obernberger I, Warnecke R. Investigations of aerosol formation pathways during MSW combustion based on high-temperature impactor measurements. *Fuel processing technology*. 2013;105:154-60.
18. Spiegel M. Salt melt induced corrosion of metallic materials in waste incineration plants. *Materials and corrosion*. 1999;50(7):373-93.
19. Bøjer M, Jensen PA, Frandsen F, Dam-Johansen K, Madsen OH, Lundtorp K. Alkali/Chloride release during refuse incineration on a grate: Full-scale experimental findings. *Fuel Processing Technology*. 2008;89(5):528-39.
20. Eklund J, Paz MD, Jönsson B, Liske J, Svensson JE, Jonsson T. Field exposure of FeCrAl model alloys in a waste-fired boiler at 600° C: The influence of Cr and Si on the corrosion behaviour. *Materials and Corrosion*. 2019;70(8):1476-85.
21. Pettersson J, Svensson JE, Johansson LG, editors. Alkali induced corrosion of 304-type austenitic stainless steel at 600 C; comparison between KCl, K₂CO₃ and K₂SO₄. *Materials science forum*; 2008: Trans Tech Publ.

22. Enestam S, Bankiewicz D, Tuiremo J, Mäkelä K, Hupa M. Are NaCl and KCl equally corrosive on superheater materials of steam boilers? *Fuel*. 2013;104:294-306.
23. Francis Chinweuba E. Efficiency Improvements in Waste-to-Energy Combustion Processes: Method Development and Evaluation: Högskolan i Borås; 2019.
24. Energy U. Energy efficiency and renewable energy. US Government, Department of Energy, Tech Rep, 2008, dOE/GO-102008-2567. 2004.
25. IEA. Energy Efficiency Indicators for Public Electricity Production from Fossil Fuels, Paris,
- 2008 [Available from: <https://www.iea.org/reports/energy-efficiency-indicators-for-public-electricity-production-from-fossil-fuels>].
26. Bankiewicz D, Enestam S, Yrjas P, Hupa M. Experimental studies of Zn and Pb induced high temperature corrosion of two commercial boiler steels. *Fuel Processing Technology*. 2013;105:89-97.
27. Kinnunen H, Hedman M, Engblom M, Lindberg D, Uusitalo M, Enestam S, et al. The influence of flue gas temperature on lead chloride induced high temperature corrosion. *Fuel*. 2017;196:241-51.
28. Núñez AM, Börjesson E, Kinnunen H, Lindberg D, Norling R. Influence of PbCl₂ and KCl salt mixture on high temperature corrosion of alloy 625. *Fuel*. 2024;358:130196.
29. Johansson A, Johnsson F, Andersson B-Å. The performance of a loop seal in a CFB boiler. 2006.
30. Nafari A, Nylund A. Field study on superheater tubes in the loop seal of a wood fired CFB plant. *Materials and Corrosion*. 2004;55(12):909-20.
31. Havercroft I. Brief-CCS in the IPCC Sixth Assessment (AR6) Synthesis Report. 2023.
32. Kemper J. Biomass and carbon dioxide capture and storage: A review. *International Journal of Greenhouse Gas Control*. 2015;40:401-30.
33. Regeringskansliet. Vägen till en klimatpositiv framtid SOU2020:4 29 January 20202020 [Available from: <https://www.regeringen.se/rattsliga-dokument/statens-offentliga-utredningar/2020/01/sou-20204/>].
34. Karlsson A, Boström B, Jernbäcker E, Lundblad M, Mjureke D. Vägen till en klimatpositiv framtid. SOU 2020: Betänkande från Klimatpolitiska vägvalsutredningen (M 2018: 07). Elanders Sverige AB; 2020.
35. Rydén M, Lyngfelt A, Langørgen Ø, Larring Y, Brink A, Teir S, et al. Negative CO₂ emissions with chemical-looping combustion of biomass—a Nordic energy research flagship project. *Energy Procedia*. 2017;114:6074-82.
36. Gogolev I. Determining the Fate and Operational Implications of Alkalies in Chemical Looping Combustion of Biomass: Chalmers Tekniska Hogskola (Sweden); 2020.
37. Gogolev I, Soleimanisalim AH, Mei D, Lyngfelt A. Effects of Temperature, Operation Mode, and Steam Concentration on Alkali Release in Chemical Looping Conversion of Biomass—Experimental Investigation in a 10 kWth Pilot. *Energy & Fuels*. 2022;36(17):9551-70.
38. Ekpe B. Modelling fireside corrosion of superheaters and reheaters following coal and biomass combustion. 2019.
39. Nunes L, Matias J, Catalão J. Biomass combustion systems: A review on the physical and chemical properties of the ashes. *Renewable and Sustainable Energy Reviews*. 2016;53:235-42.
40. Mudgal D, Singh S, Prakash S. Corrosion Problems in Incinerators and Biomass-Fuel-Fired Boilers. *International Journal of Corrosion*. 2014;2014(1):505306.
41. Shao Y, Wang J, Preto F, Zhu J, Xu C. Ash deposition in biomass combustion or co-firing for power/heat generation. *Energies*. 2012;5(12):5171-89.
42. Kalembkiewicz J, Chmielarz U. Ashes from co-combustion of coal and biomass: New industrial wastes. *Resources, Conservation and Recycling*. 2012;69:109-21.
43. Caillat S, Vakkilainen E. Large-scale biomass combustion plants: an overview. *Biomass combustion science, technology and engineering*. 2013:189-224.
44. Unchaisri T, Fukuda S. Investigation of ash formation and deposit characteristics in CFB co-combustion of coal with various biomass fuels. *Journal of the Energy Institute*. 2022;105:42-52.

45. EPA U. Energy recovery from the combustion of municipal solid waste (MSW). Retrieved April. 2023;22:2023.
46. Kalogirou EN. Waste-to-Energy technologies and global applications: CRC Press; 2017.
47. Krook J, Mårtensson A, Eklund M. Sources of heavy metal contamination in Swedish wood waste used for combustion. *Waste Management*. 2006;26(2):158-66.
48. Huron M, Oukala S, Lardière J, Giraud N, Dupont C. An extensive characterization of various treated waste wood for assessment of suitability with combustion process. *Fuel*. 2017;202:118-28.
49. Kinnunen H, Hedman M, Lindberg D, Enestam S, Yrjas P. Corrosion in recycled wood combustion—reasons, consequences, and solutions. *Energy & Fuels*. 2019;33(7):5859-66.
50. Yin C, Rosendahl LA, Kær SK. Grate-firing of biomass for heat and power production. *Progress in Energy and Combustion Science*. 2008;34(6):725-54.
51. Van Caneghem J, Brems A, Lievens P, Block C, Billen P, Vermeulen I, et al. Fluidized bed waste incinerators: Design, operational and environmental issues. *Progress in Energy and Combustion Science*. 2012;38(4):551-82.
52. Bankiewicz D. Corrosion behaviour of boiler tube materials during combustion of fuels containing Zn and Pb. 2012.
53. Henderson P, Höglberg J, Mattsson M. Reduction of fireside corrosion of superheater materials in a biomass-fired circulating fluidised bed boiler. 2002.
54. Nafari A, Nylund A. Erosion corrosion of steel tubes in the loop seal of a biofuel fired CFB plant. 2002.
55. Mettanant V, Basu P, Butler J. Agglomeration of biomass fired fluidized bed gasifier and combustor. *The Canadian Journal of Chemical Engineering*. 2009;87(5):656-84.
56. Christodoulou C, Grimekis D, Panopoulos K, Pachatouridou E, Iliopoulou E, Kakaras E. Comparing calcined and un-treated olivine as bed materials for tar reduction in fluidized bed gasification. *Fuel processing technology*. 2014;124:275-85.
57. Corcoran A, Marinkovic J, Lind F, Thunman H, Knutsson P, Seemann M. Ash properties of ilmenite used as bed material for combustion of biomass in a circulating fluidized bed boiler. *Energy & Fuels*. 2014;28(12):7672-9.
58. Plants tCoEW-t-E. <https://www.cewep.eu/waste-to-energy-plants-in-europe-in-2022/> [Available from: <https://www.cewep.eu/waste-to-energy-plants-in-europe-in-2022/>].
59. Mantripragada HC, Zhai H, Rubin ES. Boundary Dam or Petra Nova—Which is a better model for CCS energy supply? *International Journal of Greenhouse Gas Control*. 2019;82:59-68.
60. Yamada H. Amine-based capture of CO₂ for utilization and storage. *Polymer Journal*. 2021;53(1):93-102.
61. Panja P, McPherson B, Deo M. Techno-economic analysis of amine-based CO₂ capture technology: Hunter Plant case study. *Carbon Capture Science & Technology*. 2022;3:100041.
62. Lyngfelt A. Chemical looping combustion: status and development challenges. *Energy & Fuels*. 2020;34(8):9077-93.
63. Jacobs B, Tantikhajorngsol P, Hill K, Ruffini J, Wilkes S, Srisang W, et al., editors. Reducing the CO₂ Emission Intensity of Boundary Dam Unit 3 Through Optimization of Operating Parameters of the Power Plant and Carbon Capture Facilities. Proceedings of the 16th Greenhouse Gas Control Technologies Conference (GHGT-16); 2022.
64. Beiron J, Normann F, Johnsson F. A techno-economic assessment of CO₂ capture in biomass and waste-fired combined heat and power plants—A Swedish case study. *International Journal of Greenhouse Gas Control*. 2022;118:103684.
65. Navedkhan M, Lakshminarayan J, Biliyok C, Levihn F, editors. Integration of hot potassium carbonate CO₂ capture process to a combined heat and power plant at Värtaverket. Proceedings of the 16th Greenhouse Gas Control Technologies Conference (GHGT-16); 2022.
66. Levihn F, Linde L, Gustafsson K, Dahlen E. Introducing BECCS through HPC to the research agenda: The case of combined heat and power in Stockholm. *Energy reports*. 2019;5:1381-9.
67. Toftegaard MB, Brix J, Jensen PA, Glarborg P, Jensen AD. Oxy-fuel combustion of solid fuels. *Progress in energy and combustion science*. 2010;36(5):581-625.

68. Buhre BJ, Elliott LK, Sheng C, Gupta RP, Wall TF. Oxy-fuel combustion technology for coal-fired power generation. *Progress in energy and combustion science*. 2005;31(4):283-307.
69. Wall TF. Combustion processes for carbon capture. *Proceedings of the combustion institute*. 2007;31(1):31-47.
70. Davison J. Performance and costs of power plants with capture and storage of CO₂. *Energy*. 2007;32(7):1163-76.
71. Hussain T, Syed A, Simms NJ. Trends in fireside corrosion damage to superheaters in air and oxy-firing of coal/biomass. *Fuel*. 2013;113:787-97.
72. Agüero A, Baráibar I, Gutiérrez M, Hernández M, Muelas R, Rodríguez S. Biomass corrosion behavior of steels and coatings in contact with KCl/K₂SO₄ at 550 C under an oxy-fuel combustion atmosphere: a screening laboratory test. *Surface and Coatings Technology*. 2018;350:188-200.
73. Syed A, Simms N, Oakey J. Fireside corrosion of superheaters: Effects of air and oxy-firing of coal and biomass. *Fuel*. 2012;101:62-73.
74. Lyngfelt A. Chemical looping combustion (CLC). Fluidized bed technologies for near-zero emission combustion and gasification: Elsevier; 2013. p. 895-930.
75. Azis MM, Jerndal E, Leion H, Mattisson T, Lyngfelt A. On the evaluation of synthetic and natural ilmenite using syngas as fuel in chemical-looping combustion (CLC). *Chemical Engineering Research and Design*. 2010;88(11):1505-14.
76. Qasim M, Ayoub M, Ghazali NA, Aqsha A, Ameen M. Recent advances and development of various oxygen carriers for the chemical looping combustion process: a review. *Industrial & Engineering Chemistry Research*. 2021;60(24):8621-41.
77. Ohlemüller P, Ströhle J, Epple B. Chemical looping combustion of hard coal and torrefied biomass in a 1 MWth pilot plant. *International Journal of Greenhouse Gas Control*. 2017;65:149-59.
78. Linderholm C, Schmitz M, Biermann M, Hanning M, Lyngfelt A. Chemical-looping combustion of solid fuel in a 100 kW unit using sintered manganese ore as oxygen carrier. *International Journal of Greenhouse Gas Control*. 2017;65:170-81.
79. Gogolev I, Soleimanisalim AH, Linderholm C, Lyngfelt A. Commissioning, performance benchmarking, and investigation of alkali emissions in a 10 kWth solid fuel chemical looping combustion pilot. *Fuel*. 2021;287:119530.
80. Langørgen Ø, Saanum I, Khalil RA, Haugen NEL. CLC of waste-derived fuel and biomass in a 150-kW pilot unit. 2022.
81. Alakangas E, Asikainen A, Grammelis P, Hämäläinen J, Haslinger W, Janssen R, et al., editors. *Biomass technology roadmap: European technology platform on renewable heating and cooling*. Renewable Heating & Cooling European Technology Platform: 2030 Reason to Integrate Renewable Heating and Cooling: Innovation, Technology Development and Market Uptake; 2014.
82. KOFSTAD P. High temperature corrosion((Book)). London and New York, Elsevier Applied Science, 1988, 568. 1988.
83. Birks N, Meier GH, Pettit FS. *Introduction to the high temperature oxidation of metals*: Cambridge university press; 2006.
84. Young DJ. *High temperature oxidation and corrosion of metals*: Elsevier; 2008.
85. Andersson J-O, Helander T, Höglund L, Shi P, Sundman B. Thermo-Calc & DICTRA, computational tools for materials science. *Calphad*. 2002;26(2):273-312.
86. Bigdeli S, Kjellqvist L, Naraghi R, Höglund L, Larsson H, Jonsson T. Strategies for high-temperature corrosion simulations of Fe-based alloys using the calphad approach: part I. *Journal of phase equilibria and diffusion*. 2021;42(3):403-18.
87. Tammann G. Über Anlauffarben von metallen. *Zeitschrift für anorganische und allgemeine Chemie*. 1920;111(1):78-89.
88. Wagner C. Beitrag zur theorie des anlaufvorgangs. *Zeitschrift für physikalische Chemie*. 1933;21(1):25-41.
89. Cruchley S, Evans H, Taylor M, Hardy M, Stekovic S. Chromia layer growth on a Ni-based superalloy: Sub-parabolic kinetics and the role of titanium. *Corrosion science*. 2013;75:58-66.

90. Bataillou L, Desgranges C, Martinelli L, Monceau D. Modelling of the effect of grain boundary diffusion on the oxidation of Ni-Cr alloys at high temperature. *Corrosion science*. 2018;136:148-60.
91. Gao D, Shen Z, Chen K, Zhou X, Liu H, Wang J, et al. Review of progress in calculation and simulation of high-temperature oxidation. *Progress in Materials Science*. 2024;101348.
92. Atkinson A, Taylor R, Hughes A. A quantitative demonstration of the grain boundary diffusion mechanism for the oxidation of metals. *Philosophical Magazine A*. 1982;45(5):823-33.
93. Lillerud K, Kofstad P. On high temperature oxidation of chromium: I. Oxidation of annealed, thermally etched chromium at 800–1100 C. *Journal of the electrochemical society*. 1980;127(11):2397.
94. Sabioni ACS, Souza JNV, Ji V, Jomard F, Trindade VB, Carneiro JF. Study of ion diffusion in oxidation films grown on a model Fe–15% Cr alloy. *Solid State Ionics*. 2015;276:1-8.
95. Sabioni ACS, Ramos RPB, Ji V, Jomard F, Macedo WAdA, Gastelois PL, et al. About the role of chromium and oxygen ion diffusion on the growth mechanism of oxidation films of the AISI 304 austenitic stainless steel. *Oxidation of metals*. 2012;78(3):211-20.
96. Young J. Oxidation of alloys II: internal oxidation. *Corrosion Series*. 2008;1:247-314.
97. Zhou R, Wang F, Xu K, Yuan Y, Chen L, Lou M, et al. Effect of molybdenum addition on oxidation behavior and secondary protection mechanism of FeCrAl coatings. *Materials Characterization*. 2023;204:113221.
98. Eklund J, Persdotter A, Hanif I, Bigdeli S, Jonsson T. Secondary corrosion protection of FeCr (Al) model alloys at 600° C—The influence of Cr and Al after breakaway corrosion. *Corrosion Science*. 2021;189:109584.
99. Olivas Ogaz MA. High Temperature Corrosion of Low-Alloyed and Stainless Steels: Mechanistic Study of Chlorine-Induced Corrosion. Ph D Thesis. 2019.
100. Persdotter A, Eklund J, Liske J, Jonsson T. Beyond breakaway corrosion—Influence of chromium, nickel and aluminum on corrosion of iron-based alloys at 600° C. *Corrosion Science*. 2020;177:108961.
101. Ssenteza V, Eklund J, Bigdeli S, Jonsson T. Long-term corrosion behavior of FeCr (Al, Ni) alloys in O₂+ H₂O with KCl (s) at 600° C: Microstructural evolution after breakaway oxidation. *Corrosion Science*. 2024;226:111654.
102. Ssenteza V, Olausson MDP, Eklund J, Nockert J, Liske J, Jonsson Tr. High-Temperature Corrosion Behavior of Superheater Materials at 600° C: Insights from Laboratory and Field Exposures. *Energy & Fuels*. 2024;39(1):819-27.
103. Persdotter A, Sattari M, Larsson E, Ogaz MO, Liske J, Jonsson T. Oxidation of Fe-2.25 Cr-1Mo in presence of KCl (s) at 400 C—Crack formation and its influence on oxidation kinetics. *Corrosion Science*. 2020;163:108234.
104. Larsson E, Gruber H, Hellström K, Jonsson T, Liske J, Svensson J-E. A Comparative Study of the Initial Corrosion of KCl and PbCl₂ on a Low-Alloyed Steel. *Oxidation of metals*. 2017;87:779-87.
105. Viswanathan R, Bakker W. Materials for ultrasupercritical coal power plants—Boiler materials: Part 1. *Journal of materials engineering and performance*. 2001;10:81-95.
106. Okoro SC, Montgomery M, Frandsen FJ, Pantleon K. Influence of preoxidation on high-temperature corrosion of a FeCrAl alloy under conditions relevant to biomass firing. *Oxidation of Metals*. 2018;89:99-122.
107. Sadique S, Mollah A, Islam M, Ali M, Megat M, Basri S. High-temperature oxidation behavior of iron–chromium–aluminum alloys. *Oxidation of Metals*. 2000;54:385-400.
108. Ejenstam J, Thuvander M, Olsson P, Rave F, Szakalos P. Microstructural stability of Fe–Cr–Al alloys at 450–550 C. *Journal of Nuclear Materials*. 2015;457:291-7.
109. Pohja R, Hänninen H. Properties of FeCrAl Alloys and Austenitic Stainless Steel for Boiler Environments. 2010.
110. Nielsen HP, Frandsen F, Dam-Johansen K, Baxter L. The implications of chlorine-associated corrosion on the operation of biomass-fired boilers. *Progress in energy and combustion science*. 2000;26(3):283-98.

111. McNallan M, Liang W, Kim S, Kang C. Acceleration of the high temperature oxidation of metals by chlorine. *High Temperature Corrosion*, NACE. 1983;316.
112. Grabke H, Reese E, Spiegel M. The effects of chlorides, hydrogen chloride, and sulfur dioxide in the oxidation of steels below deposits. *Corrosion science*. 1995;37(7):1023-43.
113. Pettersson J. Alkali Induced High Temperature Corrosion of Stainless Steel-Experiences from Laboratory and Field: Chalmers University of Technology; 2008.
114. Folkeson N, Johansson L-G, Svensson J-E. Initial stages of the HCl-induced high-temperature corrosion of alloy 310. *Journal of the electrochemical society*. 2007;154(9):C515.
115. Jonsson T, Folkeson N, Svensson J-E, Johansson L-G, Halvarsson M. An ESEM in situ investigation of initial stages of the KCl induced high temperature corrosion of a Fe–2.25 Cr–1Mo steel at 400 °C. *Corrosion Science*. 2011;53(6):2233-46.
116. Persdotter A, Sattari M, Larsson E, Olivas Ogaz MA, Liske J, Jonsson T. Oxidation of Fe-2.25Cr-1Mo in presence of KCl(s) at 400 °C – Crack formation and its influence on oxidation kinetics. *Corrosion Science*. 2020;163:108234.
117. Kinnunen H. The role and corrosivity of lead in recycled wood combustion. 2019.
118. Enestam S. Corrosivity of hot flue gases in the fluidized bed combustion of recovered waste wood. 2011.
119. Sergeev D, Kobertz D, Müller M. Thermodynamics of the NaCl–KCl system. *Thermochimica acta*. 2015;606:25-33.
120. Enestam SH, Fabritius MK, Hulkkoonen SK, Ro“ ppa” nen JT, editors. Control of Ash-Related Operational Problems in BFB Combustion of Biofuels and Waste. International Conference on Fluidized Bed Combustion; 2003.
121. Gabriel A, Pelton AD. Phase diagram measurements and thermodynamic analysis of the PbCl₂–NaCl, PbCl₂–KCl, and PbCl₂–KCl–NaCl systems. *Canadian journal of chemistry*. 1985;63(11):3276-82.
122. Seo W-G, Matsuura H, Tsukihashi F. Calculation of phase diagrams for the FeCl₂, PbCl₂, and ZnCl₂ binary systems by using molecular dynamics simulation. *Metallurgical and Materials Transactions B*. 2006;37:239-51.
123. Viklund P, Hjörnhede A, Henderson P, Stålenheim A, Pettersson R. Corrosion of superheater materials in a waste-to-energy plant. *Fuel Processing Technology*. 2013;105:106-12.
124. Pettersson J, Folkeson N, Johansson L-G, Svensson J-E. The effects of KCl, K₂SO₄ and K₂CO₃ on the high temperature corrosion of a 304-type austenitic stainless steel. *Oxidation of metals*. 2011;76(1):93-109.
125. Ekström A. Conditions of increased life time of superheaters in loop seals: Uppsala University; 2018 [Master thesis]. Available from: <https://www.diva-portal.org/smash/record.jsf?pid=diva2%3A1186253&dswid=4676>.
126. Henderson P, Hjörnhede A. Combating corrosion in biomass and waste-fired plant. 2010.
127. Rishel D, Pettit F, Birks N. Some principal mechanisms in the simultaneous erosion and corrosion attack of metals at high temperatures. *Materials Science and Engineering: A*. 1991;143(1-2):197-211.
128. Norling R, Olefjord I. Erosion–corrosion of Fe-and Ni-based alloys at 550° C. *Wear*. 2003;254(1-2):173-84.
129. Niemi J, Kinnunen H, Lindberg D, Enestam S. Interactions of PbCl₂ with alkali salts in ash deposits and effects on boiler corrosion. *Energy & Fuels*. 2018;32(8):8519-29.
130. Talus A, Norling R, Wickström L, Hjörnhede A. Effect of lead content in used wood fuel on furnace wall corrosion of 16Mo3, 304L and alloy 625. *Oxidation of metals*. 2017;87(5-6):813-24.
131. Bankiewicz D, Yrjas P, Lindberg D, Hupa M. Determination of the corrosivity of Pb-containing salt mixtures. *Corrosion Science*. 2013;66:225-32.
132. Talus A, Kinnunen H, Norling R, Enestam S. Corrosion of carbon steel underneath a lead/potassium chloride salt mixture. *Materials and Corrosion*. 2019;70(8):1450-60.
133. Reimer L. Scanning electron microscopy: physics of image formation and microanalysis. *Measurement Science and Technology*. 2000;11(12):1826-.

134. Canovic S, Jonsson T, Halvarsson M, editors. *Grain contrast imaging in FIB and SEM*. Journal of Physics: Conference Series; 2008: IOP Publishing.
135. Guinier A. *X-ray diffraction in crystals, imperfect crystals, and amorphous bodies*: Courier Corporation; 1994.
136. Subcommittee A. *Standard test methods for determining average grain size*: ASTM international; 1996.
137. Zaefferer S, Habler G. *Scanning electron microscopy and electron backscatter diffraction*. 2017.
138. Larsson H, Jonsson T, Naraghi R, Gong Y, Reed RC, Ågren J. Oxidation of iron at 600 C—experiments and simulations. *Materials and corrosion*. 2017;68(2):133-42.
139. Larsson H, Reed R. On the numerical simulation of diffusion-controlled reactions under local equilibrium conditions. *Acta materialia*. 2008;56(15):3754-60.
140. Jonsson T, Liu F, Canovic S, Asteman H, Svensson J-E, Johansson L-G, et al., editors. *Microstructural Investigation of the Effect of Water Vapour on the Oxidation of the Si-Containing FeCrNi Steel 353MA at 900 (Degree Sign) C in Oxygen*. ECS Meeting Abstracts; 2006: IOP Publishing.
141. Amy S, Vangeli P. Water vapour effect on the high temperature resistant grades. *EUROCORR* 2001. 2001.
142. Valiente Bermejo MA, Núñez AM, Norling R. Metal loss and corrosion attack of FeCrAl overlay welds on evaporator tube shields of a waste-fired power plant. *Materials and Corrosion*. 2024.
143. Wright I, Shingledecker J. Rates of fireside corrosion of superheater and reheat tubes: making sense of available data. *Materials at High Temperatures*. 2015;32(4):426-37.
144. Norling R, Nafari A, Nylund A. Erosion-corrosion of Fe-and Ni-based tubes and coatings in a fluidized bed test rig during exposure to HCl- and SO₂-containing atmospheres. *Wear*. 2005;258(9):1379-83.
145. Pujilaksono B, Jonsson T, Halvarsson M, Svensson J-E, Johansson L-G. Oxidation of iron at 400–600 C in dry and wet O₂. *Corrosion Science*. 2010;52(5):1560-9.
146. Folkeson N, Jonsson T, Halvarsson M, Johansson LG, Svensson JE. The influence of small amounts of KCl (s) on the high temperature corrosion of a Fe-2.25 Cr-1Mo steel at 400 and 500° C. *Materials and Corrosion*. 2011;62(7):606-15.
147. Olivas-Ogaz MA, Eklund J, Persdotter A, Sattari M, Liske J, Svensson J-E, et al. The influence of oxide-scale microstructure on KCl (s)-induced corrosion of low-alloyed steel at 400 C. *Oxidation of Metals*. 2019;91:291-310.
148. Pujilaksono B, Jonsson T, Heidari H, Halvarsson M, Svensson J-E, Johansson L-G. Oxidation of binary FeCr alloys (Fe-2.25 Cr, Fe-10Cr, Fe-18Cr and Fe-25Cr) in O₂ and in O₂+H₂O environment at 600 C. *Oxidation of metals*. 2011;75:183-207.
149. Czakiert T, Krzywanski J, Zylka A, Nowak W. Chemical looping combustion: a brief overview. *Energies*. 2022;15(4):1563.
150. Coppola A, Scala F. Chemical looping for combustion of solid biomass: a review. *Energy & Fuels*. 2021;35(23):19248-65.
151. Pettersson J, Asteman H, Svensson J-E, Johansson L-G. KCl induced corrosion of a 304-type austenitic stainless steel at 600 C; the role of potassium. *Oxidation of Metals*. 2005;64(1):23-41.
152. Blomberg T, Makkonen P, Hiltunen M, editors. *Role of alkali hydroxides in the fireside corrosion of heat transfer surfaces, a practical approach*. Materials Science Forum; 2004: Trans Tech Publ.
153. Pettersson C, Pettersson J, Asteman H, Svensson J-E, Johansson L-G. KCl-induced high temperature corrosion of the austenitic Fe-Cr-Ni alloys 304L and Sanicro 28 at 600 C. *Corrosion Science*. 2006;48(6):1368-78.
154. Eriksson J-E, Lehmusto J, Silvander L, Lindberg D, Zevenhoven M, Yrjas P, et al. *Corrosion of Heat-Transfer Materials Induced by KCl, HCl, and O₂ Under Chemical-Looping Conditions*. *High Temperature Corrosion of Materials*. 2024:1-19.

155. Mei D, Lyngfelt A, Mattisson T, Linderholm C. Oxy-polishing of gas from chemical looping combustion: Fuel-nitrogen transformation and model-aided gas purity optimization. *Chemical Engineering Journal*. 2025;509:161267.
156. Pettersson R, Enecker J, Liu L. Role of nickel in the oxidation of Fe–Cr–Ni alloys in air–water vapour atmospheres. *Materials at High Temperatures*. 2005;22(3-4):269–81.
157. Gogolev I, Pikkarainen T, Kauppinen J, Hurskainen M, Lyngfelt A. Alkali emissions characterization in chemical looping combustion of wood, wood char, and straw fuels. *Fuel Processing Technology*. 2022;237:107447.
158. Nomoto H. Advanced ultra-supercritical pressure (A-USC) steam turbines and their combination with carbon capture and storage systems (CCS). *Advances in Steam Turbines for Modern Power Plants*: Elsevier; 2017. p. 501–19.
159. Josefsson H, Liu F, Svensson JE, Halvarsson M, Johansson LG. Oxidation of FeCrAl alloys at 500–900 °C in dry O₂. *Materials and Corrosion*. 2005;56(11):801–5.
160. Reddy MJ, Svensson J-E, Froitzheim J. Evaluating candidate materials for balance of plant components in SOFC: oxidation and Cr evaporation properties. *Corrosion Science*. 2021;190:109671.
161. Eklund J, Persdotter A, Ssenteza V, Jonsson T. The long-term corrosion behavior of FeCrAl (Si) alloys after breakaway oxidation at 600 °C. *Corrosion Science*. 2023;217:111155.
162. Asokan V, Eklund J, Bigdeli S, Jonsson T. The influence of Si on the primary protection of lean FeCrAl model alloys in O₂ and O₂+ H₂O at 600 °C—A microstructural investigation. *Corrosion Science*. 2021;179:109155.
163. Sand T, Edgren A, Geers C, Asokan V, Eklund J, Helander T, et al. Exploring the effect of silicon on the high temperature corrosion of lean fecral alloys in humid air. *Oxidation of Metals*. 2021;95:221–38.
164. Jonsson T, Karlsson S, Hooshyar H, Sattari M, Liske J, Svensson J-E, et al. Oxidation after breakdown of the chromium-rich scale on stainless steels at high temperature: internal oxidation. *Oxidation of Metals*. 2016;85:509–36.
165. Persdotter A. Beyond Breakaway Corrosion: Investigating the Secondary Corrosion Protection of Iron-Based Alloys: Chalmers Tekniska Hogskola (Sweden); 2023.
166. Blomberg T, Tripathi T, Karppinen M. New chemical mechanism explaining the breakdown of protective oxides on high temperature steels in biomass combustion and gasification plants. *RSC advances*. 2019;9(18):10034–48.
167. Intiso L, Johansson L-G, Svensson J-E, Halvarsson M. Oxidation of Sanicro 25 (42Fe22Cr25NiWCuNbN) in O₂ and O₂+H₂O Environments at 600–750 °C. *Oxidation of Metals*. 2015;83:367–91.
168. Sand T, Geers C, Cao Y, Svensson J, Johansson L. Effective reduction of chromium-oxy-hydroxide evaporation from Ni-base alloy 690. *Oxidation of Metals*. 2019;92:259–79.
169. Dahl KV, Slomian A, Lomholt TN, Kiamehr S, Grumsen FB, Montgomery M, et al. Characterization of pack cemented Ni₂Al₃ coating exposed to KCl (s) induced corrosion at 600 °C. *Materials at High Temperatures*. 2018;35(1-3):267–74.
170. Ssenteza V, Eklund J, Hanif I, Liske J, Jonsson T. High temperature corrosion resistance of FeCr (Ni, Al) alloys as bulk/overlay weld coatings in the presence of KCl at 600 °C. *Corrosion Science*. 2023;213:110896.
171. Moud PH, Andersson KJ, Lanza R, Pettersson JB, Engvall K. Effect of gas phase alkali species on tar reforming catalyst performance: Initial characterization and method development. *Fuel*. 2015;154:95–106.
172. Gall D, Nejman C, Allguren T, Andersson K, Pettersson JB. A new technique for real-time measurements of potassium and sodium aerosols based on field-reversal surface ionization. *Measurement Science and Technology*. 2021;32(7):075802.
173. Advancing chemical-looping combustion of domestic fuels [Available from: <https://cetpartnership.eu/calls/funded-project/acloud>].